Network Modeling
Stochastic and Deterministic Approaches

Giovanni Sansavini

Dissertation submitted to Virginia Polytechnic Institute and State University
in partial fulfillment of the requirements for the degree of

Doctor of Philosophy
in
Engineering Mechanics

Muhammad R. Hajj, Co-Chairman
Ishwar K. Puri, Co-Chairman
John C. Duke
Rahul V. Kulkarni
Shane D. Ross

September 1, 2010
Blacksburg, Virginia

Keywords: Network Systems, Cascading Failures, Percolation Transition, Interdependent Networks

Network Modeling
Stochastic and Deterministic Approaches

Giovanni Sansavini

(ABSTRACT)

Stochastic and deterministic approaches for modeling complex networks are presented. The methodology combines analysis of the structure formed by the interconnections among the elements of a network with an assessment of the vulnerability towards the propagation of cascading failures. The goal is to understand the mutual interplay between the structure of the network connections and the propagation of cascading failures.

Two fundamental issues related to the optimal design and operation of complex networks are addressed. The first concerns the impact that cascading failures have on networks due to the connectivity pattern linking their components. If the state of load on the network components is high, the risk of cascade spreadings becomes significant. In this case, the needed reduction of the connectivity efficiency to prevent the propagation of failures affecting the entire system is quantified. The second issue concerns the realization of the most efficient connectivity in a network that minimizes the propagations of cascading failures. It is found that a system that routinely approaches the critical load for the onset of cascading failures during its operation should have a larger efficiency value. This allows for a smoother transition to the cascade region and for a reasonable reaction time to counteract the onset of significant cascading failures.

The interplay between the structure of the network connections and the propagation of cascading failures is assessed also in interdependent networks. In these systems, the linking among several network infrastructures is necessary for their optimal and economical operation. Yet, the interdependencies introduce weaknesses due to the fact that failures may cascade from one system to other interdependent systems, possibly affecting their overall functioning. Inspired by the global efficiency, a measure of the communication capabilities among interdependent systems, i.e. the interdependency efficiency, is defined. The relations between the structural parameters, i.e. the system links and the interdependency links,

and the interdependency efficiency, are also quantified, as well as the relations between the structural parameters and the vulnerability towards the propagation of cascading failures. Resorting to this knowledge, the optimal interdependency connectivity is identified.

Similar to the spreading of failures, the formation of a giant component is a critical phenomenon emerging as a result of the connectivity pattern in a network. This structural transition is exploited to identify the formation of macrometastases in the developed model for metastatic colonization in tumor growth. The methods of network theory proves particularly suitable to reproduce the local interactions among tumor cells that lead to the emergent global behavior of the metastasis as a community. This model for intercellular sensing reproduces the stepwise behavior characteristic of metastatic colonization. Moreover, it prompts the consideration of a curative intervention that hinders intercellular communication, even in the presence of a significant tumor cell population.

Acknowledgements

I am most thankful to my advisors, Prof. Muhammad Hajj and Prof. Ishwar Puri, for giving me the opportunity to work with them in the Department of Engineering Science and Mechanics. Their wisdom and experienced guidance positively shaped all of the aspects of my research, and their abundant enthusiasm and optimism were a tremendous help, especially during times of discouragement.

For playing an important role in defining the lines of research that led to this dissertation, I am also very grateful to my Italian Ph.D. advisor, Prof. Enrico Zio. I am indebted to him for having made me aware of the joint agreement for dual doctoral degrees between Politecnico di Milano and Virginia Polytechnic Institute and State University.

The example of these three individuals, as both scholars and men, will not be forgotten.

I would also like to thank Prof. John Duke, Prof. Rahul Kulkarni, and Prof. Shane Ross for serving on my committee and for their valuable questions and beneficial advice.

A special mention goes to the fellow students who took part in the Complex Systems meetings, Mehdi Ghommem and Ganesh Balasubramanian, for contributing to my work with many important suggestions and fruitful discussions.

Thanks belong to each and every fellow ESM graduate student, in particular, my officemates of past and present: Mehdi Ghommem, Andrea Mola, Giancarlo Bordonaro, Abdessattar Abdelkefi, Arnab Gupta, Alireza Karimi, Mohammad Majharul Islam, Yasser Aboelkassem and Rui Vasconcellos. Their friendship and support is much appreciated.

All of the staff members of the Department of Engineering Science and Mechanics deserve my gratitude. Specifically, Lisa Smith and Anne-Marie Bracken are acknowledged for their unfailing help with paperwork, and Tim Tomlin is recognized for his assistance with respect

to setting up simulations on the departmental computational resource.

I would also like to express gratitude to all of my friends in my home country of Italy, as well as to all of my friends at Virginia Tech, particularly the members of the Italian community who made the time spent in Blacksburg both colorful and eventful. I will always carry a pleasant memory of the faces and the personalities of each one of them.

With love and appreciation, beyond that which I can express with words, I thank my parents, Claudio and Paola. They have always been in the right place at the right time, with loving support and endless words of encouragement. I also thank my grandparents, Bruno and Anna, and my aunts and their families for their unconditional support, with a special thought for my deceased grandparents, Pino and Rina.

Last but not least, I owe a huge thanks to my fiancée Lucia for accepting the challenge of creating ties with someone who undertook a dual doctoral degree, especially when we were separated by great distances. Thank you for coping with my bad moods. Thank you for trusting me. Thank you for sharing your life with me. No matter the distance between us, you are by my side.

Contents

List of Figures

List of Tables

Chapter 1

Introduction

We live in a world of networks, where almost everything is connected to everything else. We experience this when we meet mutual acquaintances, when we look at road or public transportation infrastructures, or when we realize to what extent epidemics can spread throughout the globe. Indeed, networks are pervasive in nature. As part of individuals, we are the elements of a network of social interactions of various kinds and, as biological systems we are the synergic result of a network of biochemical reactions. Networks can be physical objects in Euclidean space, such as electric power grids, the Internet, highways or subway systems and neural networks. They can be also entities defined in an abstract space, such as networks of relationships or collaborations between individuals. Understanding the structure and dynamics of these networks will help solve complex and pressing problems such as designing the optimal connectivity of single or coupled infrastructures, regulating internal biochemical reactions to hinder the course of a tumor, or stopping a network failure or disease outbreak before it spreads catastrophically. On the other end, ethical and social problems arise from the study of networks. For example, the findings that are applied to the improvement of those infrastructures that provide essential services in modern societies, might themselves be employed to mount a more efficient attack against the same infrastructures.

The study of networks arose as a branch of discrete mathematics, namely graph theory, in 1736, when the Swiss mathematician Leonhard Euler published the solution to the Königsberg bridge problem (1) by finding a path that traversed each of the bridges of the

city of Königsberg exactly once. Since then, graph theory has provided answers to a series of practical questions such as: what is the maximum flow per unit time from source to sink in a network of pipes (2), how to color the regions of a map using the minimum number of colors so that neighboring regions receive different colors (the so called four color map theorem) (3), or how to fill n jobs by n people to obtain maximum productivity (4). The study of networks has also resulted in important advances social network analysis with interest in the relationships among social entities, such as communication between elements of a group, trades among countries, or economic transactions between companies (5).

Over the last decade, researchers have developed a renewed interest in the study of complex networks, i.e. networks whose architecture is irregular, more complex than classical random graphs and dynamically evolving in time. This activity was fostered by two seminal articles, the first authored by Watts and Strogatz on small-world networks that appeared in Nature in 1998 (6), and the second authored by Barabási and Albert on scale-free networks that appeared in Science in 1999 (7). The increased computing power and the possibility to study the properties of many large databases of real networks has facilitated the study of complex systems. These include transportation networks, telephone networks, the Internet and the World Wide Web, the actors collaboration network in movie databases, scientific co-authorship and citation networks, and also systems of interest in biology and medicine, such as neural, genetic, metabolic and protein networks (8).

1.1 Motivation

The first issue faced in the study of complex networks is the analysis of their *structure*. New concepts and measures have been defined to characterize the topology of real networks. The main result has been the identification of a series of unifying principles and statistical properties common to most real networks. A relevant property concerns the degree of a node, i.e. the number of its direct connections to other nodes. In real networks, the degree distribution $P(k)$ is defined as the probability that a node chosen uniformly at random has degree k or, equivalently, as the fraction of nodes in the graph having degree k. $P(k)$ deviates from the Poisson distribution expected for a random graph and exhibits a power law (scale-

free) tail with an exponent γ between 2 and 3 (9). Real networks are characterized by correlations in the node degrees by having short paths between any two nodes (small-world property) and by the presence of a large number of short cycles.

The discovery of unifying principles in complex network architectures has led to the development of evolution models to mimic the growth of a network and to reproduce the structural properties observed in real topologies. It turns out that the structure of a real network is the result of the evolution of the forces that shape it and it affects the function of the system. This stage of the analysis is motivated by the expectation that understanding and modeling the structure of a complex network can lead a better understanding of its evolutionary mechanisms, and to a better knowledge of its dynamical and functional behavior.

Network architecture has fundamental consequences for network functional robustness and vulnerability to external perturbations, such as random failures or targeted attacks (10). Therefore, a structural analysis must be complemented by the study of the *dynamical behavior* of interconnected elements interacting via complex topologies. These analyses aim at understanding the role played by the network topology in determining the emergence of collective dynamical behavior, such as percolation or synchronization, or the main features of relevant processes, such as the spreading of failures, epidemics and information (11).

1.2 Objectives

Building on these recent developments in the field of complex network theory, this dissertation is devoted to the study of engineered infrastructures or biological systems that can be represented as networks of interacting elements. In particular, our methodology can be divided into three steps. First, the topology of the graph representing the complex system structure is analyzed through a lumped parameter that characterizes the connection efficiency of the network. Then, the dynamic behavior of the complex system is assessed through functional models abstracting the physical communication processes, mainly through the propagation of some entity, such as electricity, data, or vehicles. The propagation of perturbations, e.g. failures of some components that cascade to other components in the network, is analyzed in this step. Finally, the mutual interplay between the structure of the network connections and

the propagation of cascading failures is considered. Our aim is to address two fundamental questions related to the design and operation of complex systems: (I) to what extent do cascading failures propagate in the network due to the connectivity pattern linking its elements and (II) how the most efficient connectivity in a network that minimizes the propagations of cascading failures can be realized.

The issue of how the connectivity influences the propagations of cascading failures is addressed in both isolated networks and interdependent networks. The latter are coupled networks in which some of the elements are interconnected, and failures in one system can affect components in the dependent systems. In particular, we aim to relate the vulnerability towards cascading failures to global connectivity efficiency in isolated networks. This allows selecting the proper network configuration in order to control the extent to which failures weaken the system. In interdependent networks, we analyzed the interplay between the structures of the systems and the propagation of failures and found a criterion to determine the optimal interdependency connectivity that minimizes the vulnerability to cascading failures.

The final part of this dissertation deals with nonequilibrium systems, i.e. networks whose structures are evolving in time through the addition/removal of nodes/links. We consider a spatial network whose nodes are located in the two-dimensional Euclidean space. These are connected by a link depending on their mutual distances. We aim to determine a critical behavior at specific numbers and densities of nodes, namely, through the emergence of a giant component, i.e. a cluster that spans the entire network. This transition, called percolation transition (12), marks the appearance of emerging properties and phenomena in complex systems and characterizes variations in their dynamics (13). The model for evolving networks is applied to the metastatic colonization in tumor growth and it reproduces the emergence of a collective behavior in the metastatic cell aggregate. The new system behavior identifies the formation of overt macrometastases which can mount an effective attach to the host organ.

The dissertation is structured as follows. In Chapter 2, the approach undertaken in the study of networks is presented. The methods of network theory that have been employed are detailed, namely, the structural analysis of the network connectivity and the dynamical analysis of propagation phenomena in networks, e.g. the spread of failures in engineered infrastructures. The functional model to simulate the propagation of failures in the systems

is also introduced.

In Chapter 3, a deterministic representation of the cascade of failures in complex network is developed and applied to estimate the vulnerability towards cascading failures. Due to the lack of conservation equations for network systems, deterministic models are not applied in the description of their global behavior. The developed deterministic model is built on few simulation results but it is able to predict the outcome of a spreading process in arbitrarily connected networks. Thus, it is an useful tool to quickly assess the variation of the network dynamics with respect to changes of the connectivity.

Many networks, e.g. engineered infrastructures, do not exist in isolation and are strongly interdependent on one another. For example, the communication system is strongly dependent on the proper operation of the electrical power transmission system, and vice versa. The relations among interdependent networks must be identified to perform realistic and applicable analyses on these real-world systems. To this end, the effects that the structure of interdependent networks have on the propagation of cascading failures are assessed in Chapter 4. The influences and limitations that interacting networks impose on the individual system operating conditions and the optimal connectivity among interdependent networks are identified.

The emergence of critical phenomena in complex networks is studied in Chapter 5. The community structure of a network evolving under several constraints is analyzed. In particular, the emergence of the largest connected component and the evolution of its size are investigated. This is a basic structural transition in the network architecture. The transition is studied in an evolution model that describes the formation of metastases in tumor growth and assumes intercellurar communication among metastatic cells. The percolation transition due to the emergence of a giant connected component is related to the cells ability to initiate a collective global behavior as a results of the local interactions among single cells. This model for intercellular sensing during metastasis reproduces the stepwise behavior characteristic of metastatic colonization. Moreover, it demonstrates that the transition from micro- to macrometastases is an intrinsic characteristic of metastatic growth and prompts the consideration of a curative intervention that hinders intercellular communication.

This dissertation has been written under the joint agreement for dual doctoral degrees between Politecnico di Milano and Virginia Polytechnic Institute and State University.

Chapter 2

Approach

As stated by Strogatz (14), networks are inherently difficult to understand due to their structural complexity as the wiring of its components can be very intricate, evolution as the wiring changes dynamically over time with the addition and deletion of nodes, connection diversity as the links between components may have different weights, directions and signs, dynamical complexity as the nodes can be nonlinear dynamical systems, node diversity, as there can be many different kinds of nodes, and finally their meta-complication where various complications can influence each other. One example is the present layout of a power grid that depends on how it has grown over the years: a case where network evolution affects topology.

In this chapter, we address the structural characteristics of different network topologies. The general focus is on sparse, decentralized, connected networks that are neither completely ordered nor completely random. This is formalized under the following constraints (15):

1. The network is numerically large, i.e. made up of a number of interconnected components $N \gg 1$.

2. The network is sparse in the sense that each component is connected to an average of only $\langle k \rangle \ll N$ other components.

3. The network is decentralized in the sense that there is no dominant central component to which most others are directly connected. This means that not only the average

degree of connection $\langle k \rangle$ must be much less than the network size N but also the maximal degree of connection, $k_{max} \ll N$.

4. The network is highly clustered.

5. The network is connected in the sense that any node can be reached by any other node through a finite number of links or edges.

As mentioned in Chapter 1, network analysis is divided into topological analysis, which is concerned with the structural properties of the connectivity pattern underlying a network, and dynamical analysis, which involves the assessment of how physical entities or perturbations propagate along the wiring connections of a network. Both analyses share the same mathematical representation of network systems as graphs $G(N, K)$ in which the physical constituents (components) of a network are mapped into N nodes (or vertices), that are connected by K edges (or arcs or links) representing the links of physical connections among them.

2.1 Structural analysis

The focus of topological analysis is on the structural properties of the graphs at both global and local scales, e.g. as represented, respectively, by their characteristic path length, $\mathcal{L}$, that is defined as the number of arcs in the shortest path between two nodes averaged over all pairs of nodes, and average clustering coefficient, C, which is a measure of the extent to which nodes tend to form small groups (6). Average global measures, such as $\mathcal{L}$, provide indications on the extent to which each node i in the system is connected with any other node j, while average local measures, like C, assess to what extent the first neighbors of each node i are connected among each other.

In the structural analysis, the K edges are unweighted, i.e. they are regarded as being all equal irrespective of their physical characterizations. In practice, networks are often quite sparse, with $K \ll N(N-1)/2$. The graph $G(N, K)$ representing a network system is defined by its $N \times N$ adjacency (connection) matrix $\{a_{ij}\}$ whose entry is

$$a_{ij} = 1 \text{ if there is an edge joining vertex } i \text{ to } j$$
$$= 0 \text{ otherwise.}$$

The graph connectivity (or degree) distribution, $P(k)$, can then be evaluated as the probability that a generic node in the network is connected to k other nodes. As we shall see, random graphs and small-world networks display a Poisson distribution whereas most real complex networks are actually characterized by highly heterogeneous distributions of a truncated power-law type: $P(k) \sim k^{-\gamma}\phi(k|\zeta)$, where $\phi(k|\zeta)$ introduces a cut-off at some characteristic scale ζ. Three main classes can be defined: a) when ζ is very small, $P(k) \sim \phi(k|\zeta)$ and thus the connectivity distribution is single-scaled, typically corresponding to exponential or Gaussian distributions; b) as ζ grows, a power law with a sharp cut-off is obtained; c) for large ζ, scale-free networks are obtained. Cases b) and c) have been shown to be widespread in practice and their topological properties have immediate consequences for network robustness and fragility.

The identification of the network degree distribution, $P(k)$, is a first step in the assessment of the vulnerability characteristics of a network, providing information on its general response behavior to random failures or targeted attacks. It can also give insights on the network structure, e.g. a degree distribution that peaks at $k = 2$ reveals the mainly sequential structure of the network under study. Further characterization of the network structure is sought in terms of single-valued parameters that, on average indicate the global and local features of a network. Given the adjacency matrix $\{a_{ij}\}$ of a network graph $G(N, K)$, it is possible to compute the matrix of the shortest path lengths $\{d_{ij}\}$ whose entry d_{ij} is the number of edges making up the shortest path linking i and j in the network. The computation can be performed in N steps using the Floyd's sequential shortest path iterative algorithm, which at each step constructs an intermediate matrix containing the current shortest distance between each pair of nodes until convergence (16). The fact that G is assumed to be connected implies that the value of d_{ij} is positive and finite when $i \neq j$. For studying the global properties of the network topology, the probability distribution $P(d_{ij})$ of the shortest path lengths d_{ij} between any two nodes i and j in the network should be considered. The upper

value that $\{d_{ij}\}$ can assume is called the diameter of the network and it is used as a measure of the size of the network. It can be thought of as the maximum distance which is necessary to cover in order to walk from a randomly chosen node to another randomly chosen node (17). The d_{ij} distribution is useful to obtain an idea of what the distance most likely to be covered in the majority of the cases when moving from one node to another. The shortest path length distribution, is often synthesized by a point value, the average or characteristic path length, $\mathcal{L}$, which represents the average of the shortest distances d_{ij} between all pairs of nodes:

$$\mathcal{L}(G) = \left(\sum_{i \neq j \in G} d_{ij} \right) / \left(N(N-1) \right). \tag{2.1}$$

It represents the average distance which has to be covered to reach the majority of nodes in the graph representing the network system. $\mathcal{L}$ is a parameter related to the global structure of the network. The constraint enforcing network connectivity guarantees that $\mathcal{L}$ is a truly global statistic. It gives the average minimum distance between any pair of nodes and as such measures the typical separation between two nodes in the graph (a global property). In a friendship network $\mathcal{L}$ would measure the average number of friends in the shortest chain connecting two people (6).

The local connectivity of a network can also be synthesized through a single-valued parameter, the so called average clustering coefficient, C. The clustering coefficient C_i is a local property of node i defined as follows (17): if node i has k_i neighbors, then at most $k_i(k_i-1)/2$ edges can exist between them; C_i is the fraction of these edges that actually exist; then C is the average of the C_i values:

$$C_i = \frac{\text{Number of edges connecting the neighborhood of } i}{\text{Max possible number of edges connecting the neighborhood of } i,\ k_i(k_i-1)/2}$$

$$C(G) = \left(\sum_i C_i \right) / N. \tag{2.2}$$

Equivalently, C can be regarded as the probability that a pair of vertices u and v are connected given that each one is also connected to a mutual friend w. From the definition,

it is clear that C is a measure of the local structure of the network. The largest value that C can attain is 1 for a complete graph (all nodes connected with each other, $\langle k \rangle = N - 1$) and the smallest is 0, for an empty graph (no connections among the nodes, $\langle k \rangle = 0$) or a complete sequential graph, a ring, where $k_i = 2,\ i = 1, \ldots, N$. Large values of C are welcome for the robustness of the connectivity. A node removal disconnecting two portions of the system would be overcome by simply passing onto adjacent working nodes through short-range neighboring nodes. C gives the probability that two neighbors of a given node are also neighbors of one another and as such measures the cliquishness of a typical neighborhood (a local property). In a friendship network, C_i reflects the probability that friends of i are also friends of each other. In this view, C can be thought of as a simple measure of order: graphs with $C \gg \langle k \rangle / N$ are locally ordered in the sense that nodes with at least one mutually adjacent node are likely to be themselves adjacent (6).

However, there are two limitations which somewhat hinder the practical application of the topological indicators $\mathcal{L}$ and C for characterizing real network systems (18):

1. They are ill-defined if:
   (a) The network is not fully connected, i.e. some nodes are not connected to the remaining part of the network ($\mathcal{L} = \infty$);
   (b) Some nodes have only one neighbor, i.e. $k_i = 0$ ($C_i = 0/0$)
2. They retain only the topological information on the existence or absence of a link, with no reference to the physical length and capacity of the link. In other words, they are applicable only to unweighted networks.

2.2 Weighted networks

Indeed, along with a complex topological structure, many real networks display a marked physical heterogeneity in the capacity and intensity of the connections. Examples are different impedance and reliability characteristics of overhead lines in electrical transmission networks (19; 20), unequal traffic on roads which affects accident probability (21) or different routing capacities of the Internet links (22). To describe the inhomogeneities of real

physical systems, numerical weights can be assigned to each link of the representative network, measuring the 'strength' of the connection. In this way, the functional behavior of the network is somewhat embedded into a generalized, but still simple, topological analysis framework. Global and local measures can then be introduced for the statistical characterization of 'weighted' networks (18). The resulting generalized setup, in which global and local efficiencies measure the network global and local connectivity features accounting also for the arcs weights, encompasses the topological analysis of unweighted networks in the case that all edges have unit weight.

In addition to the adjacency matrix $\{a_{ij}\}$, defined for the unweighted graph, an additional matrix $\{l_{ij}\}$ of weights (e.g. physical distances (18), failure/accident probabilities (20; 21), 'electrical' distances (19)) can be introduced to describe the network. Of course, in the case of an unweighted network, $l_{ij} = 1$. On the basis of both $\{a_{ij}\}$ and $\{l_{ij}\}$, the matrix of the shortest path lengths $\{d_{ij}\}$ is computed: the length d_{ij} of the shortest path linking i and j in the network is the smallest sum of the physical distances throughout all the possible paths from i to j. Assuming that the network system is parallel, i.e. that every node concurrently sends information through its edges, a measure of efficiency in the communication between nodes i and j is defined as inversely proportional to the shortest distance (18). Thus, the network is characterized also by an efficiency matrix $\{\epsilon_{ij}\}$, whose entry is the efficiency in the communication between nodes i and j:

$$\begin{aligned} \epsilon_{ij} &= 1/d_{ij} \text{ if there is at least one path connecting } i \text{ and } j \\ &= 0 \text{ otherwise } (d_{ij} = \infty). \end{aligned}$$

The average efficiency of $G(N, K)$ is then

$$E_{glob}(G) = \left(\sum_{i \neq j \in G} \epsilon_{ij} \right) / (N(N-1)) = \left(\sum_{i \neq j \in G} 1/d_{ij} \right) / (N(N-1)). \tag{2.3}$$

This quantity plays the role of $\mathcal{L}$ in defining the network connection characteristics on a global scale. The fundamental difference is that E_{glob} is the efficiency of a parallel network of nodes which concurrently exchange packets of information, whereas $1/\mathcal{L}$ measures the

efficiency in a sequential system where only one packet of information at the time goes along the network. Thus, $1/\mathcal{L}$ represents well the efficiency of unweighted networks where no difference is made on the distances in the graph.

For comparison of different network systems, it is useful to normalize $E_{glob}(G)$ by considering the ideal, fully-connected network $G_{id}(N)$ in which all N nodes of the network are connected and which contains $N(N-1)/2$ edges. Such a system propagates the information in the most efficient way since $\{d_{ij}\} = \{l_{ij}\}$. The corresponding (maximum) value of global efficiency is:

$$E_{glob}\left(G_{id}\right) = \left(\sum_{i \neq j \in G_{id}} 1/l_{ij}\right) / \left(N\left(N-1\right)\right). \tag{2.4}$$

By dividing Eq. 2.3 by 2.4, one obtains a normalized value of global efficiency for the graph $G(N,K)$, which for simplicity of notation is still denoted as $E_{glob}(G)$ and is such that $0 \leq E_{glob}(G) \leq 1$. One can also quantify the local properties of the graph $G(N,K)$ by specializing the definition of the average efficiency 2.3 on the subgraph G_i of the neighbors of each node i in the network:

$$E\left(G_i\right) = \left(\sum_{n \neq m \in G_i} \epsilon_{nm}\right) / \left(k_i\left(k_i - 1\right)\right). \tag{2.5}$$

Averaging the efficiency of the local neighborhoods of all nodes in the network one can define a measure of the network local efficiency:

$$E_{loc}\left(G\right) = \left(\sum_{i=1 \in G}^{N} E(G_i)\right) / N. \tag{2.6}$$

Since $i \notin G_i$, this parameter reveals how much the system is fault tolerant in that it measures the efficiency of the communication between the first neighbors of i when i is removed. The local efficiency $E_{loc}(G)$ plays a role similar to the clustering coefficient C in measuring how well connected is a network. It can be shown that when most of the local subgraphs G_i of a graph G are not sparse, C gives a good approximation of $E_{loc}(G)$ (18).

The average global and local topological efficiency measures $E_{glob}(G)$ and $E_{loc}(G)$ are the output of the analysis of weighted networks. It is worth mentioning that when $\{a_{ij}\} = \{l_{ij}\}$,

i.e. the adjacency matrix and the weight matrix coincide, the output of the weighted analysis and the output of the unweighted topological analysis coincides in that all edges have equal unit weights, i.e. $l_{ij} = 1$ for every i and j, $i \neq j$.

2.3 Families of networks

2.3.1 Erdős-Rényi random networks

Consider a graph of N nodes. Each possible edge between two given nodes occurs with some probability p. The average degree of connection of a given node in the graph is $\langle k \rangle \sim Np$ and the connectivity distribution $P(k)$ follows a Poisson distribution which peaks at $\langle k \rangle$. As such, this so called Erdős-Rényi (ER) random graph (23) is fairly well characterized by the parameter $\langle k \rangle$. This model displays a phase transition at a critical average degree $k_c = 1$. At this critical value, a giant component forms. For $\langle k \rangle > k_c$, a large fraction of nodes are connected in the network whereas for $\langle k \rangle < k_c$ the system is fragmented in small subgraphs. The importance of this phenomenon is obvious in terms of the collective properties that arise at the critical point: communication among the whole system becomes available. Besides, the transition occurs suddenly, implying 'innovation', and takes place at a low cost in terms of the number of required links. Since the only requirement in order to reach full communication is to have a given (small) number of links per node, once the threshold is reached, order can emerge 'for free'. ER random graphs are characterized by very short path lengths, $\mathcal{L}_r = \log N / \log \langle k \rangle$ and small clustering coefficients, $C_r = \log \langle k \rangle / \log N$.

2.3.2 Small-world networks

The evidence that both natural and artificial systems display a high heterogeneity in their interconnected structures challenges the early approaches to system complexity based on purely random graphs and calls for new interpretations on how complexity might emerge from the interactions among system's parts. Small-world networks are characterized by the coincidence of high local clustering of components ($C \gg C_r$) and short global separation among the clusters ($\mathcal{L} \sim \mathcal{L}_c$) (6). As a result, these networks bear two most remarkable properties: local robustness and global accessibility. The robustness comes from dense local

clusters (e.g. families, friendship circles, cities and countries in the social context). The global accessibility comes from shortcuts, i.e. edges which connect otherwise separated clusters: it is because of these shortcuts that the world of the complex network seems small.

The small characteristic length in a small-world network is due to the presence of few long-range edges in a highly clustered network. Such shortcuts connect nodes which would otherwise be widely separated, much farther than $\mathcal{L}_r$. Thus, a single shortcut contracts the distance not only between the pair of nodes it connects but also between their immediate neighbors, the neighbors of the neighbors and so on, bearing a highly nonlinear impact on $\mathcal{L}$. By contrast, the presence of a long-range edge instead of a local connection in a clustered neighborhood impacts the clustering coefficient C only in the single neighborhood whose clustering is affected. This nonlinear versus linear global impact of shortcuts enables the coexistence of large values of C with small values of $\mathcal{L}$. Thus, it can be conjectured that the small-world phenomenon might be common in sparse, highly clustered ($C \gg \langle k \rangle / N$) connected networks with many nodes and a small fraction of long-range shortcuts. Actually, it is possible to contract distances with negligible effects on clustering, by long-range contractions in large graphs without resorting to shortcuts at all (15). An important implication of small-world graphs is that most nodes have no shortcuts at all in their local neighborhood. This absence of global information at the local scale poses significant problems for effective tracing of shortest path lengths in a network. If shortcuts exist, but they are outside the local neighborhood, it becomes difficult to utilize them consciously to construct an optimal path. Finally, small-world networks are characterized by a Poissonian connectivity distribution $P(k)$ which peaks at an average value $\langle k \rangle$ and then decays exponentially. Such an exponential network is homogeneous in nature, each node having roughly the same number of connections $\langle k \rangle$ (10). The definition of the small world behavior can also be rephrased in terms of the information flow. Small world networks are characterized by high values of both E_{glob} and E_{loc}, i.e. high efficiency in both global and local communication.

The functional significance of small-world connectivity relates to the dynamics of a network system. This implies investigating the relationship between the network topology and the globally emergent features of its dynamic behavior. It turns out that the gross features of the dynamics are dominated by the characteristic path length of the underlying network

structure. Hence, the highly clustered nature of small-world graphs can lead to the intuition that a given effect is far away when on the contrary it is effectively close and may spread rapidly (15).

2.3.3 Scale-free networks

The inhomogeneous connectivity distribution of many real networks is reproduced by the scale-free model (7). Building such a model can be pursued by incorporating two ingredients common to real networks: growth and preferential attachment. The model begins with m_0 nodes and at every time step t a new node is connected to m of the already existing nodes. The probability Π_i that the new node is connected to node i is proportional to the connectivity k_i of node i, i.e. $\Pi_i = k_i / \sum_i k_i$ (the 'rich get richer' behavior). For large t, the connectivity distribution is a power law $P(k) = 2m^2/k^3$.

To address the error tolerance of network systems, one can study the changes in the characteristic path length $\mathcal{L}$ when a small fraction of the nodes is removed to simulate its malfunction (10). The removal of any node in general tends to increase the distance between the remaining nodes. Indeed, for the exponential networks like the small-world model, $\mathcal{L}$ increases monotonically with the fraction of removed nodes. This means that it is increasingly difficult for the remaining nodes to communicate with each other in spite of the redundant wiring of the network. This is due to the inherent homogeneity of the network. Since all nodes have approximately the same number of connections, they all equally contribute to the network characteristic path length so that the removal of each node causes the same amount of damage. On the contrary, in scale-free networks, the characteristic path length remains unchanged under an increasing level of removals, and so does the communication between the remaining nodes. The robustness of scale-free networks is rooted in their extremely inhomogeneous connectivity distribution. Because the power law implies that the majority of nodes have only a few links, nodes with small connectivity will be selected with much higher probability with their removal having a minor impact on the overall network topology and thus on the communication among the remaining nodes.

An opposite behavior results with respect to the network fragility to preferential attacks directed to the most vulnerable points of the network, i.e. the most connected points. For

an exponential network, its homogeneity now turns out to be a favorable property such that there is no substantial difference in the characteristic path length whether the nodes are selected for removal at random or preferentially with large connectivity. On the contrary, in the inhomogeneous, scale-free networks the removal of the most connected nodes results in a rapid increase in the characteristic path length and a corresponding damage to the network connectivity which is, indeed, maintained by a few highly connected nodes whose removal drastically alters the network topology and decreases the ability of the remaining nodes to communicate with each other.

In summary, due to their inhomogeneous structure in which most nodes have very few connections and only a small number of nodes have many connections, scale-free networks display a surprisingly high degree of tolerance against random failures; a property not shared by their exponential, homogeneous counter parts. However, this comes at the expense of an increased vulnerability to preferential attacks directed at the most connected nodes.

2.4 Dynamical analysis

In real network systems, it is important to model the dynamics of the flow of physical quantities in the network. This entails considering the interplay between structural characteristics and dynamical aspects, which makes the modeling and analysis very complicated, since the load and capacity of each component, and the flow through the network are often highly variable quantities in both space and time. Functional models have been developed to capture the basic realistic features of networks within a topological analysis framework, i.e. disregarding the representation of the individual dynamics of the network elements. These models have shed light on the way complex networks react to faults and attacks, evaluating their consequences when the dynamics of flow of the physical quantities in the network is taken into account. The response behavior often results in a dramatic cascade phenomenon due to avalanches of node ruptures (24–26).

Various abstract models of cascading failures have been applied to simulate the propagation process in single networks, differing for the logic of redistribution of the failure load (24; 26; 27). The choice of the most suitable algorithm for modeling the spreading process

taking place in a given network must be performed carefully, considering the type of service provided by the it.

The propagation model developed for this analysis considers failure-free edges to focus on the failure propagation dynamics over the network nodes. In the abstract failure cascade modeling presented (26), the spreading variable of interest is typically normalized in the range $[0, 1]$, for generality purposes. For application to specific network, the normalization is dropped and the physical nature of the service provided is considered to tailor the abstract model to the real system.

In the study of the failure cascade propagation mechanism triggered by random failures or targeted attacks, the network system is still modeled as a graph $G(N, K)$, just as in the structural analysis. The N identical components are assigned random initial loads sampled uniformly between a minimum value L^{min} and a maximum value L^{max}. The system is operated so that the initial component loadings vary from L^{min} to $L^{max} = L^{fail} = 1$. Then, the average initial component loading $L = (L^{min} + 1)/2$ can be increased by increasing L^{min} in the uniform distribution of the initial load.

All components have the same limit of operation L^{fail}, beyond which they fail. When a component fails, the overload is propagated locally and a fixed and positive amount of load P is transferred to first-neighbors of the failed node in the network structure. If there is no working node in the neighborhood of a failed component, the cascade spreading in that direction is stopped.

To initiate the cascade, an initial disturbance imposes an additional load D on each component. If the sum of the initial load L_j of component j and the disturbance D is larger than a component load threshold L^{fail}, component j fails. This failure occurrence leads to the redistribution of an additional load P on the neighboring nodes which may, in turn, get overloaded and thus fail in a cascade which follows the connection pattern of the network system. As the components become progressively more loaded, the cascade proceeds.

The algorithm for simulating the cascading failures proceeds in successive stages as follows:

0. At stage $i = 0$, all N components are initially working under independent uniformly random initial loads $L_1,\ L_2\ , \ldots,\ L_N \in [L^{min}, L^{max}]$, with $L^{max} < L^{fail}$.

1. An initial disturbance D is added to the load of each component.

2. Each component that has not failed, is tested for failure: for $j = 1, \ldots, N$, if component j has not failed and its $L_j > L^{fail}$ then component j is removed.

3. The components loads are incremented taking into account the network topology, i.e. the failed component neighborhood: for each failed node, the load of its first-neighbors is incremented by an amount P. If the neighborhood set of the failed node is empty, the associated failure propagation comes to an end.

4. The stage counter i is incremented by 1 and the algorithm is returned to step 2.

The algorithm stops when failures are no further propagated and the damage caused by the cascade is quantified in terms of the number of network components which have failed, i.e. the cascade size S, when the propagation comes to an end. The cascade propagation algorithm is embedded in a Monte Carlo simulation framework, in which a large number of cascades is triggered for the same range of initial load, $[L^{min}, L^{max}]$, in order to obtain statistically significant results. The damage caused by the cascades for any initial load level, $[L^{min}, L^{max}]$, is quantified in terms of the number of network components which have failed on the average, i.e. the average cascade size, $\bar{S}$. The simulation is repeated for different ranges of initial load, $[L^{min}, L^{max}]$, with $L^{max} = 1$ and L^{min} varying from 0 to 1, and a point $(L, \bar{S})$ is drawn in a load-size diagram, so that the average critical load, L_{cr}, at which the phase transition between the absence of cascades and the emergence of cascades with significant size ($\bar{S} \geq S_{cr}$, e.g. involving a relevant fraction of network components) in the system can be identified. A typical example of the output of the cascading failure simulation is given in Fig. 2.1 for a fully connected network with $N = 1000$ nodes, $K = N(N-1)/2 = 499500$ and $P = D = 0.0004$.

The transfer of a fixed amount of load P to other (neighboring) components of the network upon failure of one of its components may be representative of those systems where each node equally contributes to the global system activity and following their progressive failures the same amount of damage is caused to the still working ones. For example, in biological systems the death of a neural cell leads to the release of a toxin and this, in turn, is responsible for the

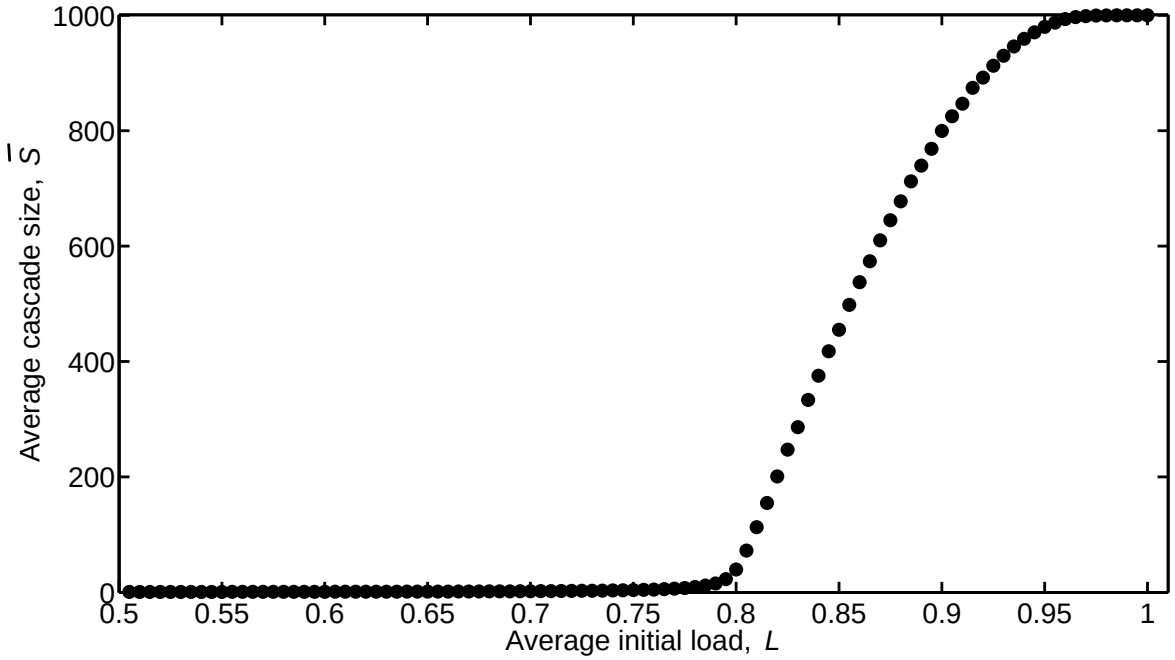

Figure 2.1: The typical output of the cascade algorithm for propagation of cascading failures in networks. The average cascade size $\bar{S}$, i.e., the number of failed nodes in a cascade event, with respect to the average initial component loading, L. Results for a fully connected network with $N = 1000$ nodes, $K = N(N-1)/2 = 499500$ and $P = D = 0.0004$.

death of many other cells (28). Thus, in some systems and under some operating conditions, it may be more realistic that the actual load previously carried by the now failed component is passed onto the other (neighboring) components in the network. To model such condition, step 3 of the cascade propagation algorithm is modified as follows (26):

3. The components loads are incremented taking into account the network topology, i.e. the failed component neighborhood: given the generic node j, failed under load $L_j > L^{fail}$, its load L_j is spread uniformly among its neighbors, by incrementing their load with an amount equal to L_j divided by the degree k_j of the failed node. If the neighborhood set of the failed node is empty, the associated failure propagation comes to an end.

In other words, with this modification, the load of the failed component is uniformly shared among its neighbors. It still holds that in case of an empty neighborhood, the load is no longer propagated and the cascade is stopped in that direction.

Chapter 3

Deterministic representation of cascading failures

It is important to characterize cascade spreading for interconnected distributed systems, such as power transmission (29), communication (30), transportation (31), social (11), and metabolic (32) networks. In these networks, the physical connections or logical relationships are represented by links. For example, in a power transmission system, overhead lines represent physical connections between substations or generators while operational procedures are logical dependencies. The interaction and growth of such networks with different connectivities, network topologies, interaction rules, and adaptive responses are usually categorized by their cascade spreading behavior (33).

A failure cascade is initiated by a disturbance that imposes an additional load D on each component. If the sum of the initial load L_j of component j and the disturbance D is larger than the load threshold L^{fail}, that component fails. This local failure leads to the redistribution of an additional load P on the neighboring nodes which may, in turn, also become overloaded and thus fail, thus forming a cascade which proceeds as additional components are progressively loaded and similarly fail along the connections of the network.

Cascade failures in networks can be analyzed using deterministic methods (34; 35), stochastic Monte Carlo simulations (36), or hybrid models that simulate scale-free behaviors (37). The load carried through a network can be correlated with the internal connectivity in terms

of the number of shortest paths passing through a specific node (24; 25; 38). In general, the distribution of the number of failed nodes in a network has a power-law behavior at a critical saturation loading (27; 39). Higher loadings lead to a greater probability of complete failure depending upon the network topology (26). Moreover, numerical simulations of cascading failures, e.g., to assess the robustness of large distributed systems, are oftentimes not feasible due to the heavy computational burden that arises from the evaluation of all possible network paths between a specific node and all other nodes in the network.

We present a model to predict cascade spreading as a function of the network topology and the network loading conditions, the results of which can be used to redesign the network links and nodes to assess the critical load and the rate of spreading. The model considers an arbitrary interconnected system of N identical components that each have random initial loads $L^{min} < L < L^{max}$. All components have the same limit of operation L^{fail} beyond which they fail. In a typical cascade process, when a component fails, a fixed positive load P is transferred to each of the other system components (27). We assume that this overload propagates locally to first-neighbors of the failed node in the network structure (26). In case there is no working node in the neighborhood of a failed component, the cascade spread in that direction ceases.

Our model differs from similar studies such as (24) since it does not rely on the assumption that the load on a component is proportional to the number of shortest paths running through it, which do not always reflect the actual routes of the flow in a network. On the contrary, it shares a similarity with the fiber bundle model in complex networks which has been applied to the blackout scenarios for cascading breakdown of power plants from overloading (40). Similar to the fiber bundle model, if the load in a node exceeds its capacity, that node is disconnected from the network and the stress/load is transferred locally to neighboring nodes through the edges of the network. Moreover, while the vertices are damaged, the underlying network is rigid . This means that the connections among the nodes act as load carriers but are unaffected by its propagation.

3.1 Cascade numerical algorithm

Following the approach detailed in Section 2.4, the algorithm for numerically simulating cascade spreading proceeds in successive stages as follows:

1. At the initial stage $i = 1$, all N nodes of the network are assumed to be functionally working under independent uniformly random initial loads $L_1, L_2, ..., L_N \in \left[L^{min}, L^{max}\right]$ with $L^{max} < L^{fail}$;

2. At $i = 1$, an initial disturbance D is added to the load on each node;

3. All working nodes are examined for failure: for $j = 1, ..., N$, if $L_j > L^{fail}$, then node j is assumed to also have failed;

4. The component loads are incremented taking into account the neighborhoods of the failed nodes: for each failed node, the load of its first-neighbors is incremented by an amount P; if the neighborhood set of the failed node is empty, the associated failure propagation ceases;

5. The stage counter i is incremented by 1 and the algorithm is returned to step 2.

The algorithm stops when failures are no longer able to propagate. The damage caused by the cascade is quantified in terms of the number of network components which have failed, i.e. the cascade size S, when the propagation comes to an end.

The cascade propagation algorithm is embedded in a Monte Carlo simulation framework, in which a large number of cascades, e.g. 10,000 in this study, is triggered for the same range of initial load, $[L^{min}, L^{max}]$, in order to obtain statistically significant results for various realizations of the same average loading condition. The damage caused by the cascades for any initial load level, $[L^{min}, L^{max}]$, is quantified in terms of the number of network components which have failed on the average, i.e. the average cascade size, $\bar{S}$. The simulation is repeated for different ranges of initial load, $[L^{min}, L^{max}]$, with $L^{max} = 1$ and L^{min} varying from 0 to 1, and the pair $(L, \bar{S})$ is recorded.

The algorithm is applied to simulate various networks that have $N = 50$ nodes but different numbers of connections K. Twenty-four small-world networks with $n = 2$ to 49

initially connected first neighbors and thirteen Erdős-Rényi random networks with rewiring probabilities ranging from 0.07 to 1 are constructed using a previously described algorithm that spans the feasible connectivity range (41). The use of two different network models increases the fidelity of our deterministic representation of cascading failures. Thus, the representation is not limited to the dynamics of a specific class of network models.

To construct a network exhibiting small-world properties, we begin by accommodating its N nodes on a ring. Initially, each node is linked to its n first-neighbors, i.e. the first n nodes encountered starting from each node and moving both clockwise and counter-clockwise. As a result of this process, each node is connected to other $2n$ nodes, forming a very regular network. The last step is the randomization of the connectivity where connections are established bridging parts of the network which were previously far away. With a probability p, the $K = 2nN$ connections are rewired, i.e. one or both extremities of a connection may be switched to new randomly chosen nodes so that distant nodes that were originally not connected may now be linked. Multiple connections between the same pair of nodes and self-connections are not allowed. The probability p affects the degree of randomness of the network. If p assumes small values, the network presents a very regular structure with strong local connectivity, granted by the initial linking of each node to the first n neighbors. On the other hand, if p is large, the initially formed clusters are disrupted and the connectivity is completely random. The small-world properties appear for intermediate values of p. In this case, the local highly-clustered structure is preserved during the randomization while at the same time this process establishes new connections among distant areas of the network, enhancing the global connectivity efficiency.

The Erdős-Rényi model describes completely random networks. To construct Erdős-Rényi networks, we start with N unconnected nodes and link each pair of nodes in the network with probability p. Multiple connections between the same pair of nodes and self-connections are not allowed. Since the maximum number of connections in a network of N nodes is $\binom{N}{2} = N(N-1)/2$, the average number of connections K in a Erdős-Rényi network will be $K \cong p\binom{N}{2}$ and a fully-connected network is obtained when $p = 1$. Thus, the global connection efficiency can be varied through the probability p, i.e. larger p values

will correspond to higher global connection efficiency.

The propagation of cascading failures was simulated in the thirty-seven networks whose structural characteristics are presented in Table 3.1, columns 1 and 2, with respect to the number of links K and the global connectivity efficiency, E_{glob}. The significance of the parameters in columns 3 and 4 will be highlighted shortly in this section and in the next Section 3.2.

Table 3.1: Characteristics of the thirty-seven networks of $N = 50$ nodes employed to build the deterministic representation of cascading failures. From left to right, the structural indicators, i.e. the number of links K and the global efficiency E_{glob}, and the parameters related to the propagation of cascading failures, i.e. the exponential growth α and the critical load L_{cr} are displayed.

Connections (K)	**Efficiency ($\mathbf{E_{glob}}$)**	**Exponential growth (α)**	**Critical load ($\mathbf{L_{cr}}$)**
1225	1.0000	29.2742	0.8057
1200	0.9898	29.5146	0.8100
1150	0.9694	30.9652	0.8144
1100	0.9490	31.6224	0.8202
1100	0.9490	32.4772	0.8211
1007	0.9110	33.3727	0.8339
1000	0.9082	33.8846	0.8336
882	0.8600	36.7260	0.8486
772	0.8151	39.9213	0.8625
750	0.8061	41.7613	0.8658
635	0.7592	46.0659	0.8807
550	0.7243	47.2662	0.8903
511	0.7086	48.4629	0.8960

Continued on Next Page...

Table 3.1 – Continued

Connections (K)	**Efficiency ($\mathbf{E_{glob}}$)**	**Exponential growth (α)**	**Critical load ($\mathbf{L_{cr}}$)**
500	0.6735	48.1508	0.8995
450	0.6837	50.3283	0.9037
400	0.6624	54.9294	0.9101
389	0.6581	52.9331	0.9120
350	0.6410	56.4050	0.9169
300	0.6162	55.9119	0.924
300	0.5143	58.4100	0.9257
263	0.5951	57.0410	0.9292
250	0.5868	60.6762	0.9310
250	0.5546	60.8320	0.9315
250	0.5368	60.3460	0.9322
250	0.4619	59.1162	0.9323
235	0.5754	60.8140	0.9330
200	0.5442	61.6369	0.9374
200	0.5423	61.7461	0.9377
171	0.5144	61.5122	0.9413
150	0.4891	62.5366	0.9447
150	0.3351	61.7302	0.9457
128	0.4457	62.5255	0.9473
100	0.4084	67.2024	0.9512
100	0.2548	62.8720	0.9518
100	0.3737	63.3629	0.9516
89	0.3555	62.9908	0.9525
50	0.2187	63.7783	0.9579

We assume that each system operates in such a manner that the initial component loadings vary from $L^{min} = 0$ to $L^{max} = L^{fail} = 1$. Thereafter, the average component loading $L = \left(L^{min} + 1\right)/2$ is raised by increasing L^{min}. The average component loading, L, provides information on the initial working conditions of the network in which the cascade is triggered. Large L values represent highly-loaded systems, where each component is operating on the average close to its limit capacity, $L^{fail} = 1$. We normalize the range of loading conditions from 0 to 1 so that the model for cascading failure is not limited to the propagation of failures in specific applications. The normalized loads describe the propagation of an 'abstract' cascade of failures. Then, for specific applications, the range of loading conditions is scaled to describe the dynamics of the actual physical quantities spreading for the network being analyzed. Since varying loading conditions are explored only through the variation of L^{min} from 0 to 1, the average initial load, L, lies in the range from 0.5 to 1. $L = 0.5$ describes the lowest possible loading condition in the network in which the components can assume all the possible loads between 0 and 1 with an uniform probability. Conversely, $L = 1$ describes the highest possible loading conditions in which all of the components operate at their limit capacity and stop functioning in the next time step.

The values of the parameters which govern the outbreak and the propagation of the cascade, i.e. D and P, respectively, must be determined in the context of the specific failure propagation to be represented. Larger D values result in many more component failures at the initial stage of the cascade. Large P values facilitate the spreading of the failure cascade to a large number of components, since a large overload, P, is transfered to the neighborhood of a component, upon its failure. Herein, the initial disturbance D and the load transfer amount P are set equal to 2% and to 7% of the failure load L^{fail}, respectively. This choice of the cascade parameters results in few initial failures at the outbreak of the cascade while allowing its propagation to a large number of components during the next steps. This occurs in particular when the system operates at high loading conditions. Thus, the effects that the initial loading conditions, L, have on the propagation of the cascading failure can be clearly identified.

Figure 3.1 presents the simulation results of the algorithm for cascading failure propagation. The mean number of failed components $\bar{S}$, which is the cascade size, is plotted as a

function of the average initial component loading L for four networks that have decreasing connectivity levels. The results show how system loading can influence the risk of cascade spreading. At low loadings, there is a trailing tail for small values of $\bar{S}$ in the distribution of the number of failed components. The longer this tail, the lower the susceptibility of a network to large cascading failures. There is a sharp change in the gradients of these tails at a critical loading L_{cr} that marks the transition between the non-cascading ($L < L_{cr}$) and cascading ($L > L_{cr}$) regions. This loading identifies the safe and critical failure-prone working conditions for a network, since the likelihood of large cascading failures increases significantly when $L > L_{cr}$. We have assumed that L_{cr} is the initial loading which leads to a cascade involving 10% of system constituents, i.e. $S_{cr} = 5$ components for the $N = 50$ networks. The actual choice of the maximum fraction of network components whose failures can be tolerated, S_{cr}, depends on the physics of the specific network whose failure dynamics are analyzed. In this study, the fraction 10%, leading to $S_{cr} = 5$ components, is selected to clearly display the effects that different connectivity patterns have on the dynamics of cascading failures. Figure 3.1 also shows that the response of $\bar{S}$ to varying L is similar for networks with the same number of nodes even though they may have different connectivities.

The critical load, L_{cr}, is a relevant feature of a network system since it identifies, together with the continuous change in gradient, a type-two transition (42) between the cascade-safe region ($L < L_{cr}$) and the onset of disrupting cascades ($L \geq L_{cr}$) in terms of the loading conditions, L. Along with the average cascade size, $\bar{S}$, it provides essential information on the system vulnerability towards cascading failures and it can help in identifying safety margins of system operation. L_{cr} presents the same range of variability as $L \in [0.5, 1]$. $L_{cr} = 0.5$ implies that no cascade-safe region can be identified for the network. Hence, cascade of significant size, i.e. $S \geq S_{cr}$, will occur no matter how small the initial loading condition L is going to be. On the other hand, $L_{cr} = 1$ implies that the cascade-safe region spans the whole range of possible loading condition in the network. In this case, the only possibility for cascades of significant size to propagate, i.e. $S \geq S_{cr}$, is to force all the components to operate to their limit capacity $L^{fail} = 1$.

When the average loading, L, of a network approaches the critical value, L_{cr}, failure cascade of significant sizes start propagating in the system. At this critical loading condition

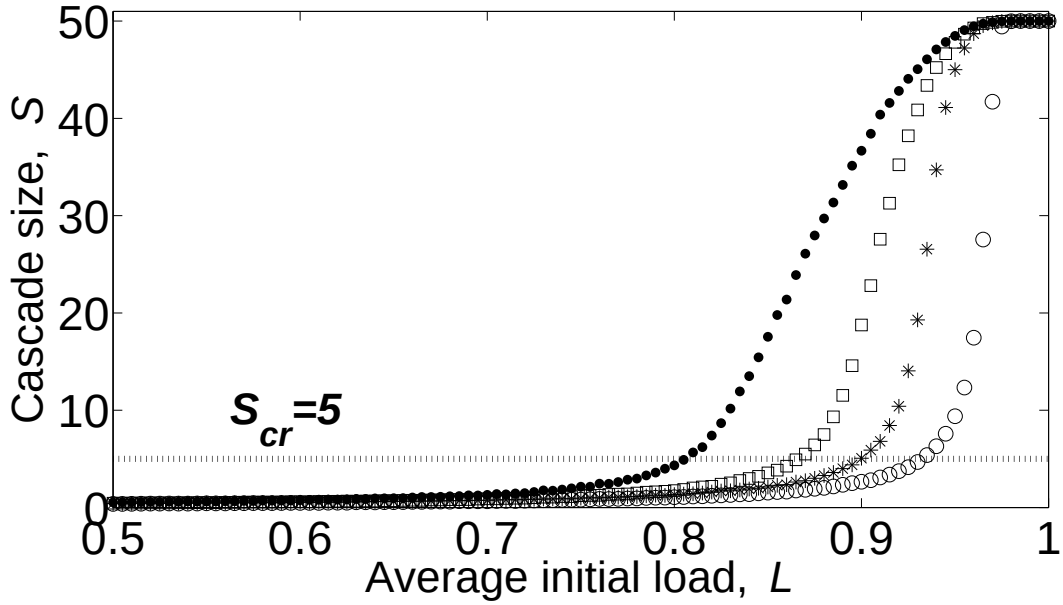

Figure 3.1: Cascade size $\bar{S}$, i.e., the number of failed nodes in a cascade event, with respect to the average initial component loading, L. From left to right we consider networks with equal numbers of nodes $N = 50$, but with decreasing numbers of connections $K = 1225, 750, 500, 250$ and global connectivity efficiency, $E_{glob} = 1, 0.8061, 0.6735, 0.4619$. The critical load L_{cr} for a network is identified at 10% of complete network failure line, i.e., at $S_{cr} = 5$.

the probability distribution function of the cascade size, S, develops a power-law tail for large S values (27; 39). This points towards a finite probability for large cascades to be triggered at this loading conditions. The power-law tail is shown in Fig. 3.2 where the probability distribution function of the cascade size, S, at the critical load $L = L_{cr} = 0.9377$ is presented for the network in Tab. 3.1 with $K = 400$ and $E_{glob} = 0.5423$. Hence, it is important to stress that even at the critical point L_{cr}, which marks the upper bound of the cascade-safe region, cascades of very large size ($S = 41$, i.e. 82% of the system size $N = 50$) appear, even if their frequency is extremely low ($1.4 \cdot 10^{-5}$).

As we have seen from Fig. 3.2, cascades of significant size, i.e. $\bar{S} > S_{cr}$, propagate in the system even at $L = L_{cr}$. This is not surprising since the average critical load, L_{cr}, is estimated as the average of 10,000 simulations. Indeed, the model itself is devised to evaluate average indicators from the stochastic loading conditions that are simulated. Thus, the capabilities of the critical load, L_{cr}, as a reliable indicator of the vulnerability of the network towards the spreading of cascading failures should be assessed. Figure 3.3 shows the probability that a cascade having size smaller that the critical cascade size, i.e. $Prob(S < S_{cr})$, is generated for the all the possible average initial loads, $L \in [0.5, 1]$. The probability follows the same trend as the average cascade size, $\bar{S}$ with a long trailing tail for small average initial loads, L, followed by a transition to low probabilities of cascades smaller that the critical size, $Prob(S < S_{cr})$, for large average initial loads. The plot has been generated for the network with $K = 400$ and $E_{glob} = 0.5423$ in Tab. 3.1. Interestingly, at the critical load, $L = L_{cr} = 0.9377$, 63% of the generated cascading failures are smaller than the critical size, S_{cr}. Therefore, although the use of the average cascade size, $\bar{S}$, is well established in the literature to describe the increasing magnitude of cascading failures as the system loading conditions increase, its use as a vulnerability indicator may be questionable. The use of the probability of not exceeding the critical cascade size, $Prob(S < S_{cr})$, seems to be more suitable instead.

As it can be seen from Fig. 3.1, the average cascade size, $\bar{S}$, has small values until it reaches the proximity of the critical load, L_{cr}, beyond which the transition to cascade region occurs as an exponential growth. We also see from Fig. 3.2 that a cascade of significant size propagate in the network even below the critical load, L_{cr}. Thus, the use of the critical load as a vulnerability indicator needs to be gauged against the sensitivity of detecting small

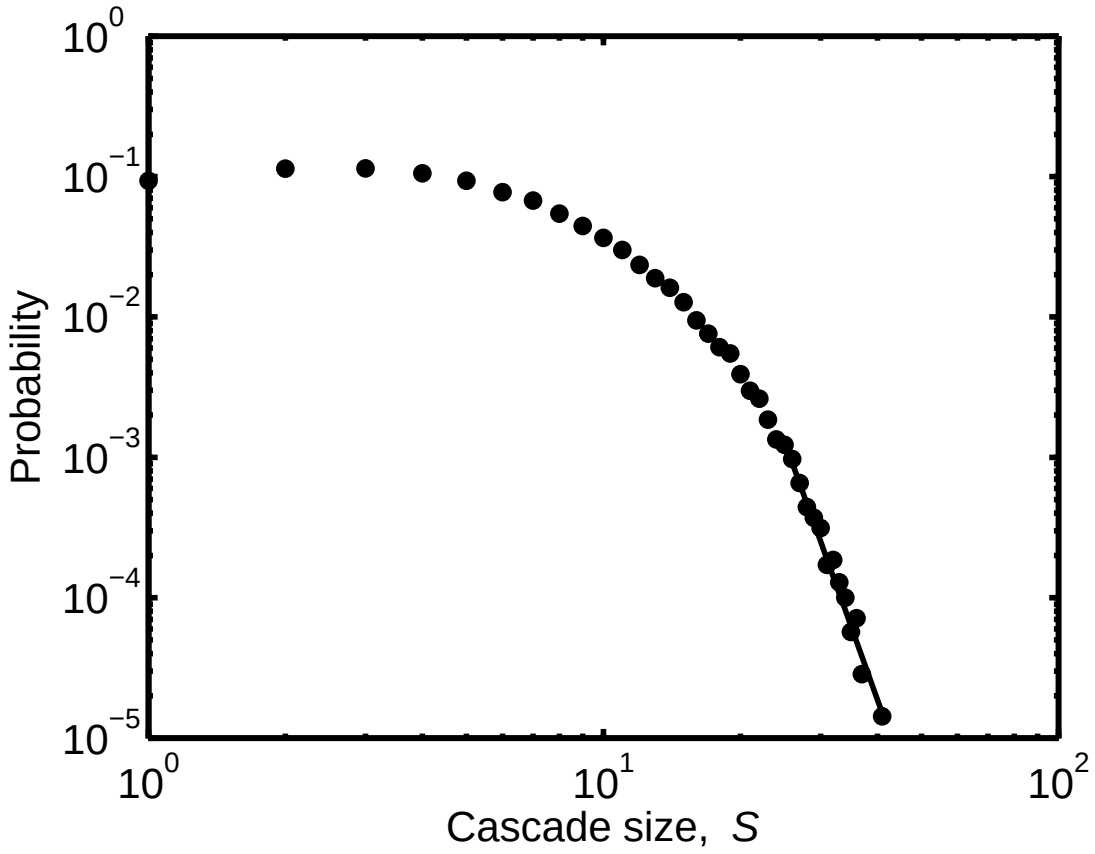

Figure 3.2: The probability distribution function of the cascade size, S, at the critical load $L = L_{cr} = 0.9377$ for the network with $K = 400$ and $E_{glob} = 0.5423$ (see Tab. 3.1). For large S, the probability distribution shows a power-law tail, $p(S) \sim S^{-9.00}$, which attests the propagation of failure cascade having significant size in the network. This plot was obtained using 10,000 failure cascades simulated within a Monte Carlo framework for the average initial load, $L = L_{cr} = 0.9377$.

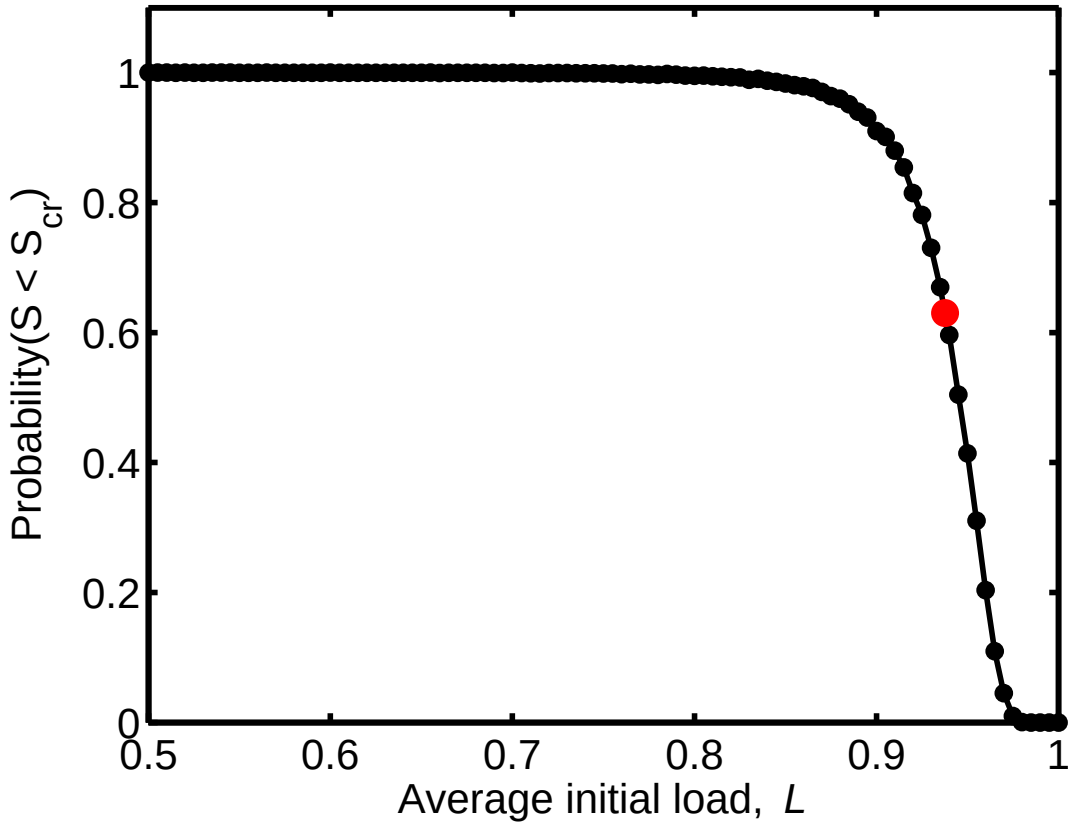

Figure 3.3: Probability that the cascade size, S, is smaller that the critical cascade size, S_{cr}, i.e. $Prob(S < S_{cr})$, for the all the possible average initial loads, $L \in [0.5, 1]$. The red marker highlights how for the critical load, $L = L_{cr} = 0.9377$, the 63% of the generated cascading failures are smaller than the critical size, S_{cr}. For each average initial load, L, 10,000 failure cascades were simulated in the network with $K = 400$ and $E_{glob} = 0.5423$ (see Tab. 3.1).

changes in its value. Then, appropriate countermeasures of reducing the working load for limiting the failure propagation can be taken as the operation conditions are approaching the critical load L_{cr}.

3.2 Deterministic predictive model

As seen in Section 2.2, the global connection efficiency is introduced as a measure of the reachability of the constituent parts of a network (18). As we have noticed from Fig. 3.1, the network responses to cascading failure propagations, in terms of the critical load, L_{cr}, and of the exponential transition towards the cascade region, scale with the numbers of connections and, thus, with the global connection efficiency. Hence, the global connection efficiency can be used to predict the effect of the network connectivity on the cascade spreading. To quantify this quantity, the network of N nodes connected by K links or arcs is first represented as a graph $G(N, K)$ that is defined by an $N \times N$ adjacency (connection) matrix $\{a_{ij}\}$ whose entries are 1 if there is an unbroken link between nodes i and j, or 0 otherwise (for sake of illustration, the results presented herein are for networks with $N = 50$).

The matrix of the shortest path lengths between nodes i and j, $\{d_{ij}\}$, is then evaluated using the Floyd algorithm (16), which performs the minimization with respect to all the possible paths, γ_{ij}, from every node i to any other node j. The matrix $\{d_{ij}\}$ contains the values

$$d_{ij} = \min_{\gamma_{ij}} \left(1 \Big/ \sum_{mn \in \gamma_{ij}} a_{mn} \right), \tag{3.1}$$

where the minimization is performed with respect to all paths γ_{ij} linking these nodes and the sum extends to all the edges formed by each of these paths. Thus, $1 \leq d_{ij} \leq \infty$, where the lower value denotes the existence of a direct link connecting i and j and the upper value applies when no paths connect the two nodes. The distance d_{ij} counts the numbers of links in the shortest path from node i to node j. Thus, it is called 'topological' distance since additional link features, such as their lengths or their reliabilities, are not considered.

The global efficiency $E_{glob}(G)$ is defined as being inversely proportional to the distance of the shortest path linking nodes i and j, i.e. (18),

$$E_{glob}(G) = \left(\sum_{i \neq j \in G} 1/d_{ij} \right) / \left(N(N-1) \right). \tag{3.2}$$

This topological lumped parameter characterizes the global connectivity of the network. Since the shortest path length between nodes i and j, $d_{ij} = 1$ when there is one direct link in the graph which connects nodes i and j, $E_{glob}(G)$ is equal to one in case of a perfectly connected network, in which a direct connection between any pair of nodes exists. It is not possible to establish an one-to-one correspondence between the global connectivity efficiency, E_{glob}, and the number of links, K, in a network. Different E_{glob} may characterize networks having the same number of links K due to the variability in the possible connectivity patterns. Furthermore, the evaluation of the number of the possible connectivity patters which can be realized in a network given the number of nodes, N, and links, K, is a combinatorial problem. In a network of N nodes, $K_{max} = \binom{N}{2} = N(N-1)/2$ links can be accommodated at most. These are all the combinations of N nodes taken 2 at a time, i.e. the maximum number of pairs which can be obtained from N nodes. When the network contains $K < K_{max}$ links, only K pairs are selected among the possible $N(N-1)/2$. Hence, the number of connectivity patterns arising from the ways to accommodate K links on $N(N-1)/2$ available sites is

$$\binom{\binom{N}{2}}{K} = \binom{N(N-1)/2}{K}. \tag{3.3}$$

Figure 3.4 presents the global connectivity efficiency values, E_{glob}, obtained placing K connections among the $N = 50$ network nodes. Each black dot is a realization of a connectivity pattern involving K connections and one hundred patterns are generated for each K. The red curve represents the average global connectivity efficiency, E_{glob}, for the considered numbers of connections, K. The maximum number of links that can be accommodated in the network of $N = 50$ nodes is $K_{max} = 1225$. When $K = 0$ and $K = K_{max}$, only one connectivity pattern can be realized, as predicted by Eq. 3.3 which reads $\binom{N(N-1)/2}{0} = 1$ and $\binom{N(N-1)/2}{N(N-1)/2} = 1$, respectively. It is interesting to notice that the variability found in Fig. 3.4 with respect to E_{glob} is not reflected in Eq. 3.3 with respect to the possible connectivity patterns. In particular, while on one hand Eq. 3.3 is symmetric about the $K = K_{max}/2$ axis, thus predicting the same variability in the connectivity patterns, e.g. for $K = 50$ and

$K = 1175$, on the other hand in Fig. 3.4 we see that this variability affects the connectivity efficiency, E_{glob}, only for poorly connected networks. In networks with few links, different areas of the system may be connected or not depending on the connectivity patterns of the network, resulting in higher or lower connectivity efficiency values, respectively. Conversely, networks with many links are less affected by the connectivity pattern since good network connectivity is already provided by the large number of connections. As a result of this, from Fig. 3.4 we can see that $E_{glob} \in [0.1444, 0.2413]$ for $K = 50$, while only the value $E_{glob} = 0.9800$ was obtained during the one hundred realization for $K = 1175$.

The nonlinear relation between the global connectivity efficiency, E_{glob}, and the network links, K, presented in Fig. 3.4 allows drawing some structural consideration about improving E_{glob}. In particular, we can see that 60% of the maximum global connectivity efficiency is attained with $K = 272$ links, not even 23% of the links required to build a fully connected network. This is due to the fast growth of E_{glob} occurring in poorly connected networks as more links, K, are employed. The fast initial growth is followed by a slower linear growth past $K = 272$ links. The residual 40% of the global connectivity efficiency is attained with the addition of the remaining 77% of the maximum possible network links. Therefore, we can conclude that it is easier to increase the global connectivity efficiency in a network with fewer connections, i.e. $K < 272$ for the case $N = 50$, than in a well-connected network. By the same token, an improvement plan aiming at increasing the connectivity K of the network is much more effective in systems having fewer connections.

The deterministic model is devised to predict the network responses to cascading failure propagations, in terms of the critical load, L_{cr}, and of the exponential transition towards the cascade region with α growth rate, using the structural information provided by the global connectivity efficiency, E_{glob}. The increase in the average number of failed components in a cascade $\bar{S}$ for $L > L_{cr}$ is represented through the deterministic relation

$$\mathrm{d}\,\bar{S} / \mathrm{d}\,L = \alpha\,(E_{glob}) \cdot \bar{S}. \tag{3.4}$$

The coefficient α represents an exponential growth in cascade size, $\bar{S}$, and is assumed to be related to the global efficiency, E_{glob}. This coefficient is a measure of how fast the disruption following a cascading failure increases as the average initial load L increases past

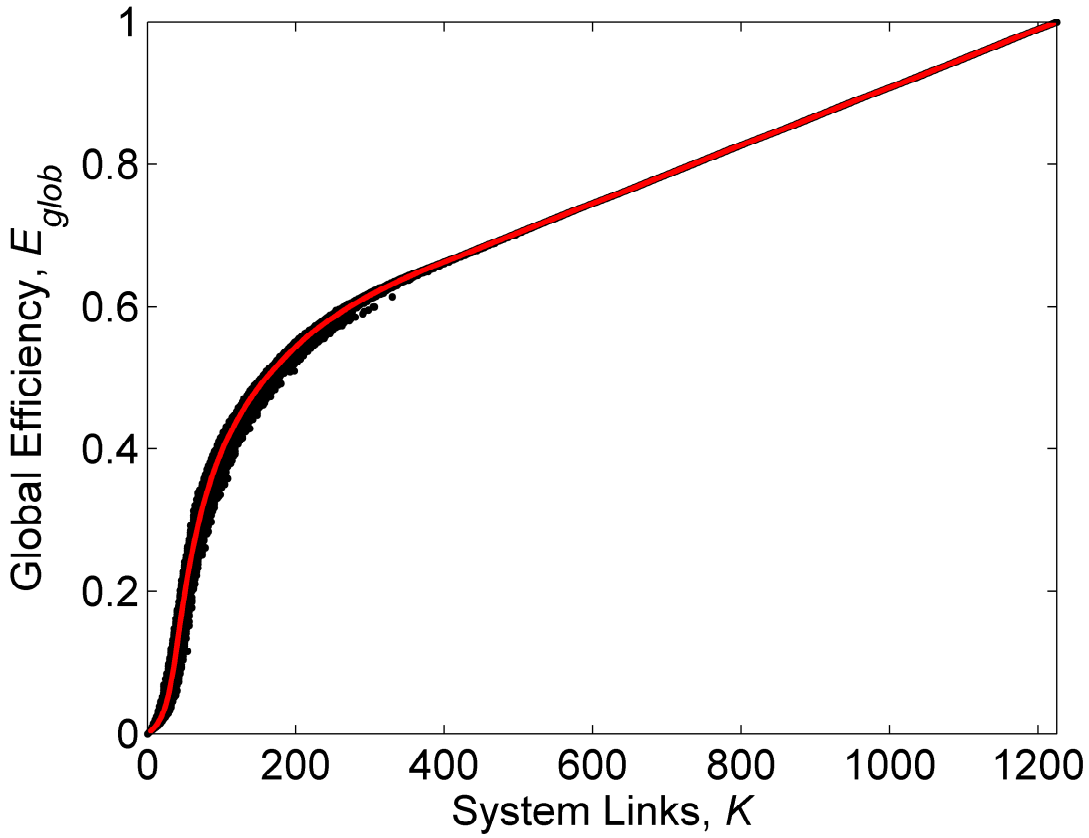

Figure 3.4: The global connectivity efficiency values, E_{glob}, obtained placing K connections among the $N = 50$ network nodes. Each black dot is a realization of a connectivity pattern involving K connections and one hundred patterns are generated for each K. The red curve represents the average global connectivity efficiency, E_{glob}, for the considered numbers of connections, K. The maximum number of links that can be accommodated in the network of $N = 50$ nodes is $K_{max} = 1225$.

the critical load, L_{cr}, and is a function of the system connectivity identified by E_{glob}. The larger the α growth rate, the sharper the transition from cascade-safe to cascade-prone region will be.

Following the results of Fig. 3.1, we assume that the critical load, L_{cr}, is also a function of E_{glob}. L_{cr} corresponds to a state at which 10% of the system components have failed, $\bar{S}\,(L = L_{cr}) = \bar{S}_{cr} = 5$. Our objective is to find the relations between E_{glob} and the model parameters α and L_{cr}, i.e. $\alpha = f(E_{glob})$ and $L_{cr} = f(E_{glob})$.

From Eq. 3.4, it is clear that the model does not consider the saturation of the cascade size, S, towards its maximum value, i.e. the network size, N. Indeed, this behavior is much less critical than the exponential growth in the cascade size occurring after the critical load, L_{cr}. While the former occurs when the majority of the network component is already failed and it is due to an obvious physical limitation in the cascade size for $S = N$, the latter involves the transition from the cascade-safe region to loading conditions where cascading failures of significant sizes propagate.

3.3 Results and discussion

Numerical simulations of cascading failures are performed for the thirty-seven networks presented in Tab. 3.1 based on the algorithm described in Section 3.1. These result in various $\bar{S}$ vs. L cascading behaviors, four of which are shown in Fig. 3.1. For these thirty-seven simulations of cascading failure propagations, the critical load, L_{cr}, is evaluated from diagrams similar to those presented in Fig. 3.1, at the intersection with the line $\bar{S} = S_{cr}$, i.e. $\bar{S}(L = L_{cr}) = S_{cr}$. The values of the critical load, L_{cr}, for the simulated propagations are presented in Tab. 3.1 column 4.

Following the model assumption of exponential growth in the cascade size at the critical load, L_{cr}, stated in Eq. 3.4, the value of α is determined through least square regression analysis of the propagation of cascading failures in the thirty-seven networks. The procedure applied to evaluate the growth rate α is detailed in Figs. 3.5 and 3.6. Starting from the critical load, L_{cr}, increasing numbers of points $(L, \bar{S})$ in the diagram $\bar{S} = f(L)$ are employed to fit exponential functions. Figure 3.5 shows the Pearson correlation coefficient, r^2, for

the performed regressions versus the maximum average initial load, L, included in the least square fit, for the network with $K = 882$ and $E_{glob} = 0.8600$ in Tab. 3.1. As the maximum average initial load increases, a larger number of regression values are included in the analysis. In all the considered propagations, the correlation coefficient r^2 initially decreases and then shows a maximum for a regression sample having maximum average initial load, L. After the maximum, the correlation coefficient decreases since the exponential function cannot fit the saturation of the cascade size, S, towards its limit value, i.e. the system size N. The growth rate, α, which corresponds to the exponential function having the best correlation coefficient is chosen as the best representative of the growth of the average cascade size, $\bar{S}$, beyond the critical load, L_{cr}. Figure 3.6 shows the growth rate α of the fitted exponential versus the maximum average initial load, L, included in the least square fit, for the network with $K = 882$ and $E_{glob} = 0.8600$ in Tab. 3.1. In particular, from Fig. 3.5 we can see that the least square regression correlation coefficient r^2 has a maximum for the exponential fit obtained from the sample with maximum average initial load, $L = 0.895$. Therefore, we choose the corresponding $\alpha = 36.7260$ in Fig. 3.6 to model the exponential growth of the cascade size, S. The values of α for the simulated propagations are reported in Tab. 3.1 column 3.

The estimated values of α and L_{cr} accurately reproduce the simulation results, particularly at the transition L_{cr} that is a critical feature of the plot. Figure 3.7 shows the simulation results for the propagation of cascading failures in one network in Tab. 3.1 with $K = 400$ and $E_{glob} = 0.5423$ and the corresponding exponential function fitted using the least square regression starting from the critical load, $L_{cr} = 0.9377$. The estimated growth rate is $\alpha = 61.7461$. These values of the critical load, L_{cr}, and growth rate α, together with those from the other thirty-six networks, are used to establish the two relations $\alpha = f(E_{glob})$ and $L_{cr} = f(E_{glob})$ that are the backbones of the deterministic predictive model in Eq. 3.4.

Before network failure occurs, at least some nodes of the network are initially reachable from some others. This connection property is represented by the global efficiency (and in turn by $f(\alpha)$ and $f(L_{cr})$). The relations between E_{glob} and the model parameters are obtained through a least square regression analysis of the simulations, as shown in Fig. 3.8 and Eq. 3.5 and in Fig. 3.9 and Eq. 3.6, respectively, i.e.,

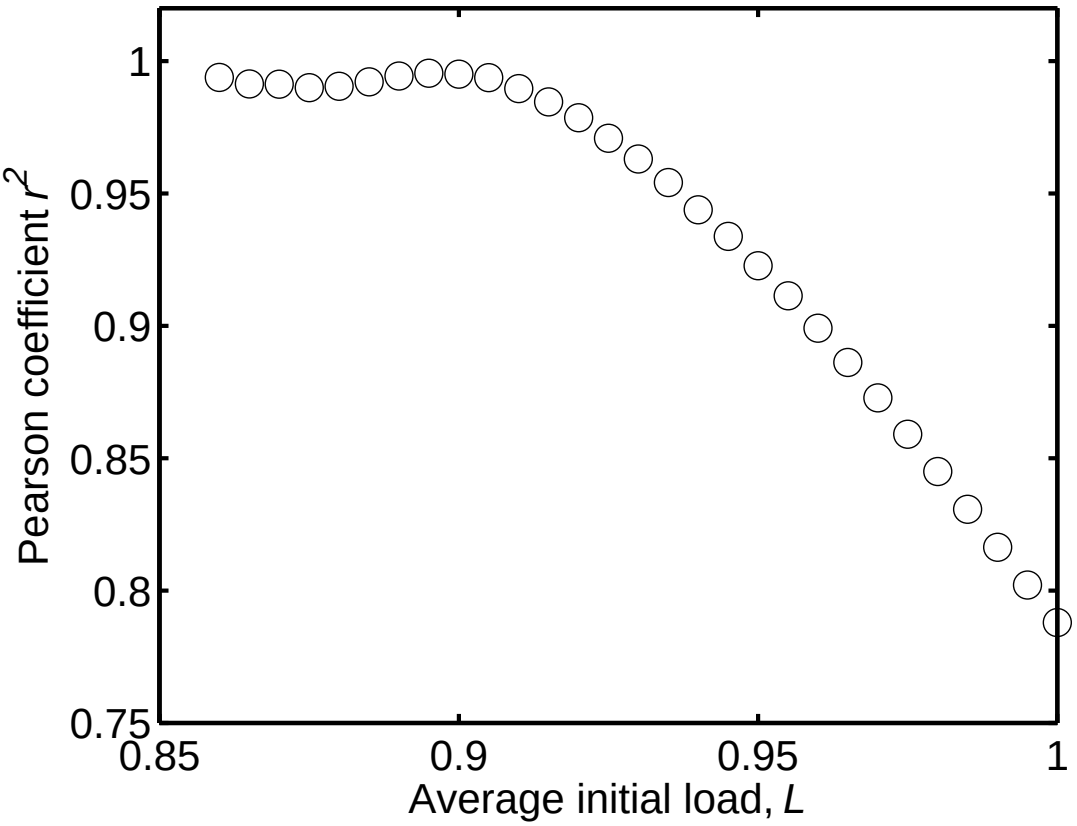

Figure 3.5: The Pearson correlation coefficient, r^2, for the least square regressions employing exponential functions, versus the maximum average initial load, L, included in the least square fit, for the network in Tab. 3.1 with $K = 882$ and $E_{glob} = 0.8600$. The corresponding regression sample sizes ranges from 3 for $L = 0.86$ to 31 for $L = 1$. r^2 has a maximum for $L = 0.895$.

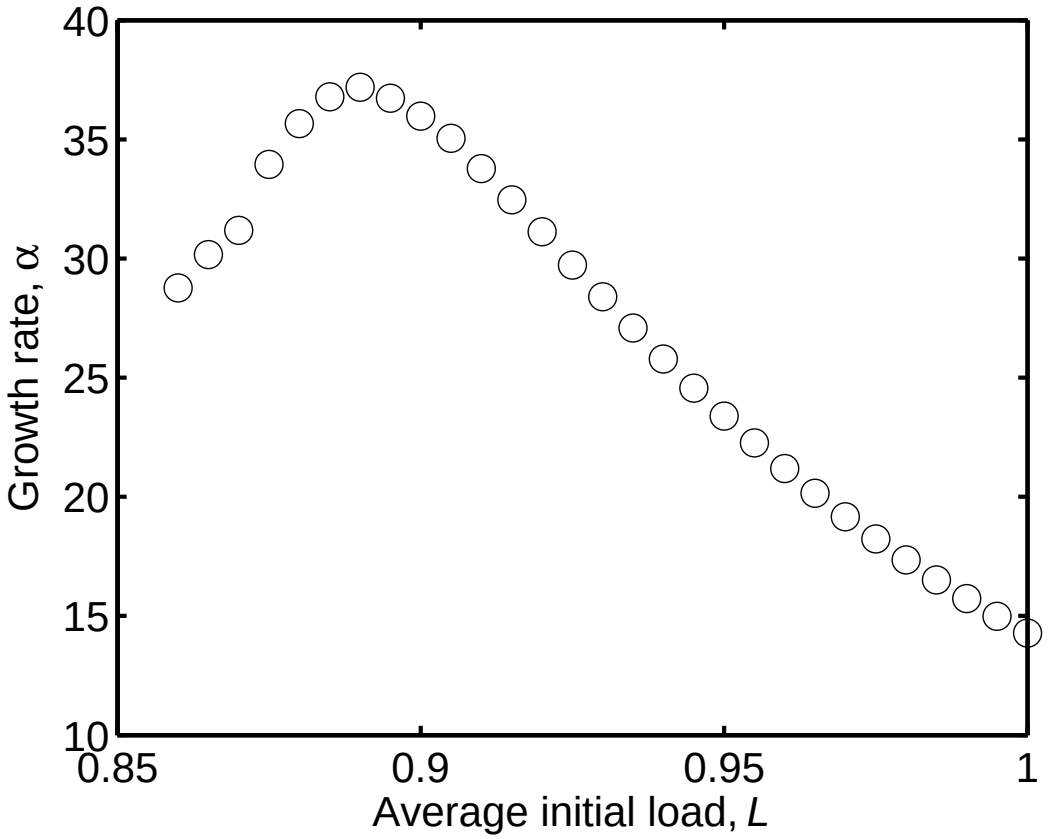

Figure 3.6: The growth rate α of the fitted exponential versus the maximum average initial load, L, included in the least square fit, for the network in Tab. 3.1 with $K = 882$ and $E_{glob} = 0.8600$. The corresponding regression sample sizes ranges from 3 for $L = 0.86$ to 31 for $L = 1$. Since r^2 has a maximum for $L = 0.895$, the value $\alpha = 36.7260$ is selected as the best fit for the exponential growth of the cascade size, S.

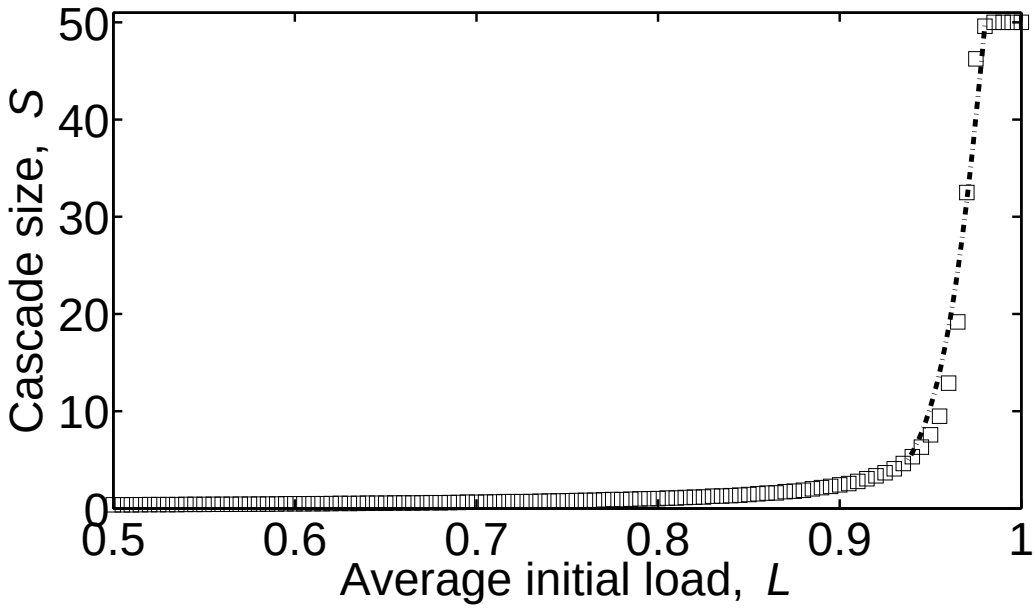

Figure 3.7: Simulation results for the propagation of cascading failures in one network in Tab. 3.1 with $K = 400$ and $E_{glob} = 0.5423$ (squares). The dash dotted curve shows the exponential function fitted using the least square regression starting from the critical load, $L_{cr} = 0.9377$. The estimated growth rate is $\alpha = 61.7461$.

$$\begin{cases} L_{cr} = -0.3046 \cdot E_{glob} + 1.1106 & 0.56 < E_{glob} < 1 \\ L_{cr} = -0.0722 \cdot E_{glob} + 0.9742 & E_{glob} < 0.56 \end{cases} \tag{3.5}$$

and

$$\begin{cases} \alpha = -74.12 \cdot E_{glob} + 101.9 & 0.56 < E_{glob} < 1 \\ \alpha = -9.47 \cdot E_{glob} + 66.18 & E_{glob} < 0.56 \end{cases} \tag{3.6}$$

Two bilinear relations are identified for $\alpha = \alpha(E_{glob})$ and $L_{cr} = L_{cr}(E_{glob})$. Systems at larger E_{glob} values are more sensitive to small variations in this parameter. Conversely, the values of α and L_{cr} are somewhat invariant for smaller E_{glob} systems indicating that the failure cascade no longer depends on the system configuration. This is due to the fact that α and L_{cr} cannot grow indefinitely but must be physically bounded. Figures 3.8 and 3.9 show that, on one hand, cascading failure occurs at larger L_{cr} as E_{glob} decreases, or as the system becomes less connected. On the other hand, as E_{glob} decreases, the transition from the cascade-safe region to the cascade-prone region becomes sharper, due to the increase of the growth rate α. In this respect, Figs. 3.8 and 3.9 allow identifying a convenient network connectivity, E_{glob}, that is the best compromise between the width of the cascade-safe region, L_{cr}, and the transition speed towards the region where significant cascades appear, α. From the standpoint of the network operations, smaller E_{glob} appears to be safer, not only because it ensures lower critical loads, L_{cr}, but also because the cascading failure propagation is less affected by E_{glob} changes stemming from structural changes in the network.

As seen in Fig. 3.4, a network with fewer connections is able to incorporate a larger number of different link-node configurations. Therefore, a higher level of variability is introduced in the response to cascade spreading as E_{glob} decreases. Therefore, the statistical variability in the $\alpha = \alpha(E_{glob})$ and $L_{cr} = L_{cr}(E_{glob})$ relations presented in Figs. 3.8 and 3.9 increases for small E_{glob}. In Section 3.2, we realized that the variability introduced by the different link-node configurations affects only networks with small global connectivity efficiency, E_{glob}. To account for this behavior, the coefficient of variability is defined as $C_v = 1 - K/K_{max}$, where K_{max} denotes the maximum possible number of network connections or links. As shown in Fig. 3.10, for a completely connected system when the global efficiency $E_{glob} = 1$, $C_v = 0$.

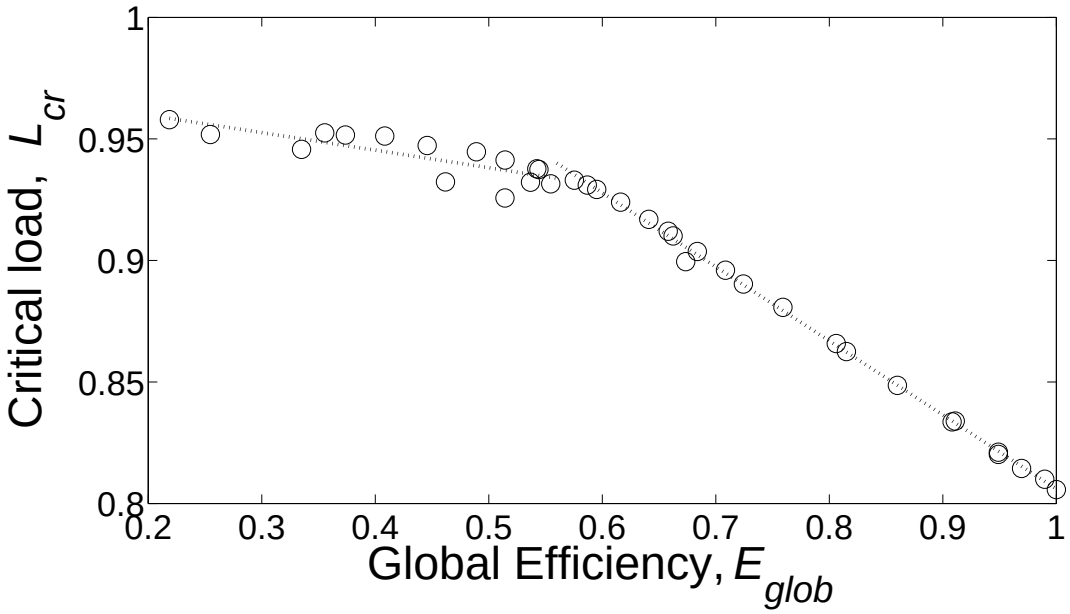

Figure 3.8: L_{cr} as function of E_{glob} for different network configurations K, but with $N = 50$. The bilinear relation was estimated through least square regression of the data for the thirty-seven networks in Tab. 3.1.

As E_{glob} and K decrease, the combinations connecting any two network nodes increase.

An intrinsic shortcoming of this deterministic representation of cascading failures stems from the multiple different link-node configurations which result in identical global connectivity efficiency, E_{glob} (see Fig. 3.4). The lack of an one-to-one correspondence between link-node configurations and E_{glob} spawns the lack of an one-to-one correspondence between E_{glob} and the model parameters L_{cr} and α, which turns out to be the reason for lack of accuracy in the cascading failure predictions.

Once the network connectivity is specified for a real system, the global efficiency is evaluated using Eq. 3.2 and thereafter used to determine α and L_{cr} from Eqs. 3.5 and 3.6. Thus, a model that is calibrated on a small set of thirty-seven network configurations for which $N_1 = N_2 = ... = N_n = N$, but $K_1 \neq K_2 \neq ... \neq K_n$, can be employed to predict the cascade spreading in any distributed system with N nodes (that are arbitrarily connected in any manner), through E_{glob}. Figure 3.11 compares the predictions of Eq. 3.4 for two networks

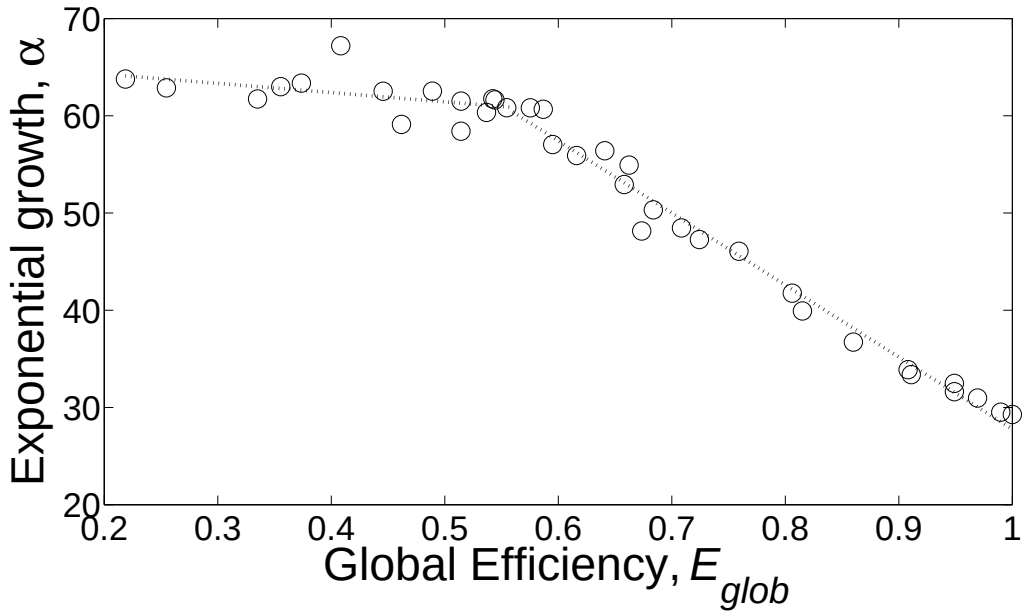

Figure 3.9: α as function of E_{glob} for different network configurations K, but with $N = 50$. The bilinear relation was estimated through least square regression of the data for the thirty-seven networks in Tab. 3.1.

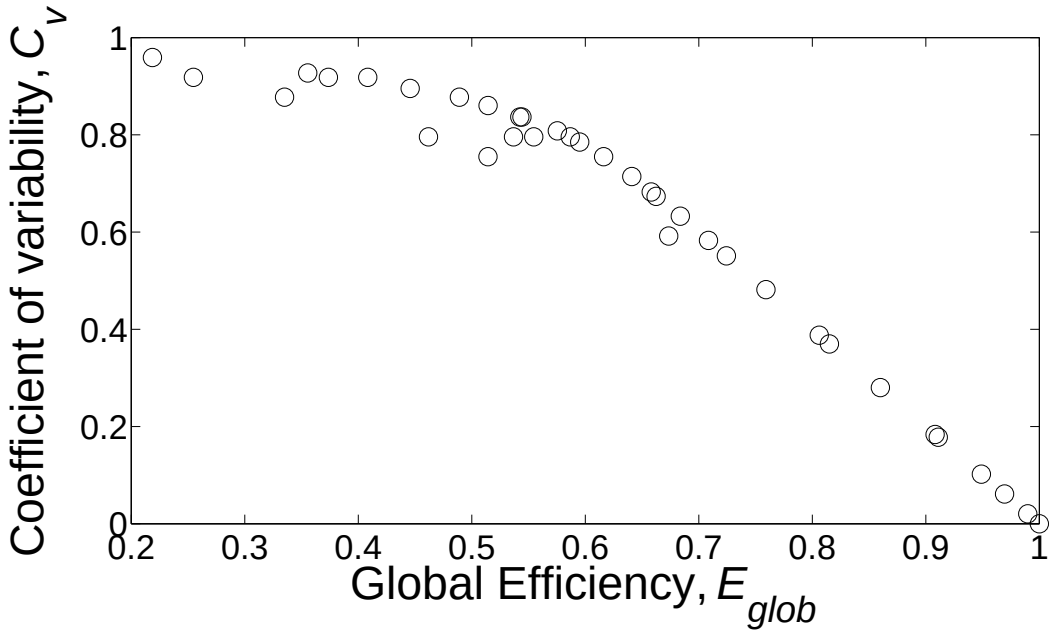

Figure 3.10: The variability in the possible connectivity patterns represented through the coefficient of variability $C_v = 1 - K/K_{max}$. If fewer links are allowed in a network, the combinations in which they can be placed increase, leading to poorer connectivity but failure at larger L_{cr}.

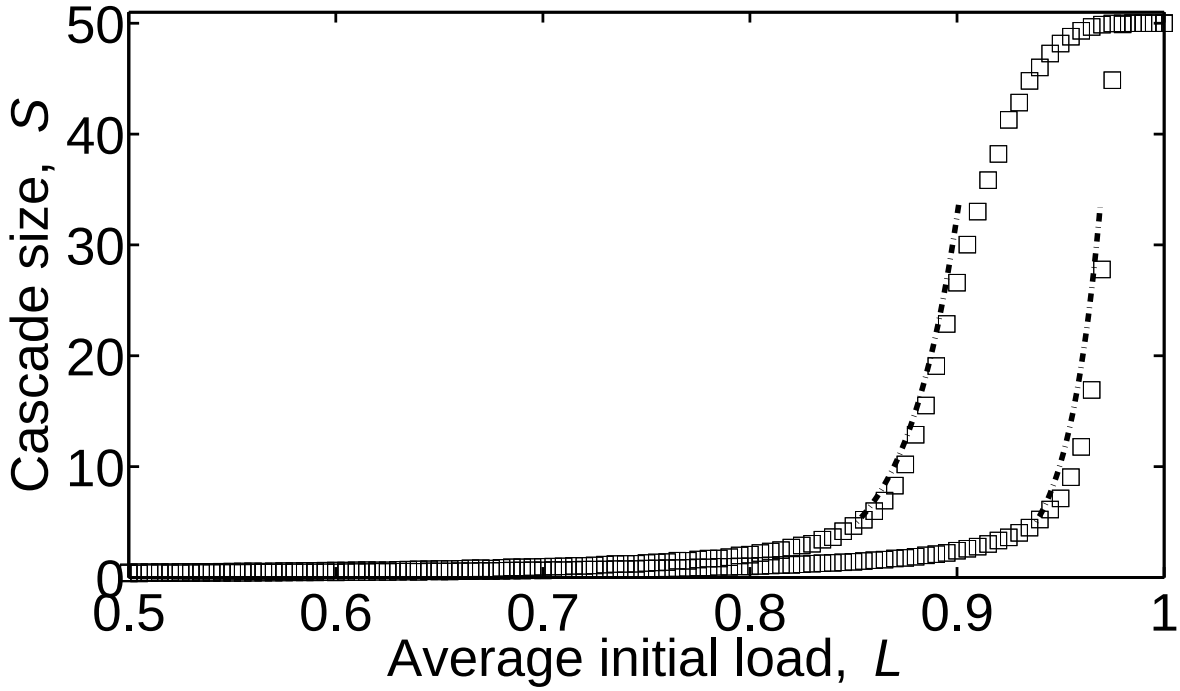

Figure 3.11: Two sets of cascade size predictions, using the deterministic relation of Eq. 3.4 (dashed line) for two different network connectivities ($E_{glob} = 0.85$, $K = 850$ and $E_{glob} = 0.50$, $K = 200$). The corresponding parameter values are $\alpha = 38.9$, $L_{cr} = 0.852$ and $\alpha = 61.5$, $L_{cr} = 0.938$. The results of the numerical simulations of cascading failure propagation (squares) are also provided to show the goodness of the two sets of cascade size predictions.

with (1) $E_{glob} = 0.85$, $K = 850$ and (2) $E_{glob} = 0.50$, $K = 200$. To test the accuracy of these estimates the results of more detailed numerical simulations are also provided. The predictions are in good agreement with the simulated cascading failures and it is clear that the reduced-order lumped parameter model provides reasonably accurate results. Its use can be advantageous in overcoming the potentially heavy computational burden of performing repeated numerical simulations for very large systems that have an identical number of nodes but different connectivity patterns. This is the case when networks are affected by contingencies that disrupt their connectivity. A prompt reevaluation of the effects of cascading failure propagations will be performed for the weakened network using this deterministic model.

In summary, if the overall network connectivity represented through the lumped param-

eter E_{glob} decreases for a system, it becomes less vulnerable to cascade spreading. While such a system can continue to work at higher loads before a cascade occurs, since L_{cr} has a relatively higher value, it is less resilient for $L > L_{cr}$ when it exhibits the sudden onset of cascading failure due to its large α value. Conversely, if E_{glob} increases, L_{cr} has a smaller value and the system becomes more vulnerable to cascade spreading due to its numerous links. Nevertheless, such a network is more resilient in resisting saturation when $L \to L_{cr}$ due to the relatively smaller value of α. The effects of the E_{glob} increase are represented by the leftward shift of L_{cr} for the corresponding networks in Fig. 3.11.

Several network system design considerations can be thus induced, e.g., a system that routinely approaches L_{cr} during its operation should have a larger E_{glob} value allowing a smoother transition to the cascade region and a reasonable reaction time to counteract the onset of significant cascading failures. On the other hand, if there is a need for L_{cr} to lie far beyond the operating range of the network, it could be made less vulnerable with fewer connections. Moreover, networks with structural constraints, e.g. the same number of links, K, can have different E_{glob} due to different link-node configurations (see Fig. 3.4). This degree of freedom in the wiring of the network can be used to elicit different responses towards cascading failure to comply with the design operating conditions.

The bilinear $\alpha = \alpha(E_{glob})$ and $L_{cr} = L_{cr}(E_{glob})$ relations presented in Figs. 3.8 and 3.9 and the nonlinear relation between the global connectivity efficiency, E_{glob}, and the network links, K, presented in Fig. 3.4 have opposite effects when one considers how changes in the number of connections, K, affect the propagations of cascading failures. In particular, regions where the cascading failure parameters, L_{cr} and α, are less sensitive to E_{glob} variations correspond to regions where E_{glob} is more sensitive to variations of the number of links K, i.e. for small E_{glob} and K, and vice versa. The combinations of these behaviors make the cascading failure parameters, L_{cr} and α, less sensitive with respect to variations in the number of links, K.

Chapter 4

Interdependent networks

In Chapter 3 we have discussed that understanding, modeling and assessing the normal functioning, as well as the possible faulty conditions of interconnected distributed systems, is essential to safely design these complex systems and to effectively provide their services. Distributed infrastructures have been modeled as graphs to unravel their structure and dynamics and to evaluate to what extent their structure has an impact on the dynamics (14).

However, it is evident that infrastructures do not exist in isolation from one another, and that the linking among service network infrastructures is necessary for their optimal and economical operation (43). As an example, the railway transportation system and the telecommunication networks both require power input from the electrical grid to perform their operations. On the other hand, efficient communication is required for the safe operation of the trains in the railway network and for the delivery of the proper amount of electrical power to the users of the power grid. In addition, interconnections among networks that provide identical services may be an expedient way to enhance their performances. Independently operating electrical power distribution systems or telecommunications networks that are located in neighboring regions can be interconnected so that a lack of power generation or communication capabilities in a region is compensated by an excess of generation or capabilities in other regions. Moreover, in this manner no additional power plants or routing stations are required.

The focus of the research on distributed infrastructures must then be shifted from single,

isolated systems to multiple, interconnected and mutually dependent systems. Such systems are called interdependent systems and the underlying network structures that describe them are called interdependent networks (43). Yet, these interdependencies introduce weaknesses in the systems due to the fact that failures may cascade from one system to other interdependent systems, possibly affecting their overall functioning if a proper design of interdependencies is not considered (44). Thus, it is important to assess the influences and limitations that interacting infrastructures impose on operating conditions of individual systems to avoid fault propagation by designing redundancies and alternative modes of operations, and detecting and recognizing threats (45). In particular, two complementary questions must be addressed in the design and operation of interdependent systems: (*i*) to what extent do cascading failures propagate along the interconnection among interdependent networks and (*ii*) how the most efficient interconnection among interdependent networks that minimizes the propagations of cascading failures is realized.

This chapter provides answers to these questions through a combination of structural analysis and simulation of cascading failures in interdependent networks. The interdependency connection efficiency, E_i, is introduced to evaluate the communication capabilities among the interdependency networks, i.e. how the structure of the interconnections affects the reachability of each individual component of the interdependent networks. The dynamics of the cascading failures is assessed through an extension of a numerical propagation model that was previously developed by the author (46). In this model, networks with arbitrary, random and diverse connectivity distributions can be generated, and the interdependencies among them can be varied to assess the extent of the propagations of cascading failures for different structural configurations.

Interdependencies among telecommunication systems, transportation systems and power distribution grids played a negative role in the small telecommunication blackout which took place in the suburbs of Rome, Italy in January 2004 (47). A flooding due to a break of a metallic pipe carrying cooling water of an air-conditioning plant in a major telecommunication service node led to a communication blackout. This, in turn, affected the communication/transmission operations in the area, hit the country's biggest printed news agency transmissions, stopped the check-in, ticketing, luggage acceptance and switching services at

Fiumicino International Airport, disturbed post offices and banking operations and caused problems to the communication network connecting the main Italian research institutions. Furthermore, the telecommunication blackout impacted the operation of the power distribution grid causing the disconnection of two control centers and resulting in the loss of control of a number of remote substations in the Rome area.

The role of dependencies among infrastructures (so called interdependencies) and the intrinsic difficulties arising in their modeling have been pointed out in previous studies (39; 48–75). A recent study appeared in Nature (76) highlighted the occurrence of a catastrophic cascade of failures in interdependent networks, taking as example the electrical blackout which affected Italy on 28 September 2003. During that event, the shutdown of power stations directly led to the failure of nodes in the Internet communication network, which in turn caused further breakdown of power stations.

Due to the intrinsic complexities related to interdependencies among infrastructures, their modeling is far from trivial for which abstractions can be helpful for a preliminary investigation or for deeper understanding of the dynamics of these networks. The proposed model of cascading failures herein for interdependent network systems aims at developing a simulation framework which abstracts the physical details of the services provided by the infrastructures while at the same time capturing their essential operating features. Such type of simulation models are appealing because of their simplicity and feasibility of use, which allows for the identification of factors that most contribute to the safe and efficient design and operation of interdependent infrastructures, and for assessing to what extent the presence of interdependencies affects the performance of the individual infrastructures. In particular, this scheme of analysis can be used for a first evaluation of the connectivity and interconnectivity patterns and of the operational margins of interdependent systems. This ensures that the services provided by infrastructures with cascade-safe conditions can prevent the propagation of failures over large areas.

Many models and computer simulation techniques exist for analyzing the behavior of individual infrastructures (43) (e.g., load flow and stability codes for electric power networks, connectivity and hydraulic analyses for pipeline systems, traffic management models for transportation networks), but modeling and simulation frameworks that allow the cou-

pling of multiple interdependent infrastructures are needed to address infrastructure protection, mitigation, response, and recovery issues. In developing these, it is important to know that simply linking existing infrastructure models together into a reduced model may fail to capture the emergent behavior arising in interdependent infrastructures (77).

4.1 A model for interdependent networks

Infrastructure interdependency stems from the functional and logical relations among individual components in different distributed systems.

The modeling carried out in this work considers two interdependent network systems, each created by a number N_i, $i = 1, 2$, of components (also called nodes or vertices) that are connected by K_i, $i = 1, 2$, links representing the physical and/or logical relations among them. If the two networks have the same number of links, i.e. $K_1 = K_2$, they are called symmetric networks. These are asymmetric networks if $K_1 \neq K_2$. The interdependencies are modeled as links connecting nodes of the two systems. These links are conceptually similar to those of the individual systems and are bidirectional with respect to the 'flow' between the two interdependent networks. The number of interdependency links among interdependent components in the two systems, M, and the fixed amount of load transferred over the interdependency links upon a component failure, I, are essential features characterizing the 'coupling level' between the two interdependent systems.

In Fig. 4.1, a particular realization of the systems considered in this study is shown. Two asymmetrical interdependent networks with $N_1 = N_2 = 24$ nodes, connected by $K_1 = 40$ and $K_2 = 60$ links (blue lines in Fig. 4.1), respectively, are presented. $M = 34$ interdependency links are drawn between the N_1+N_2 nodes as explained above (red lines in Fig. 4.1). All of the analyzed networks are constructed based on the abstract topological structure of the IEEE Reliability Test System - 96 (78), having $N = 24$ nodes and $K = 34$ links. Then, the numbers of links, K_1 and K_2, and the number of interdependency links, M, are varied to assess the corresponding effects on the connection efficiency and on the propagation of cascading failures in the interdependent networks. The numbers of nodes in the two networks are kept constant, i.e. $N_1 = N_2 = 24$. In our analysis, cascade onset and propagation over the bare topological

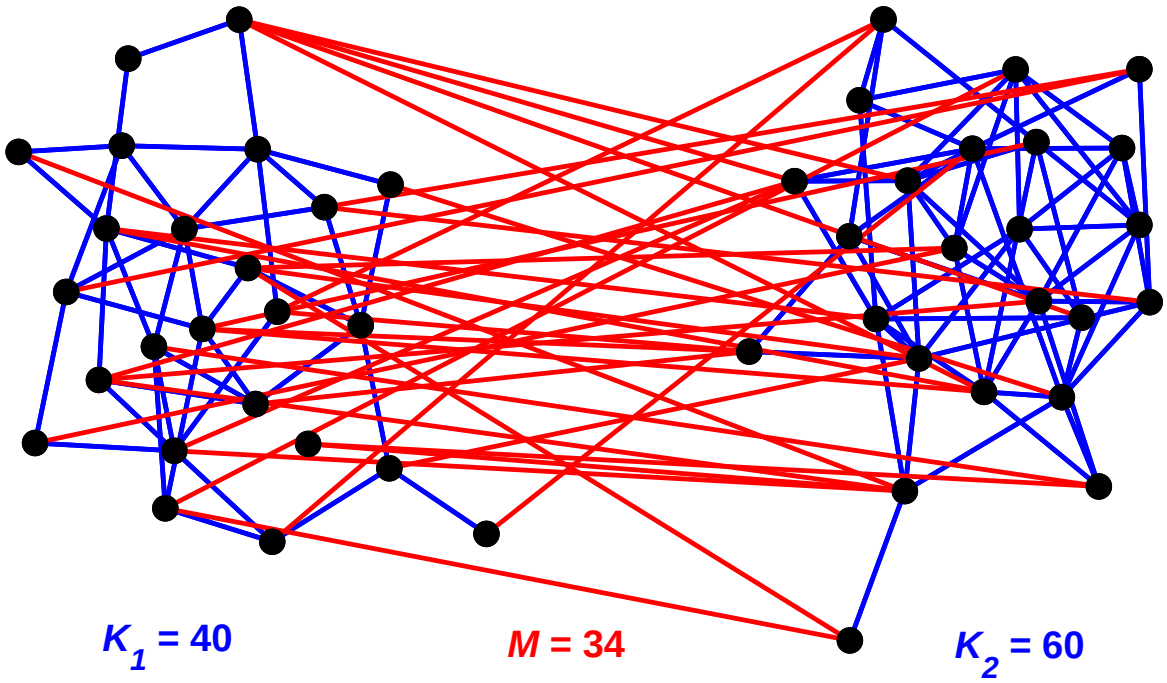

Figure 4.1: A particular realization of two asymmetric interdependent networks considered in this study. Each system has $N_1 = N_2 = 24$ nodes (black circles). System 1 on the left has $K_1 = 40$ links (blue lines) and system 2 on the right has $K_2 = 60$ links (blue lines). The two interdependent networks are interconnected by $M = 34$ interdependency links (red lines). The numbers of nodes $N_1 = N_2 = 24$ are constant throughout the study.

structure of the test systems is considered. No reference is made to the specific properties that characterize these infrastructures.

In the following analysis, our interest is on systems with varying 'interdependency level'. For a specific value of 'interdependency level', each node in system 1 could be interdependent with any other node in system 2, but the number of available interdependency links, M, between the two systems is fixed. Higher 'interdependency energies' correspond to larger numbers of interdependency links, M. To account for the dynamics of changing connections between the two networks under developing failure cascade processes, Monte Carlo simulations are performed in which the number of interdependency links, M, and the load transferred over the interdependency links, I, are kept constant but the interdependency

connections, M, among components are randomly rewired at each Monte Carlo trial. This approach allows us to evaluate the average system response to cascading failures at a given M, since it accounts for multiple interconnectivity patterns among the N_1 nodes in system 1 and the N_2 nodes in system 2. Therefore, this analysis provides an immediate indication of the average effects that the addition or the removal of n interdependency link have on the interdependency connection efficiency, E_i, and on the propagation of cascading failures in the interdependent networks.

Such average results are not only useful in that the description of the interdependency pattern is condensed into only one value, namely M, but they are also unavoidable due to the combinatorial complexity of the problem. As an example, consider the two interdependent networks in Fig. 4.1 with $N_1 = N_2 = 24$ nodes connected by $M = 34$ interdependency links. The maximum number of interdependency links, M_{max}, among among the N_1 nodes in system 1 and the N_2 nodes in system 2 is $M_{max} = N_1 \cdot N_2 = 24^2 = 576$. Thus, the number of the possible interconnectivity patterns that can be realized using the available $M = 34$ interdependency links is given by the number of combinations of the $M_{max} = 576$ links taken $M = 34$ at a time, i.e. $\binom{M_{max}}{M} = \binom{576}{34} \sim 9.0 \cdot 10^{54}$, whose magnitude excludes the possibility of their individual treatments. Communication systems, in which each node in system 1 can interact with any other node in system 2 but where there is a maximum amount of connecting energy between the two systems, could be an example of such energy-limited systems.

4.2 Evaluation of the global and interdependency connection efficiencies

4.2.1 The global connection efficiency, E_{glob}

The determination of the global connection efficiency within the two individual networks is carried out as described in Section 2.2. The global connection efficiency, E_{glob}, is defined as a measure of the reachability of the constituent parts of a network (18). To evaluate this quantity, the network of N nodes connected by K links is first represented as a graph

$G(N, K)$ that is defined by an $N \times N$ adjacency (connection) matrix $\{a_{ij}\}$ whose entries are 1 if there is an unbroken link between nodes i and j, or 0 otherwise.

The matrix of the shortest path lengths between nodes i and j, $\{d_{ij}\}$, is then evaluated using the Floyd algorithm (16), which performs the minimization with respect to all the possible paths, γ_{ij}, from every node i to any other node j. The matrix $\{d_{ij}\}$ contains the values

$$d_{ij} = \min_{\gamma_{ij}} \left(1 \Big/ \sum_{mn \in \gamma_{ij}} a_{mn} \right), \tag{4.1}$$

where the minimization is performed with respect to all paths γ_{ij} linking these nodes and the sum extends to all the edges formed by each of these paths. Thus, $1 \leq d_{ij} \leq \infty$, where the lower value denotes the existence of a direct link connecting i and j and the upper value applies when no paths connect the two nodes. The distance d_{ij} counts the numbers of links in the shortest path from node i to node j. Thus, it is called 'topological' distance since additional link features, such as their lengths or their reliabilities, are not considered.

The global efficiency $E_{glob}(G)$ is defined as being inversely proportional to the distance of the shortest path linking nodes i and j, i.e. (18),

$$E_{glob}(G) = \left(\sum_{i \neq j \in G} 1/d_{ij} \right) / \left(N(N-1) \right). \tag{4.2}$$

This topological lumped parameter characterizes the global connectivity of the network. Since the shortest path length between nodes i and j, $d_{ij} = 1$ when there is one direct link in the graph which connects nodes i and j, $E_{glob}(G)$ is equal to one in case of a perfectly connected network, in which a direct connection between any pair of nodes exists.

For the two interdependent networks of N_1 and N_2 nodes that are connected, respectively, by K_1 and K_2 links, there are two graphs $G_1(N_1, K_1)$ and $G_2(N_2, K_2)$, that are defined by two $N_1 \times N_1$ and $N_2 \times N_2$ adjacency (connection) matrices $\left\{a_{ij}^1\right\}$ and $\left\{a_{ij}^2\right\}$ whose entries are 1 if there is an unbroken link between nodes i and j, or 0 otherwise. The use of Eqs. 4.1 and 4.2 leads to the evaluation of the two global connection efficiencies, E_{glob}^1 and E_{glob}^2, characterizing system 1 and system 2, respectively.

As described in Section 3.2, it is not possible to establish a one-to-one correspondence between the global connectivity efficiency, E_{glob}, and the number of links, K, in a network. Different E_{glob} values may characterize networks having the same number of links K due to the variability in the possible connectivity patterns. Figure 4.2 presents the global connectivity efficiency values, E_{glob}, obtained placing K connections among the $N = 24$ network nodes. Each black dot is a realization of a connectivity pattern involving K connections and one thousand patterns are generated for each K. The red curve represents the average global connectivity efficiency, E_{glob}, for the considered numbers of connections, K. This relation is employed to establish an average one-to-one correspondence, $E_{glob} = f(K)$, between the global connectivity efficiency, E_{glob}, and the number of links, K. As a consequence of this one-to-one correspondence, all the possible connectivity patterns involving K links are represented by a network with K links forming an 'average' connectivity pattern. Moreover, symmetric networks, i.e. $K_1 = K_2$, have identical average global connectivity efficiency, E_{glob}. The maximum number of links that can be accommodated in the network of $N = 24$ nodes is $K_{max} = N(N-1)/2 = 276$. When $K = 0$ and $K = K_{max}$, only one connectivity pattern can be realized since $\binom{N(N-1)/2}{0} = 1$ and $\binom{N(N-1)/2}{N(N-1)/2} = 1$, respectively.

4.2.2 The interdependency connection efficiency, E_i

In the analysis of interdependent networks, a measure of the reachability of the constituent parts of the two networks must be identified. In particular, three different sets of links contribute to the connectivity between nodes in system 1 and nodes in system 2, namely, the interdependency links, M, between system 1 and system 2, but also the K_1 links in system 1 and the K_2 links in system 2. For example, a node in system 1 may not have a direct interdependency connection to any nodes in system 2 but, nonetheless, one of its neighboring nodes in system 1 may be connected to some interdependent nodes in system 2, thus establishing a path connecting nodes in different networks. Therefore, the K_1 and K_2 system links must be also accounted for in the evaluation of the interdependency connection efficiency, E_i.

To develop a definition of the interdependency connection efficiency, E_i, the two interdependent networks of N_1 and N_2 nodes that are respectively connected by K_1 and

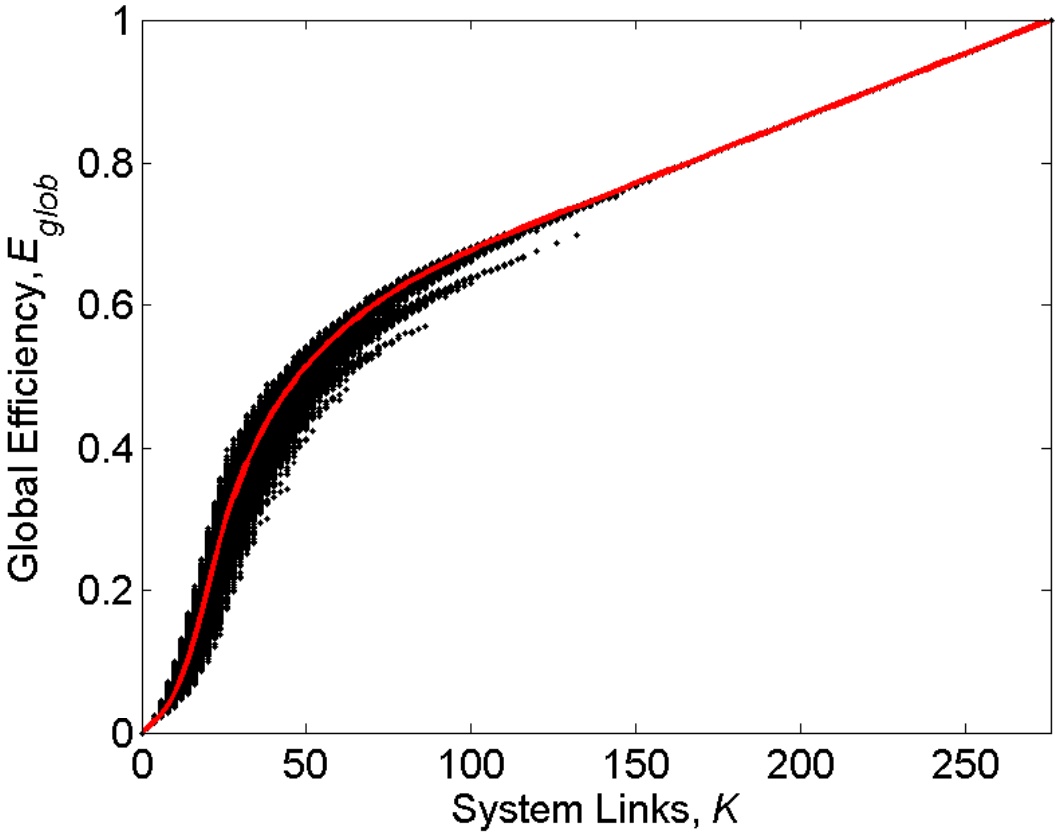

Figure 4.2: The global connectivity efficiency values, E_{glob}, obtained placing K connections among the $N = 24$ network nodes. Each black dot is a realization of a connectivity pattern involving K connections and one thousand patterns are generated for each K. The red curve represents the average global connectivity efficiency, E_{glob}, for the considered numbers of connections, K and describes the one-to-one correspondence, $E_{glob} = f(K)$. The maximum number of links that can be accommodated in the network of $N = 24$ nodes is $K_{max} = 276$.

K_2 system links and by M interdependency links are first represented as a unique graph $G\left(N_1+N_2, K_1+K_2, M\right)$ that is defined by a $(N_1+N_2)\times(N_1+N_2)$ interdependency matrix $\{m_{ij}\}$. The two $N_1\times N_1$ and $N_2\times N_2$ individual adjacency matrices for system 1 and 2, $\left\{a_{ij}^1\right\}$ and $\left\{a_{ij}^2\right\}$, describing the two isolated graphs, $G_1\left(N_1, K_1\right)$ and $G_2\left(N_2, K_2\right)$, are employed in the construction of the interdependency matrix $\{m_{ij}\}$ along with the interdependency connectivity pattern created by the M interdependencies.

The interdependency matrix $\{m_{ij}\}$ can be thought of as the combination of four matrices, namely,

1. The $N_1\times N_1$ north-west submatrix $\{m_{ij}\}$, with $i=1,..,N_1$ and $j=1,..,N_1$, which is identical to the matrix $\left\{a_{ij}^1\right\}$;

2. The $N_1\times N_2$ north-east submatrix $\{m_{ij}\}$, with $i=1,..,N_1$ and $j=N_1+1,..,N_1+N_2$, whose entries are 1 if there is an interdependency link between node i in system 1 and node $j-N_1$ in system 2, or 0 otherwise;

3. The $N_2\times N_1$ south-west submatrix $\{m_{ij}\}$, with $i=N_1+1,..,N_1+N_2$ and $j=1,..,N_1$, whose entries are 1 if there is an interdependency link between node $i-N_1$ in system 2 and node j in system 1, or 0 otherwise;

4. The $N_2\times N_2$ south-east submatrix $\{m_{ij}\}$, with $i=N_1+1,..,N_1+N_2$ and $j=N_1+1,..,N_1+N_2$, which is identical to the matrix $\left\{a_{ij}^2\right\}$.

In this study, these four submatrices are square matrices, since $N_1=N_2$, and the interdependency matrix $\{m_{ij}\}$ is a symmetric matrix, since all the system links, K_1 and K_2, and the interdependency links, M, are bidirectional. The interdependency matrix $\{m_{ij}\}$ has the following form,

$$\{m_{ij}\} = \left(\begin{array}{c|c} \left\{a_{ij}^{1}\right\},\ i = 1,..,N_1,\ j = 1,..,N_1 & \begin{array}{c}\textbf{1} \text{ if there is an interdependency} \\ \text{link between node } i \text{ in system 1} \\ \text{and node } j - N_1 \text{ in system 2,} \\ \text{or } \textbf{0} \text{ otherwise}\end{array} \\ \hline \begin{array}{c}\textbf{1} \text{ if there is an interdependency} \\ \text{link between node } i - N_1 \text{ in} \\ \text{system 1 and node } j \text{ in system 2,} \\ \text{or } \textbf{0} \text{ otherwise}\end{array} & \begin{array}{c}\left\{a_{i-N_1,j-N_1}^{2}\right\} \\ i = 1 + N_1,..,N_2 + N_1, \\ j = 1 + N_1,..,N_2 + N_1\end{array} \end{array} \right) \tag{4.3}$$

Analogous to individual networks, the matrix of the shortest path lengths, $\{d_{ij}\}$, between nodes i and j in the interdependency matrix, $\{m_{ij}\}$, is then evaluated using the Floyd algorithm (16), which performs the minimization with respect to all the possible paths, γ_{ij}, from every node i to any other node j. At the present stage the two interdependent network are treated as a combined overall network. The matrix $\{d_{ij}\}$ contains the values

$$d_{ij} = \min_{\gamma_{ij}} \left(1 \Big/ \sum_{mn \in \gamma_{ij}} a_{mn} \right), \tag{4.4}$$

where the minimization is performed with respect to all paths γ_{ij} linking the $N_1 + N_2$ nodes in the overall combined system and the sum extends to all the edges formed by each of these paths. Thus, $1 \leq d_{ij} \leq \infty$, where the lower value denotes the existence of a direct link connecting i and j and the upper value applies when no paths connect the two nodes. The distance d_{ij} counts the numbers of links in the shortest path from node i to node j. Thus, it is called the 'topological' distance since additional link features, such as their lengths or their reliabilities, are not considered.

The interdependency efficiency matrix, $\{\epsilon_{ij}\}$, is inversely proportional to the distance of the shortest path linking nodes i and j, i.e. $\epsilon_{ij} = 1/d_{ij}$. $0 \leq \epsilon_{ij} \leq 1$, where the lower value applies when no paths connect the two nodes and the upper value denotes the existence of a direct link connecting i and j. ϵ_{ij} is defined as the interdependency efficiency of the shortest path from node i to node j, since the interdependency links, M, are accounted for in its computation, as well as the $K_1 + K_2$ system links.

The interdependency efficiency E_i is defined in a way similar to Eq. 4.2 for single networks as the average of the interdependency efficiencies, $\{\epsilon_{ij}\}$, of the shortest paths from node i to node j,

$$E_i = \frac{\sum_{i \neq j} \epsilon_{ij}}{2N_1N_2 + [\frac{1}{2}(N_1(N_1-1) - 2K_1) + 2K_1] + [\frac{1}{2}(N_2(N_2-1) - 2K_2) + 2K_2]}. \quad (4.5)$$

This topological lumped parameter characterizes the interdependency connectivity of the network. In order to compare the interdependency efficiencies, E_i, in various interdependent networks, their values are normalized between 0 and 1, through the normalization constant in the denominator of Eq. 4.5. It amounts to the maximum value assumed by $\sum_{i \neq j} \epsilon_{ij}$ when $M = M_{max} = N_1 \cdot N_2$ interdependencies connect the two interdependent networks that have K_1 and K_2 links, respectively.

Each term in the denominator of Eq. 4.5 is the maximum values assumed by the sum of the elements of one of the four submatrices that form the interdependency efficiency matrix, $\{\epsilon_{ij}\}$. In particular, since every N_1 nodes in system 1 is directly connected to every N_2 node in system 2, $\{\epsilon_{ij}\} = 1$ for the $N_1 \times N_2$ north-east and for the $N_2 \times N_1$ south-west submatrices so that the term $N_1 \cdot N_2$ contributes twice to the normalization constant. A similar reasoning applies to the evaluation of the remaining two submatrices. When $M = M_{max}$, the N_1 nodes in system 1 are at most two links away through the interdependency connections with the N_2 nodes in system 2, the only exception being the K_1 links that establish direct connections among them. Since we are dealing with bidirectional links, a connection directed from node i to node j is considered also to be directed from node j to node i, and the contribution of the K_1 links appear twice in the $N_1 \times N_1$ north-west symmetric submatrix. Thus, the interdependency efficiency, $\epsilon_{ij} = \frac{1}{2}$ for the $(N_1(N_1 - 1) - 2K_1)$ shortest paths involving interdependent links, and $\epsilon_{ij} = 1$ for the $2K_1$ direct connections. The total number of directed shortest paths among N_1 nodes is $N_1(N_1 - 1)$, since self-connections from a node to itself are not allowed.

The maximum value of the sum of the elements in the south-east interdependency efficiency submatrix is evaluated analogously. When $M = M_{max}$, the N_2 nodes in system 2 are at most two links away through the interdependency connections with the N_1 nodes in system

1, the only exception being the K_2 links that establish direct connections among them. Since we are dealing with bidirectional links, a connection directed from node i to node j is also considered to be directed from node j to node i, and the contribution of the K_2 links appear twice in the $N_2 \times N_2$ south-east symmetric submatrix. Thus, the interdependency efficiency, $\epsilon_{ij} = \frac{1}{2}$ for the $(N_2(N_2-1)-2K_2)$ shortest paths involving interdependent links, and $\epsilon_{ij} = 1$ for the $2K_2$ direct connections. The total number of directed shortest paths among N_2 nodes is $N_2(N_2-1)$, since self-connections from a node to itself are not allowed.

It follows that $E_i = 1$ when the maximum number of interdependent links $M = M_{max} = N_1 \cdot N_2$ is present between the N_1 nodes of network 1 and the N_2 nodes of network 2, i.e. when every node in network 1 is interdependent on every node in network 2, and vice versa. On the contrary, Eq. 4.5 does not hold when $M = 0$, since the two networks are not interdependent. When there are no interdependencies between the two networks, i.e. $M = 0$, $E_i = 0$.

Figure 4.3 presents the interdependency efficiency values, E_i, obtained placing M interdependencies among two identical interdependent networks with $N_1 = N_2 = 24$ and $K_1 = K_2 = 34$, based on the abstract topological structure of the IEEE Reliability Test System - 96 (78). Each black dot is a realization of an interdependency pattern involving M interdependencies and of two connectivity patterns involving $K_1 = K_2$ links relative to network 1 and network 2, respectively. One thousand patterns are generated for each M. The red curve represents the average interdependency efficiency, E_i, for the considered numbers of interdependencies, M, and system links, $K_1 = K_2$. This relation is employed to establish an average one-to-one correspondence $E_i = f(M|K_1, K_2)$ between the interdependency efficiency, E_i, and the interdependency links, M, for specific numbers of system links, K_1 and K_2. As a consequence of this one-to-one correspondence, all the possible interdependency patterns involving M links are represented by M links forming an 'average' interdependency pattern. Moreover, the same number of interdependency links, M, generate identical average interdependency connectivity efficiencies, E_i. The maximum number of interdependency links that can be accommodated between the two networks of $N_1 = N_2 = 24$ nodes is $M_{max} = N_1 \cdot N_2 = 576$. When $M = 0$ and $M = K_{max}$, only one interdependency pattern can be realized, since $\binom{N_1 \cdot N_2}{0} = 1$ and $\binom{N_1 \cdot N_2}{N_1 \cdot N_2} = 1$, respectively.

The nonlinear relation between the interdependency efficiency, E_i, and the number of in-

terdependency links, M, presented in Fig. 4.3 allows us to draw some structural considerations about improving E_i. In particular, we can see that 80% of the maximum interdependency efficiency is attained with $M = 231$ interdependencies, which are 40% of the interdependencies required to build a fully interdependent network with $M = M_{max}$. This is due to the fast growth of E_i occurring at low M values. The fast initial growth is followed by a slower linear growth past $M = 231$ links. The residual 20% of the interdependency efficiency is attained with the addition of the remaining 60% of the maximum possible interdependencies. Therefore, we conclude that it is easier to increase the interdependency efficiency when fewer interdependencies are present, i.e. $M < 231$ for the case $N_1 = N_2 = 24$. By the same token, an improvement aiming at increasing the interdependencies M between two networks is much more effective in terms of E_i for systems with fewer interdependencies.

As seen through Eq. 4.3, the system links K_1 and K_2 contribute to the interdependency efficiency, E_i. In particular, large K_1 and K_2 values not only enhance the connection efficiencies, E^1_{glob} and E^2_{glob}, within the two networks, but also may lead to the formations of shorter paths among the N_1 in system 1 and the N_2 nodes in system 2 with an increase of the interdependency efficiency, E_i. This behavior is clarified in Fig. 4.4 where the average interdependency efficiency, E_i, is graphed with respect to the numbers of interdependencies M between two interdependent networks with $N_1 = N_2 = 24$ and $K_1 = K_2$, for increasing $K_1 = K_2 \in [34, 60, 90, 150, 270]$ values. As it can be seen, each M value is not univocally associated with a E_i value, but instead with increasing E_i values as $K_1 = K_2$ increase.

The adopted definition of the interdependency efficiency, E_i, allows a comparison not only of two interdependent networks with different M, but also two interdependent networks with different systems links K_1 and K_2. As an example, for two interdependent networks with $N_1 = N_2 = 24$, $K_1 = K_2 = 34$ and $M = 18$, $E_i = 0.4812$, while for two interdependent networks with $N_1 = N_2 = 24$, $K_1 = K_2 = 90$ and $M = 18$, $E_i = 0.6355$. Comparing curves at different $K_1 = K_2$ in Fig. 4.4, it appears that the system links K_1 and K_2 do not contribute to the interdependency efficiency, E_i, for large values of the interdependencies, M.

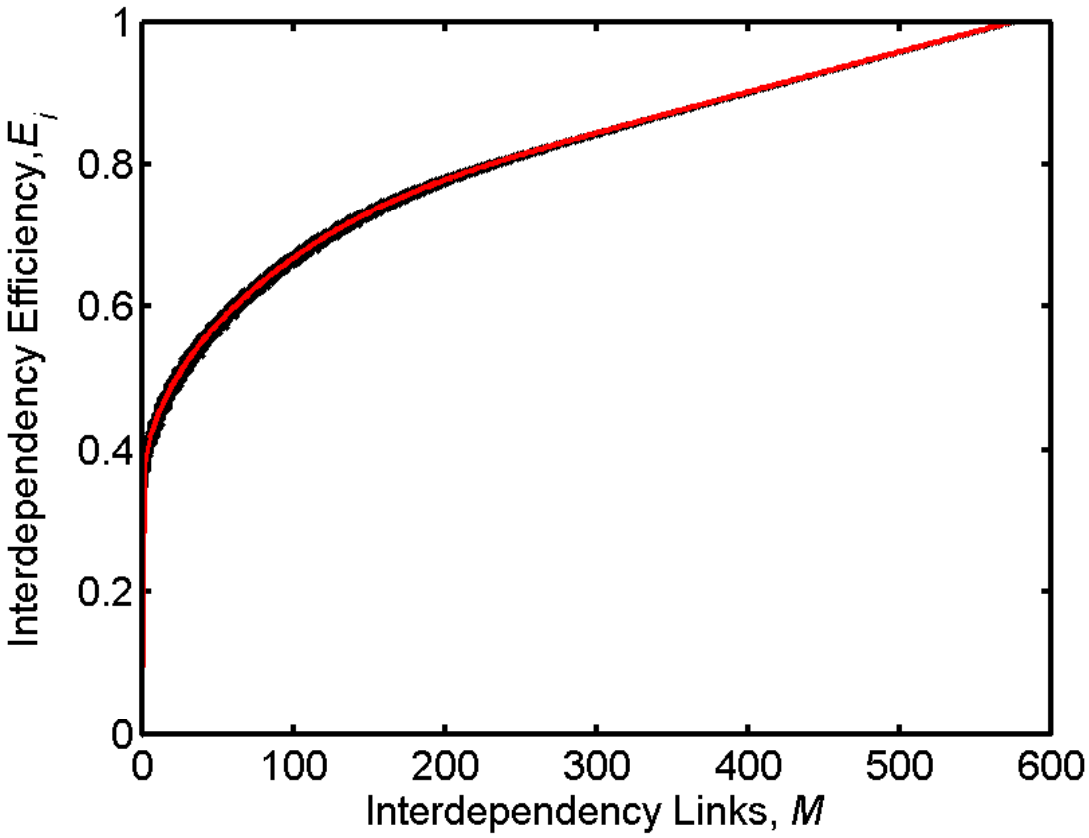

Figure 4.3: The interdependency efficiency values, E_i, obtained placing M interdependencies among two identical interdependent networks $N_1 = N_2 = 24$ and $K_1 = K_2 = 34$, based on the abstract topological structure of the IEEE Reliability Test System - 96 (78). Each black dot is a realization of an interdependency pattern involving M interdependencies and of two connectivity patterns involving $K_1 = K_2$ nodes, relative to network 1 and network 2, respectively. One thousand patterns are generated for each M. The red curve represents the average interdependency efficiency, E_i, for the considered numbers of interdependencies, M and describes the one-to-one correspondence, $E_i = f(M|K_1, K_2)$. The maximum number of interdependency links that can be accommodated between the two networks of $N_1 = N_2 = 24$ nodes is $M_{max} = N_1 \cdot N_2 = 576$.

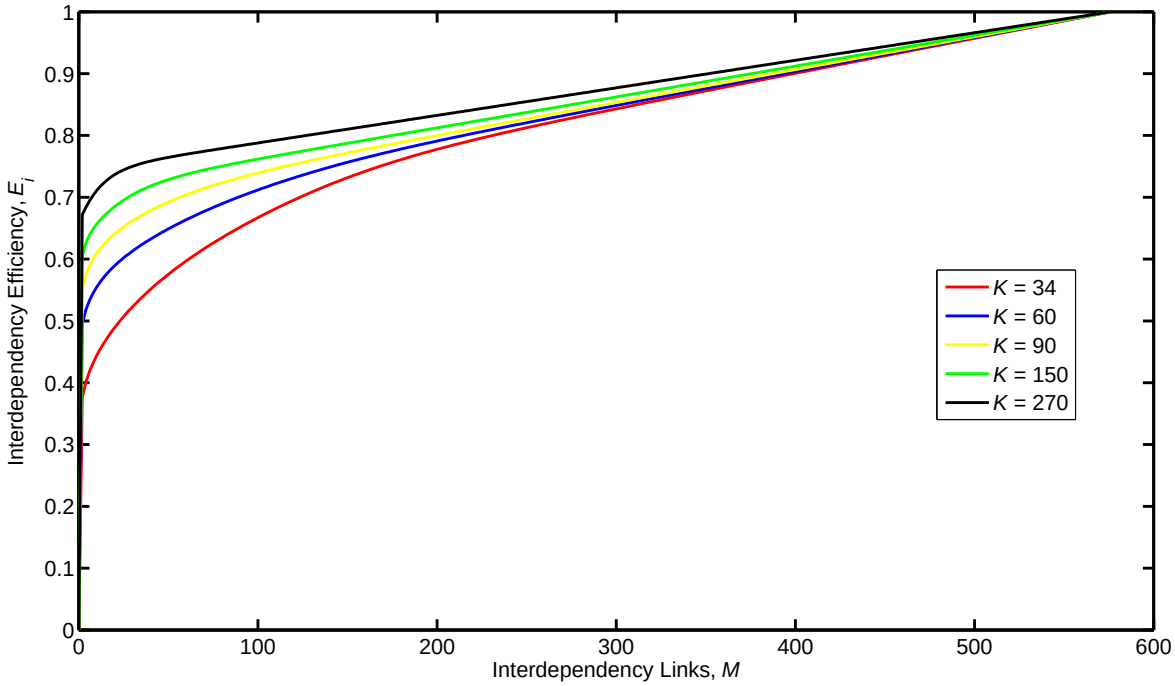

Figure 4.4: The average interdependency efficiency, E_i, vs. the numbers of interdependencies, M, between two interdependent networks with $N_1 = N_2 = 24$ and $K_1 = K_2$, for increasing $K_1 = K_2 \in [34, 60, 90, 150, 270]$ values. These curves represent averages of different system realizations with an interdependency pattern involving M interdependencies and two connectivity patterns involving $K_1 = K_2$ nodes, relative to network 1 and network 2, respectively. One thousand patterns are generated for each pairs of M and $K_1 = K_2$.

4.2.3 Two interdependent networks vs. one overall network

As stated above, infrastructure interdependency stems from the functional and logical relations among individual components in different distributed systems. Thus, in an analysis framework which accounts for the different physics of the service provided by the distributed infrastructures, the identification of the interacting interdependent networks and the distinction between interdependency links, M, and system links, K_1 and K_2, are clear-cut.

Conversely, the difference between two interacting infrastructures and one overall infrastructure may become fuzzy if interdependent infrastructures providing identical services, e.g. interacting regional power grids or telecommunication networks, are considered or if an analysis framework which abstracts the physics of the services provided by the interacting infrastructures is embraced. If this is the case, we must devise a methodology to discern when we should treat the systems as two interacting infrastructures or as one overall network, i.e. using the technique for single networks presented in Chapter 3.

To this end, the global connection efficiencies, E^1_{glob} and E^2_{glob}, and the interdependency efficiency, E_i, defined in Section 4.2.2, are employed to identify when the interdependent networks are so strongly coupled by the interdependency connections, M, that any reference to two separate networks loses its meaning.

As seen through Eq. 4.3, the system links K_1 and K_2 contribute both to the global connection efficiencies, E^1_{glob} and E^2_{glob}, and to the interdependency efficiency, E_i. Thus, the quantity $E_i - (E^1_{glob} + E^2_{glob})/2$ measures the average net contribution of the interdependency links, M, to the interdependency efficiency, E_i. For symmetric networks, i.e. $K_1 = K_2$, $E^1_{glob} = E^2_{glob} = E_{glob}$ due to the one-to-one correspondence, $E_{glob} = f(K)$, defined in Section 4.2.1, and the above relation reduces to $E_i - E_{glob}$. The 'strength' of the interdependencies and the 'strength' of the system connectivities are compared through the efficiency ratio, ρ, defined as,

$$\rho = (E_i - E_{glob})/E_{glob}. \tag{4.6}$$

We argue that when $\rho > 1$, the interdependencies are stronger than the individual system connectivities and the two networks must be treated as an unique overall network. Conversely,

when $\rho < 1$, the two networks can be actually treated within the formalism of interdependent networks. Using the one-to-one correspondences, $E_{glob} = f(K)$ and $E_i = f(M|K_1, K_2)$, found in Sections 4.2.1 and 4.2.2, respectively, we can identify how the inequality $\rho < 1$ translates into the inequality between the number of system links, $K_1 = K_2$, and the interdependencies, M. Figure 4.5 shows the efficiency ratio, ρ, with respect to the number of systems links, $K_1 = K_2$, for eight values of the interdependency connections, $M = 10, 15, 20, 34, 47, 60, 66, 75$. The intersection with the horizontal line, $\rho = 1$, identifies the minimum number of system links, $K_1 = K_2$, that must be in each of the two networks to ensure that they can be considered as two interdependent networks and not a unique overall network. As an example, when there are $M = 10$ interdependency links, there must be at least $K_1 = K_2 = 4$ system connections among the $N_1 = N_2 = 24$ nodes in the two networks. Alternatively, if we want to analyze two networks with $K_1 = K_2 = 25$ within the formalism of interdependent networks, we have to limit our analysis to no more than $M = 66$ interdependency links among their $N_1 = N_2 = 24$ nodes.

4.3 Propagation of failures in interdependent networks

4.3.1 Propagation algorithm

Following the same approach detailed in Section 2.4 for single, isolated networks, the model of cascading failures in interdependent network systems considers the local propagation of the overload (i) to first-neighbors (within the same network) and (ii) to the interdependent set (in the interdependent network) of the failed component. The proposed model differs from similar studies such as Ref. (24) since it does not rely on the assumption that the load on a component is proportional to the number of shortest paths running through it, which do not always reflect the actual routes of the flow in a network. On the contrary, it shares a similarity with the fiber bundle model in complex networks which has been applied to the blackout scenarios for cascading breakdown of power plants from overloading (40). Similar to the fiber bundle model, if the load in a node exceeds its capacity, that node is disconnected from the network and the demand is transferred locally to neighboring nodes through the edges of the network. Moreover, the underlying network is rigid while the vertices

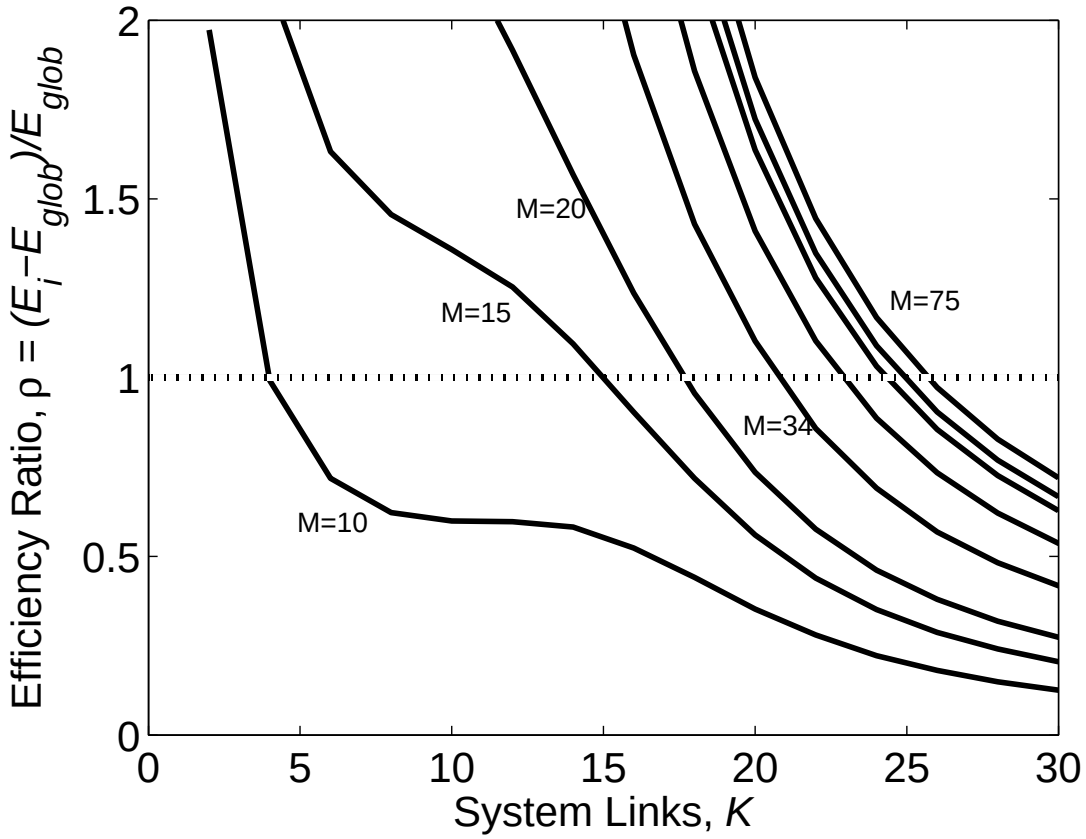

Figure 4.5: The efficiency ratio, ρ, vs. the number of systems links, $K_1 = K_2$, for eight values of the interdependency connections, $M = 10, 15, 20, 34, 47, 60, 66, 75$. The intersection with the horizontal line, $\rho = 1$, identifies the minimum number of system links, $K_1 = K_2$, that must be in each of the two networks to ensure that they can be considered two interdependent networks and not a unique overall network.

are damaged and, consequently, removed from the systems.

Consider two systems of N_1 and N_2 identical components ($N_1 = N_2 = N = 24$ in this study) connected by K_1 and K_2 links with random initial loads sampled uniformly between a minimum value L^i_{min} and a maximum value $L^i_{max},\ i = 1,\ 2$. The two systems are connected by M interdependency links.

For simplicity, but with no loss of generality, all components in the i-th system are assumed to have the same limit of operation L^i_{fail}, beyond which they fail ($L^1_{fail} = L^2_{fail} = L_{fail} = 1$ in this study, upon normalization of all loads relative to the failure load value). When a component fails, a fixed and positive amount of load is transferred locally to the first-neighbors of the failed node within the network structure it belongs to (a fixed and positive amount of load, $P^i,\ i = 1,\ 2$; $P^1 = P^2 = P = 0.07$ in this study) and to the interdependent components which the failed component is connected to in the other network system (a fixed and positive amount of load, $I = 0.07$), if any. If there is no working node in the neighborhood of a failed component or among the interdependent nodes connected to it, the cascade spreading along that path is stopped. The interdependency links between the two network systems are treated in the same way as the individual system links. They are bidirectional connections and upon the failure of a node in system 1 or 2, the fixed amount of load, I, is propagated locally to the nodes in the interdependent network system 2 or 1, if any interdependency is present for the failed node. This transfer accomplishes the coupling between the two systems.

To start the cascade, an initial disturbance imposes an additional load D_{j_i} on each component j_i of the two systems, $j_i = 1,\ 2, \ldots,\ N_i,\ i = 1,\ 2$ ($D_{j_1} = D_{j_2} = D = 0.02$ in this study). If the sum of the initial load L_{j_i} and the disturbance D_{j_i} of component j_i in system $i = 1,\ 2$ is larger than the component load threshold L^i_{fail}, component j_i fails. This failure occurrence leads to the redistribution of additional loads P^i on the neighboring nodes and I on the interdependent nodes, which may, in turn, get overloaded and thus fail in a cascade which follows the connection and interdependency patterns of the network systems. As the components become progressively more loaded, the cascade proceeds.

The algorithm for simulating the cascading failures proceeds in successive stages as follows:

0. At stage $m = 0$, a connectivity pattern involving $K_i,\ i = 1,\ 2$ system links is randomly generated among the $N_i,\ i = 1,\ 2$ nodes in network $i,\ i = 1,\ 2$. All $N_1 + N_2$ components

in systems 1 and 2 are working under independent uniformly random initial loads $L_1^i,\ L_2^i, \ldots,\ L_{N_i}^i \in [L_{min}^i, L_{max}^i]$, with $L_{max}^i < L_{fail}^i,\ i = 1,\ 2$.

1. M interdependency links between system 1 and system 2 are generated, connecting two randomly selected components; multiple interdependency links are allowed for each component.

2. An initial disturbance $D^i,\ i = 1,\ 2$, is added to the load of each component in the two systems.

3. Each component that has not failed is tested for failure: for $j_i = 1, \ldots,\ N_i$, if component j_i has not failed and its load $L_{j_i} > L_{fail}^i$ then component j_i in system i fails, $i = 1,\ 2$.

4. The components loads are incremented taking into account the network topology, i.e. the failed component neighborhood: for each failed node in system i, the load of its first-neighbors is incremented by an amount $P^i,\ i = 1,\ 2$. If the working neighborhood set of the failed node is empty, the associated failure propagation into the system comes to an end.

5. The components loads are incremented taking into account the interdependency pattern, i.e., the nodes interdependent to the failed component: for each failed node in system 1 or 2, the load of its interdependent nodes in system 2 or 1 is incremented by an amount I. If the interdependency set of the working components of the failed node is empty, the associated failure propagation to the interdependent system comes to an end.

6. The stage counter m is incremented by 1 and the algorithm is returned to step 3.

The damage caused by the cascade is quantified in terms of the number of network components which have failed in each network, i.e. the cascade size S^i, in system $i = 1,\ 2$, when the propagation comes to an end.

The values of the parameters which govern the outbreak and the propagation of the cascade, i.e. D, P and I, have to be gauged against the specific failure propagation to be represented. Larger D values result in many more component failures at the initial stage of

the cascade. Large P and I values facilitate the spreading of the failure cascade to a large number of components, since large overloads, P and I, will be transfered, respectively, to the neighborhood and to the interdependency set of a component upon its failure. In the following, the initial disturbance D is set to 2% of the failure load $L^{fail} = 1$. The load transfer over the system links, P, and the load transferred over the interdependency links, I, are both set equal to 7% of the failure load $L^{fail} = 1$. This choice of the cascade parameters results in few initial failures at the outbreak of the cascade while allowing its propagation to a large number of components during the next steps. This occurs in particular when the system operates at high loading conditions. Thus, the effects that the initial loading conditions have on the propagation of the cascading failure can be clearly identified.

Various initial system loading levels are evaluated varying the uniform sampling ranges $[L^i_{min}, L^i_{max}],\ i = 1,\ 2$, whose midpoints, L^i, are indicators of the average initial systems loading levels. The pair (L^i, S^i) is recorded for system $i = 1,\ 2$, at the end of every simulations. Large L^i values relate to operating conditions in which the systems are more stressed. For clarity, the range of variation of $L^i \in [0.5, 1]$ at 0.01 steps is obtained through the variation of L^i_{min} from 0 to 1 while $L^i_{max} = 1$.

4.3.2 Results of the propagation algorithm

The effects of the interdependencies between two symmetric systems, $K_1 = K_2 = 34$ and $N_1 = N_2 = 24$, are shown in Fig. 4.6 in terms of the average cascade size, $\bar{S^i}$, i.e., the number of failed components in the i-th system at the end of the cascade spread, versus the average initial load in the system, L^i, which represents the system operating level in system i, $i = 1,\ 2$. For each value of L^i, 1000 Monte Carlo simulations are repeated to obtain statistically significant results, with each simulation corresponding to a differently sampled pattern of the M interdependency links, different realizations of the same average loading condition, L^i, and different connectivity patterns generated by K_1 and K_2 system links.

The triangles in Fig. 4.6 represent the average cascade size, $\bar{S^i}$, in system $i = 1,\ 2$ as a function of the average initial load, $L^i = L$, for the isolated single systems $i = 1,\ 2$, i.e., when no interdependency is present. The overlapping squares and circles represent the same quantity $\bar{S^1} = \bar{S^2}$ for the symmetrical and identically operating systems 1 and 2, respectively,

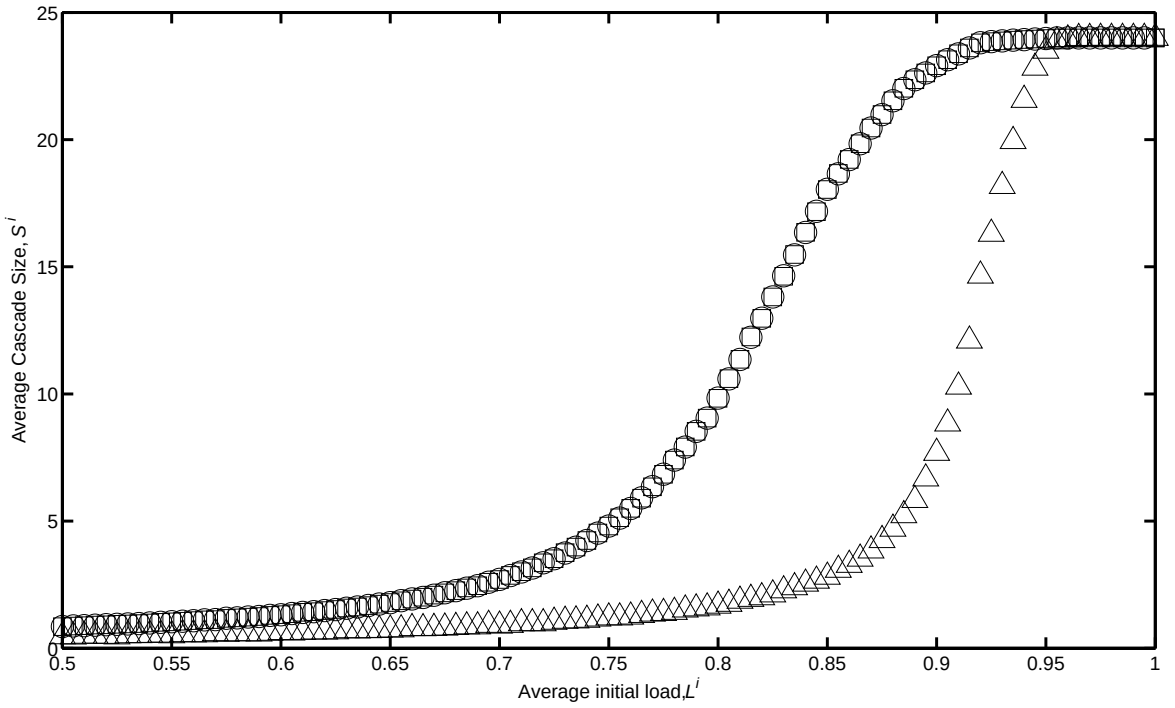

Figure 4.6: The average cascade size, $\bar{S}^i$, i.e., the number of failed components at the end of the cascade spread in the i-th system, vs. the average initial load in the system, $L^i = L$ for $i = 1,\ 2$, i.e. the midpoint of the uniform distribution where the random initial loads are sampled from. Triangles: isolated single system, $N = 24$ and $K = 34$. Squares and circles: symmetric interdependent systems 1 and 2, $N_1 = N_2 = 24$ and $K_1 = K_2 = 34$. Each plotted value is the average over 1000 Monte Carlo repetitions of the $M = 34$ interdependency links. In these simulations $L^i_{fail} = 1$, $D^i = 2\%$, $P^i = I = 7\%$, $K_i = M = 34$ for $i = 1,\ 2$.

when $M = 34$ interdependency links interconnect them. Similar to the corresponding diagram for isolated networks in Section 3.1, the results show how system loading can influence the risk of cascade spreading. At low levels, there is a trailing tail for small values of $\bar{S}^i$ in the distribution of the number of failed components. The longer this tail, the lower the susceptibility of a network to large cascading failures. There is a sharp change in the gradients of these tails at a critical loading L^i_{cr} that marks the transition between the non-cascading $L^i < L^i_{cr}$ and cascading $L^i > L^i_{cr}$ regions, for system i, $i = 1,\ 2$. This loading identifies the safe and critical failure-prone working conditions for the network i ($i = 1,\ 2$), since the likelihood of large cascading failures increases significantly when $L^i > L^i_{cr}$.

As expected, the interdependencies cause a shift to lower values of the loading threshold for which the cascading phenomenon appears (from approximately 0.9 for the individual isolated system to approximately 0.8 for the interdependent systems). Notice that as the average initial loading, $L^i = L$, on the system increases the systems are increasingly vulnerable to cascading failures. The transition from the non-cascading to the cascading region occurs with a smoother behavior for the two interdependent networks than for the individual isolated system, due to the fact that cascades start arising at lower average initial loading, $L^i = L$, in the interdependent networks which, thus, are less stressed and prone to their propagation. Nonetheless, the interdependencies between the two networks make access to the critical point easier, which means that the systems when coupled are more susceptible to large-scale failures and a failure in one system can cause a similar failure in the coupled system.

To quantitatively assess the effects of the interdependency in Fig. 4.6, a threshold representing the maximum allowable cascade size, S^i_{cr}, can be set which identifies the critical load, L^i_{cr}, beyond which the threshold is exceeded in system $i = 1,\ 2$. The maximum allowable cascade size, S^i_{cr}, is interpreted as the maximum number of components which can be lost in system i without affecting the global service provided by the infrastructure. This threshold can vary from system to system and is a distinguishing feature of the provided service. In the following, for simplicity but with no loss of generality $S^1_{cr} = S^2_{cr} = 15\%$ of the network nodes is assumed, which identifies $L^1_{cr} = L^2_{cr} = 0.8662$ for the individual systems in isolated conditions and $L^1_{cr} = L^2_{cr} = 0.7266$, for the two interdependent systems (Fig. 4.6).

Due to the interdependencies, the two networks have become more prone to the outbreak

and the propagation of cascading failures than the corresponding isolated network with the same number of nodes and links, since the region where cascade of large size appear has increased from $L = [0.8662,\ 1]$ for the system in isolated conditions to $L^i = [0.7266,\ 1]$, for the two interdependent symmetric systems. From Fig. 4.6, it is also observed that the transition from cascade-safe to cascade regime is smoother for interdependent networks, allowing more time for them to react against the cascading failure onset.

4.4 Effects of the connectivity structure on the operation of the interdependent networks

In this Section, the first of the two fundamental issues in the design and operation of interdependent networks is addressed, namely, to what extent cascading failures propagate along the system links, K_1 and K_2, and along the interdependency connections, M, among interdependent networks. In particular, we assess how the structural configurations of the system links and of the interdependency links limit the operations of the two interdependent networks in terms of the critical loads, L^1_{cr} and L^2_{cr}, defined in Section 4.3.2 for system 1 and system 2. Interdependent networks with $N_1 = N_2 = 24$ nodes are considered in this analysis.

Diagrams for interdependent networks similar to the one in Fig. 4.6 are traced for varying K_1 and K_2 and M, which form varying connectivity and interconnectivity patterns, respectively. Average values of the critical loads, L^1_{cr} and L^2_{cr}, are evaluated from these diagrams, providing indications about the amplitude of the cascade-safe regions, i.e. $L^1 = [0.5,\ L^1_{cr}]$ and $L^2 = [0.5,\ L^2_{cr}]$, and on the vulnerability of the interdependent networks towards cascading failures.

Symmetric interdependent networks, i.e. $K_1 = K_2$, are considered in Section 4.4.1 and asymmetric interdependent networks, i.e. $K_1 \neq K_2$, are considered in Section 4.4.2. The results for two asymmetric interdependent networks, e.g. $K_1 = k_1$ and $K_2 = k_2$, are bounded by the results for the two sets of corresponding symmetric interdependent networks, i.e. with $K_1 = K_2 = k_1$ and $K_1 = K_2 = k_2$, respectively. Thus, the analysis of symmetric interdependent networks encompasses the analysis of asymmetric interdependent networks.

4.4.1 Symmetric interdependent networks

The limitations that increasing interdependency links, M, impose on the operations of symmetric interdependent networks are assessed for different connectivity patterns involving $K_1 = K_2$ system links. Figure 4.7 presents the critical loads, L^1_{cr} (circles) and L^2_{cr} (squares) vs. the interdependency links, M, for 6 sets of symmetric interdependent networks having $K_1 = K_2 = K \in [34, 60, 90, 120, 150, 180]$ system links. The critical loads L^1_{cr} and L^2_{cr} almost completely overlap since the two interdependent networks are symmetric and the cascading failures similarly arise and propagate in them. The small discrepancies in L^1_{cr} and L^2_{cr} for the same M and K are due to the different random connectivity and interconnectivity patterns, with K system links and M interdependency links, respectively, that are realized for each simulation.

The diagram in Fig. 4.7 conveys information about the effects that particular system configurations, (K_1, K_2, M), have on the propagation of cascading failure in term of the amplitude of the cascade-safe regions, $L^1 = [0.5,\ L^1_{cr}]$ and $L^2 = [0.5,\ L^2_{cr}]$. As an example, if $K_1 = K_2 = 90$ and $M = 18$, the cascade-safe regions are, $L^1 = [0.5,\ 0.667]$ and $L^2 = [0.5,\ 0.664]$. Thus, the two networks must be operated with these load extremes to avoid the propagation of large cascading failures. Figure 4.7 can be used to find system configurations, (K_1, K_2, M), that guarantee a minimum amplitude of the cascade-safe region. As an example, if we want the cascade-safe regions to be larger than, $L^1 = [0.5,\ 0.7]$ and $L^2 = [0.5,\ 0.7]$, in symmetric interdependent networks with $M = 26$, then the maximum number of allowed system links is $K_1 = K_2 = 60$.

For different system links, K, the critical loads, L^1_{cr} and L^2_{cr}, approach the line $L^i_{cr} = 0.5$ with the same trend. When $L^i_{cr} = 0.5$, the amplitude of the cascade-safe region for network i is zero. This means that cascades having size larger than the critical size $S^1_{cr} = S^2_{cr} = 15\%$ of the network nodes will propagate in the two interdependent networks irrespective of the average initial load in the systems, $L^i = L$ for $i = 1,\ 2$.

From Fig. 4.7, we also notice that as the system links, $K_1 = K_2$, increase, fewer interdependency links, M, can be allowed among the two networks so that the amplitude of the cascade-safe region is unchanged. For example, when $K = 34$ and $M = 43$, the cascade-safe

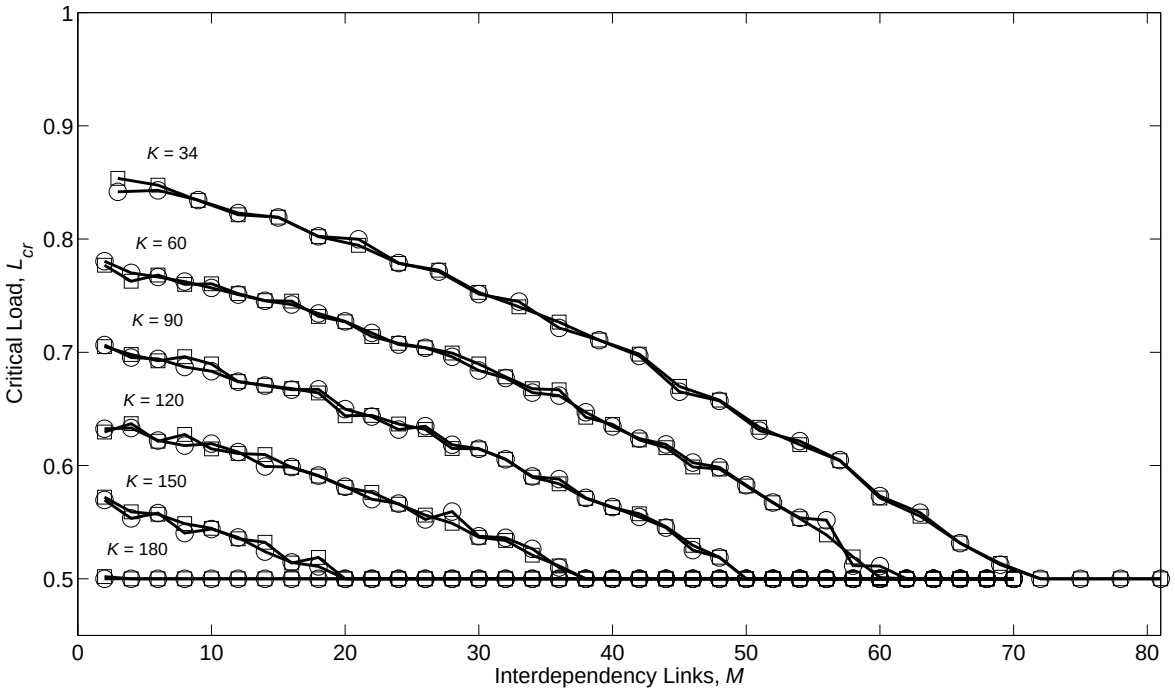

Figure 4.7: The critical loads, L_{cr}^1 (circles) and L_{cr}^2 (squares), vs. the interdependency links, M, for 6 sets of symmetric interdependent networks having $K_1 = K_2 = K \in [34, 60, 90, 120, 150, 180]$ system links. $N_1 = N_2 = 24$.

region for network 1 is $L^1 = [0.5,\ 0.7]$, while the same cascade-safe region is granted by no more than $M = 3$ interdependency links if $K = 90$. By the same token, symmetric interdependent networks with $K = 180$ system links have no cascade-safe region irrespective of the number of interdependencies, M. Furthermore, even for relatively few system links, $K = 34$ (less that 13% of the maximum number of system links, $K_{max} = 276$), the cascade-safe region disappear beyond $M = 73$ interdependency links that are less that 13% of the maximum number of interdependency links, $M_{max} = 576$, among $N_1 = 24$ and $N_2 = 24$ nodes.

Resorting to the one-to-one correspondence between E_i and M, $E_i = f(M|K_1, K_2)$, defined in Section 4.2.2, we can assess the limitations that the increasing interdependency efficiency, E_i, imposes on the operations of symmetric interdependent networks. Figure 4.8 presents the critical loads, L_{cr}^1 (circles) and L_{cr}^2 (squares), vs. the interdependency efficiency, E_i, for 6 sets of symmetric interdependent networks having $K_1 = K_2 = K =$

$34, 60, 90, 120, 150$ and 180 system links. As in Fig. 4.7, the critical loads L_{cr}^1 and L_{cr}^2 almost completely overlap since the two interdependent networks are symmetric and the cascading failures similarly arise and propagate in them. The small discrepancies in L_{cr}^1 and L_{cr}^2 for the same E_i and K are due to the different random connectivity and interconnectivity patterns, with K system links and E_i interdependency efficiency, respectively, that are realized for each simulations.

All curves for different K values in Fig. 4.8 show two trends, namely, a region at smaller E_i, for which the amplitude of the cascade-safe region is less sensitive to E_i variations, followed by a region at larger E_i, in which the the amplitude of the cascade-safe region varies sharply due to small E_i changes. This behavior must be taken into account during the operations of the interdependent networks since even a small variation in the interdependency efficiency, E_i, may lead to severe consequences in the propagation of cascading failures, such as the sudden reduction of the cascade-safe region.

From Fig. 4.7, we notice that the L_{cr}^i vs. M diagrams intersect the horizontal line $L_{cr}^i = 0.5$ (at which the amplitude of the cascade-safe region for network i is zero) at decreasing M values as the system links, K, increase. On the contrary, from Fig. 4.4, it appears that, when the system links, K, increase the interdependency efficiency, E_i, increases for constant interdependency links, M. Due to the combined effect of these opposing trends, all the diagrams in Fig. 4.8 intersect the horizontal line $L_{cr}^i = 0.5$, within a narrow range of interdependency efficiency, $0.62 < E_i < 0.70$, for a broad range of system links, i.e. at least $34 \leq K \leq 180$. Therefore, when symmetric interdependent networks are operated, we expect the disappearance of the cascade-safe region if the interdependency efficiency falls within or beyond the range identified above.

A complementary assessment with respect to the variation of the system links, $K_1 = K_2 = K$, is also performed in symmetric interdependent network with $N_1 = N_2 = 24$. In particular, the limitations that increasing system links, $K_1 = K_2 = K$, impose on the operations of symmetric interdependent networks are evaluated for different interdependency patterns involving M interdependency links. Figure 4.9 presents the critical loads, L_{cr}^1 (circles) and L_{cr}^2 (squares), vs. the system links, $K_1 = K_2 = K$, for 7 sets of symmetric interdependent networks having $M = 1, 10, 20, 34, 47, 60$ and 66 interdependency links. The critical loads

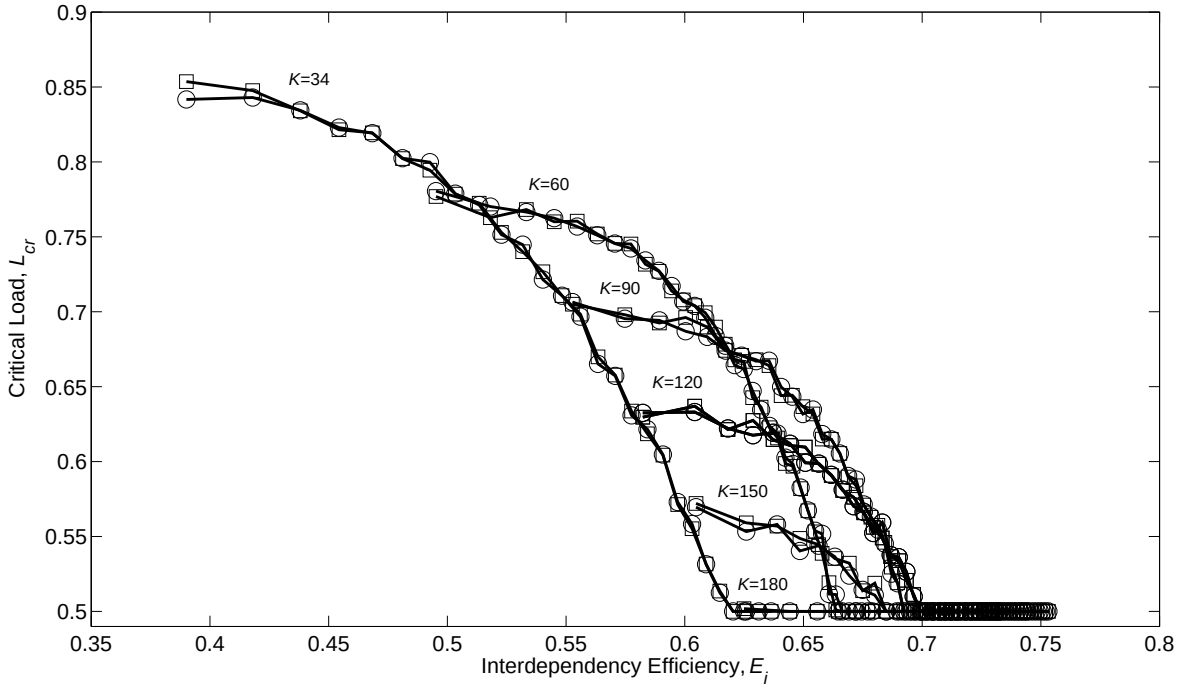

Figure 4.8: The critical loads, L_{cr}^1 (circles) and L_{cr}^2 (squares), vs. the interdependency efficiency, E_i, for 6 sets of symmetric interdependent networks having $K_1 = K_2 = K = 34, 60, 90, 120, 150$ and 180 system links. $N_1 = N_2 = 24$.

L_{cr}^1 and L_{cr}^2 almost completely overlap since the two interdependent networks are symmetric and the cascading failures similarly arise and propagate in them. The small discrepancies in L_{cr}^1 and L_{cr}^2 for the same K and M are due to the different random connectivity and interconnectivity patterns, with K system links and M interdependency links, respectively, that are realized for each simulations.

As seen in Section 4.2.3, for a specific number of interdependencies, M, there must be a minimum number of system links, $K_1 = K_2 = K$, in each of the two networks to ensure that they can be treated as two interdependent networks and not as a unique overall network. Hence, in Fig. 4.9 we see that as M increases, the minimum number of system links, $K_1 = K_2 = K$, in the interdependent networks increases consequently.

The diagram in Fig. 4.9 conveys information about the effects that particular system configurations, (K_1, K_2, M), have on the propagation of cascading failure in term of the amplitude of the cascade-safe regions, $L^1 = [0.5,\ L_{cr}^1]$ and $L^2 = [0.5,\ L_{cr}^2]$. As an example, if $K_1 = K_2 = 45$ and $M = 34$, the cascade-safe regions are, $L^1 = [0.5,\ 0.705]$ and $L^2 = [0.5,\ 0.703]$. Thus, the two networks must be operated with these load extremes to avoid the propagation of large cascading failures. Figure 4.9 can be used to find system configurations, (K_1, K_2, M), that guarantee a minimum amplitude of the cascade-safe region. As an example, if we want the cascade-safe regions to be larger than, $L^1 = [0.5,\ 0.7]$ and $L^2 = [0.5,\ 0.7]$, in symmetric interdependent networks with $K = 70$, then the maximum number of allowed interdependency links is $M = 20$.

For varying interdependency links, M, the critical loads, L_{cr}^1 and L_{cr}^2, approach the line $L_{cr}^i = 0.5$ with the same linear trend. When $L_{cr}^i = 0.5$, the amplitude of the cascade-safe region for network i is zero. Therefore, for that (K^*, M^*) combination and for those having $K > K^*$ and $M > M^*$, cascades having size larger than the critical size $S_{cr}^1 = S_{cr}^2 = 15\%$ of the network nodes will propagate in the two interdependent networks irrespective of the average initial load in the systems, $L^i = L$ for $i = 1,\ 2$.

From Fig. 4.9, we also notice that as the interdependency links, M, increase, fewer system links, K, can be allowed in the two networks so that the amplitude of the cascade-safe region is unchanged. For example, when $M = 20$ and $K = 94$, the cascade-safe region for network 1 is $L^1 = [0.5,\ 0.65]$, while the same cascade-safe region is granted by no more than $K = 38$ system

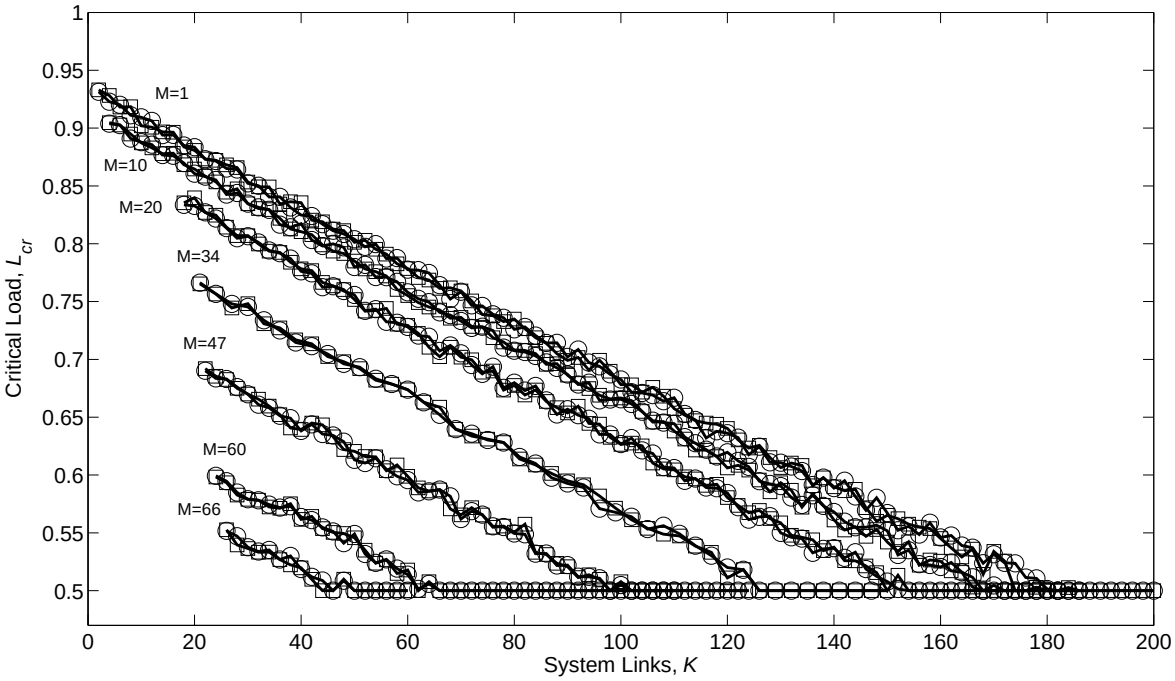

Figure 4.9: The critical loads, L_{cr}^1 (circles) and L_{cr}^2 (squares), vs. the system links, $K_1 = K_2 = K$, for 7 sets of symmetric interdependent networks having $M = 1, 10, 20, 34, 47, 60$ and 66 interdependency links. $N_1 = N_2 = 24$. As M increases, the minimum number of system links, $K_1 = K_2 = K$, in the two interdependent networks increases consequently, ensuring that the systems can be treated within the framework of interdependent network analysis (see Section 4.2.3).

links if $M = 47$. By the same token, symmetric interdependent networks with approximately $M = 70$ interdependency links have no cascade-safe region irrespective of the number of system links, K.

Resorting to the one-to-one correspondence between E_{glob} and K, $E_{glob} = f(K)$, defined in Section 4.2.1, we can assess the limitations that the increasing connection efficiencies, $E_{glob}^1 = E_{glob}^2 = E_{glob}$, imposes on the operations of symmetric interdependent networks. Figure 4.10 presents the critical loads, L_{cr}^1 (circles) and L_{cr}^2 (squares), vs. the global efficiency, E_{glob}, for 7 sets of symmetric interdependent networks having $M = 1, 10, 20, 34, 47, 60$ and 66 interdependency links. As in Fig. 4.9, the critical loads L_{cr}^1 and L_{cr}^2 almost completely overlap

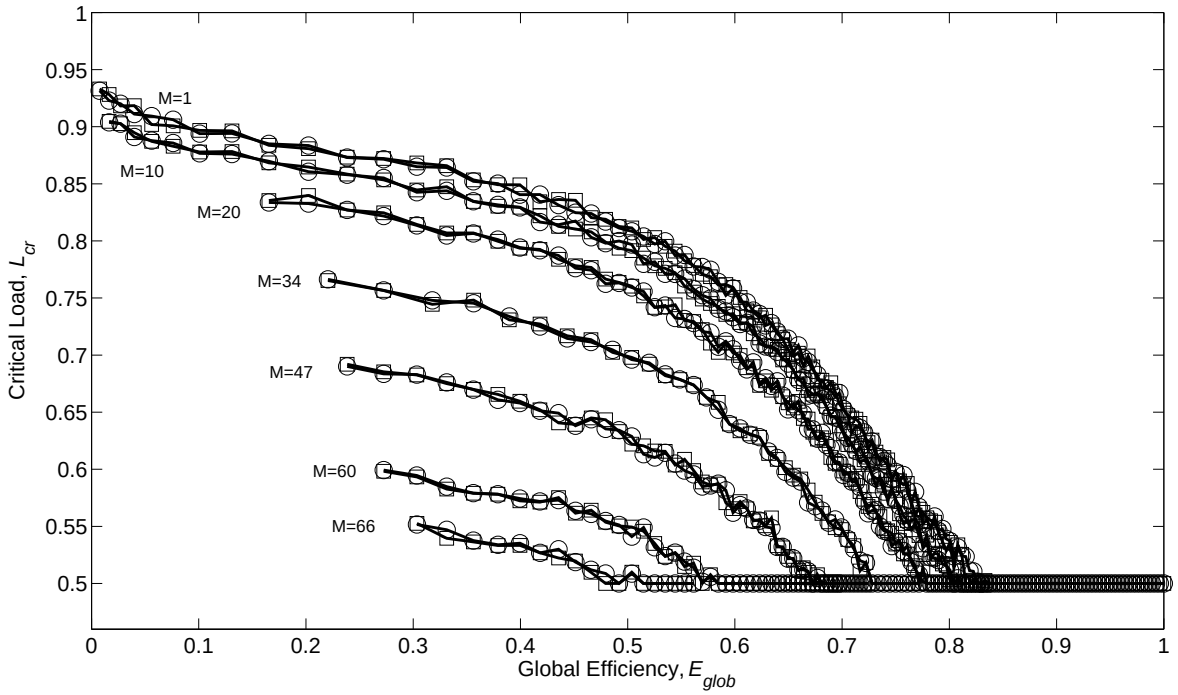

Figure 4.10: The critical loads, L_{cr}^1 (circles) and L_{cr}^2 (squares), vs. the global efficiency, E_{glob}, for 7 sets of symmetric interdependent networks having $M = 1, 10, 20, 34, 47, 60$ and 66 interdependency links. $N_1 = N_2 = 24$.

since the two interdependent networks are symmetric and the cascading failures similarly arise and propagate in them. The small discrepancies in L_{cr}^1 and L_{cr}^2 for the same E_{glob} and M are due to the different random connectivity and interconnectivity patterns, with M system links and E_{glob} global efficiency, respectively, that are realized for each simulations.

All curves at different M in Fig. 4.10 show two trends, namely, a region at smaller E_{glob}, for which the amplitude of the cascade-safe region is less sensitive to E_{glob} variations, followed by a region at larger E_{glob}, in which the the amplitude of the cascade-safe region varies sharply due to small E_{glob} changes. This behavior must be taken into account during the operations of the interdependent networks since even a small variation in the global efficiency, E_{glob}, may lead to severe consequences in the propagation of cascading failures, such as the sudden reduction of the cascade-safe region.

4.4.2 Asymmetric interdependent networks

When two networks are coupled, there are in principle no limitations on the number of the system links, K_1 and K_2, they may contain. Therefore, the coupling of asymmetric interdependent networks, i.e. $K_1 \neq K_2$, and the cascading failure propagation in them must be also analyzed. In particular, the limitations that the structure of asymmetric interdependency networks, i.e. particular (K_1, K_2, M) combinations, impose on their operations have been assessed.

Figure 4.11 presents the critical loads, L_{cr}^1 (black circles) and L_{cr}^2 (black squares), vs. the interdependency links, M, for the two asymmetric interdependent networks having $K_1 = 60$ and $K_2 = 90$ system links, shown in Fig. 4.1. Since the two networks have different numbers of system links, cascading failures do not similarly propagate in them, therefore the critical loads L_{cr}^1 and L_{cr}^2 do not overlap. The results for two sets of symmetric interdependent networks with $K_1 = K_2 = 60$ (red markers and line) and $K_1 = K_2 = 90$ (cyan markers and line), respectively, are also shown for comparison.

The results for asymmetric networks are bounded by those for symmetric networks. In particular, the results for the corresponding symmetric networks with the smaller number of links, i.e. $K_1 = K_2 = 60$, form the upper bound for the asymmetric networks case, while the results for the corresponding symmetric networks with the larger number of links, i.e. $K_1 = K_2 = 90$, form the lower bound. This behavior is not surprising. As seen in Fig.4.7, symmetric interdependent networks with many system links, $K_1 = K_2$, are more prone to cascading failures than those with fewer system links, for the same M values. In the asymmetric configuration of Fig. 4.11, the network with $K_1 = 60$ is coupled to a network with $K_2 = 90$ that is more prone to the propagation of cascading failures. On the other hand, the network with $K_2 = 90$ is coupled to a network with $K_1 = 60$ that is less prone to the propagation of cascading failures. Therefore, the results for the asymmetric configurations, follow in between the results for the corresponding symmetric configurations. As a result, the cascade-safe regions in network 2 ($K_2 > K_1$) are broader in the asymmetric configuration than they are in the symmetric configuration. Conversely, the cascade-safe regions in network 1 ($K_1 < K_2$) are narrower in the asymmetric configuration than they are in the symmetric

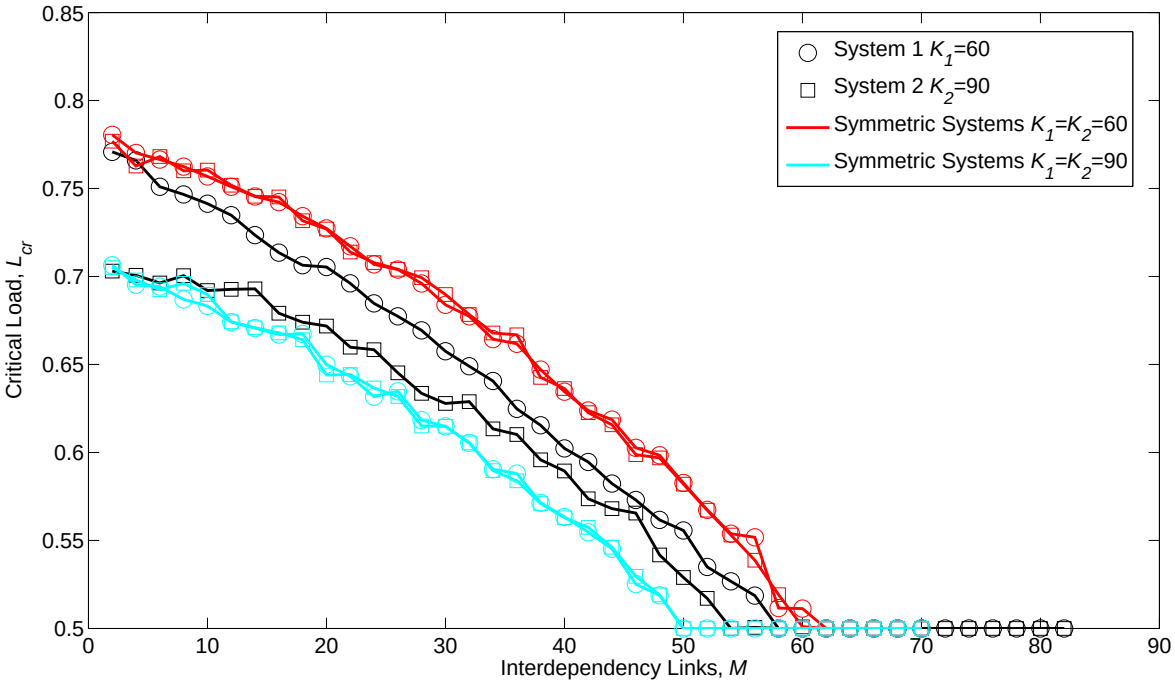

Figure 4.11: The critical loads, L^1_{cr} (black circles) and L^2_{cr} (black squares), vs. the interdependency links, M, for two asymmetric interdependent networks having $K_1 = 60$ and $K_2 = 90$ system links, shown in Fig. 4.1. The results for two sets of symmetric interdependent networks with $K_1 = K_2 = 60$ (red markers and line) and $K_1 = K_2 = 90$ (cyan markers and line), respectively, are also shown for comparison. $N_1 = N_2 = 24$.

configuration. For example, in the asymmetric configuration, the cascade-safe region are $L^1 = [0.5,\ 0.658]$ and $L^2 = [0.5,\ 0.628]$ (black markers), while in the symmetric configuration $L^1 = [0.5,\ 0.684]$ (red marker) and $L^2 = [0.5,\ 0.615]$ (cyan marker), for $M = 30$.

An equivalent behavior was shown to be valid in all the considered asymmetric cases. Therefore, the analysis of asymmetric configuration with $K_1 = k_1$ and $K_2 = k_2$ is encompassed by the analysis of two symmetric interdependent configurations with $K_1 = K_2 = k_1$ and $K_1 = K_2 = k_2$, respectively. Thus, the results of the analyses on symmetric interdependent networks are employed in assessing the limitations that the structures of asymmetric interdependent networks impose on their own operations.

4.5 Optimal interdependency connectivity

In this Section, the second of the two fundamental issues in the design of interdependent networks is addressed, namely, what is the most efficient interconnection among interdependent networks that minimizes the propagations of cascading failures in them. In particular, we assess how different configurations of the system links and of the interdependency links, i.e. the pairs $(K_1 = K_2 = K, M)$, contribute to the interdependency efficiency, E_i, and affect the propagation of cascading failures in the two symmetric interdependent networks, in terms of the critical loads, L_{cr}^1 and L_{cr}^2 defined in Section 4.3.2. To this end, the results of Sections 4.2.1, 4.2.2, 4.2.3 and 4.4.1 are employed. Symmetric interdependent networks with $N_1 = N_2 = 24$ nodes are considered in this analysis. As seen in Section 4.4.2 the results obtained for these configurations encompass the results for asymmetric interdependent networks with $N_1 = N_2 = 24$ nodes.

In Fig. 4.12, the relation, $E_i = f(K, M)$, between the configuration of the interdependent networks, i.e. (K, M), and the interdependency efficiency, E_i, and the relation, $L_{cr} = f(K, M)$, between the configuration of the interdependent networks, i.e. (K, M), and the average critical load of the two symmetric networks, $L_{cr} = (L_{cr}^1 + L_{cr}^2)/2$, are presented. As seen in Section 4.4.1, the average critical load, L_{cr}, is representative of the two critical loads in the symmetric networks. Indeed, L_{cr}^1 and L_{cr}^2 almost completely overlap since cascading failures similarly arise and propagate in them. Each point (K, M) of the diagram in Fig. 4.12 corresponds to a particular configuration of the interdependent networks as for the system links, K, and the interdependencies, M, and it is associated to a unique E_i value and a unique L_{cr} value.

The small black dots and the solid black lines define the contour lines of the relation, $E_i = f(K, M)$, along which the interdependency efficiency, E_i, has a constant value. Seven contour lines are shown whose range of variation is $E_i \in [0.4,\ 0.7]$ at steps of 0.05. In a similar way, the large black dots and the black dash dotted lines define the contour lines of the relation, $L_{cr} = f(K, M)$, along which the critical load, L_{cr}, has a constant value. Nine contour lines are shown whose range of variation is $L_{cr} \in [0.5,\ 0.9]$ at steps of 0.05. The red dots and the red dash dotted line identify the system configurations for which the

efficiency ratio, ρ, defined in Section 4.2.3, Eq. 4.6, is equal to one. For the configurations (K, M) on the left of this line (red shaded region), $\rho > 1$. As pointed out in Section 4.2.3, these configurations cannot be treated within the formalism of the interdependent network analysis.

As the system size increases, i.e. K and M increase, the interdependency efficiency, E_i, also increases since the two interdependent networks communicate more effectively. Conversely, as the system size increases, i.e. K and M increase, the critical load, L_{cr}, decreases since the two interdependent networks become more vulnerable to the propagation of cascading failures. From Fig. 4.12, we notice that the contour lines for $E_i = f(K, M)$ have the same functional form that is translated on the (K, M) plane to account for varying E_i values. The same behavior holds for the contour lines $L_{cr} = f(K, M)$. In particular, the functional form of the contour lines for $E_i = f(K, M)$ only depends on K and E_i through the relation,

$$M = (a + b \cdot E_i + c \cdot E_i^2 + d \cdot E_i^3) \cdot E_i/K + const, \tag{4.7}$$

with $a = -0.24591 \cdot 10^5$, $b = 1.8894 \cdot 10^5$, $c = -4.2903 \cdot 10^5$ and $d = 3.2645 \cdot 10^5$. These coefficients are the parameters that characterize the contour lines for $E_i = f(K, M)$ for all the system configurations (K, M) and interdependency efficiencies, E_i. The red solid curves in Fig. 4.12 show how the functional form in Eq. 4.7 fits the contour lines for $E_i = f(K, M)$ in the least-square sense. The agreement is particularly good for large M values.

Since the contour lines of the relation, $E_i = f(K, M)$, are convex functions, and, conversely, the contour lines of the relation, $L_{cr} = f(K, M)$, are upper convex functions, it is possible to identify the optimal configuration, (K^{opt}, M^{opt}), that minimizes the propagation of cascading failure, i.e. that maximizes L_{cr}, for every E_i values. These optimal configurations, (K^{opt}, M^{opt}), are the tangent points of the contour lines for $E_i = f(K, M)$ and for $L_{cr} = f(K, M)$. The blue dots in Fig. 4.12 identify seven optimal configurations for different values of interdependency efficiency, E_i. They lie on the line which is the locus of the optimal configurations, i.e. the points in the (K, M) plane that maximize the critical load, L_{cr}, for each E_i. The relation between M^{opt} and K^{opt} is found through least-square linear fit of the optimal configurations,

$$M^{opt} = \left[0.4020 \cdot K^{opt} - 9.4895\right], \tag{4.8}$$

which is plotted as a blue solid line in Fig. 4.12. The square brackets in Eq. 4.8 denote the nearest integer function. This relation is useful in designing optimum interdependencies between two networks having $K_1 = K_2 = K$. If there are no constraints on the number of interdependencies, M, a value close to $M^{opt} = [0.4020 \cdot K - 9.4895]$ should be selected to find the best compromise between the interdependency efficiency, E_i, and the critical load, L_{cr}. This choice maximizes the communication between the two interdependent networks, while at the same time reduces their vulnerability to the propagation of cascading failures. From Eq. 4.8, we notice that the optimal number of interdependencies, M^{opt}, is always smaller than a third of the number of system links, K. Additional interdependencies would increase the vulnerability towards cascading failures more than they would contribute to the communication between the two interdependent networks. It is important to stress that Eq. 4.8 is valid only within the range of system configurations, (K, M), used for its development, i.e. $K \in [34,\ 120]$ and $M \in [4,\ 39]$.

From Fig. 4.12, several network system design considerations can be thus induced. For example, the same interdependency efficiency, $E_i = 0.6$, is obtained for the configurations $(K = 45, M = 44)$ and $(K = 111, M = 5)$. Moreover, these two configurations of interdependent networks have the same vulnerability towards cascading failures since $L_{cr} = 0.65$. In this case, other considerations related to the possible congestion of the five nodes in each network (for the $(K = 111, M = 5)$ configuration) that handle the entire interdependency connectivity will guide to the choice of the best configuration. If a maximum number of system links, $K = \bar{K}$, and a minimum interdependency efficiency, $E_i = \bar{E}$, are prescribed, then the optimum number of interdependencies, $M = \bar{M}$, is found at the intersection between the line $K = \bar{K}$ and the contour line $E_i = \bar{E}$. If $M < \bar{M}$, the constraint on the minimum interdependency efficiency is not satisfied, while if $M > \bar{M}$, the cascade-safe region shrinks. If the constraint on the number of system links, $K = \bar{K}$, is dropped, then a configuration on the contour line $E_i = \bar{E}$, but closer to the locus of the optimal configurations defined in Eq. 4.8, can be selected.

Alternatively, if $M = 30$ connections must be established among the nodes of two inter-

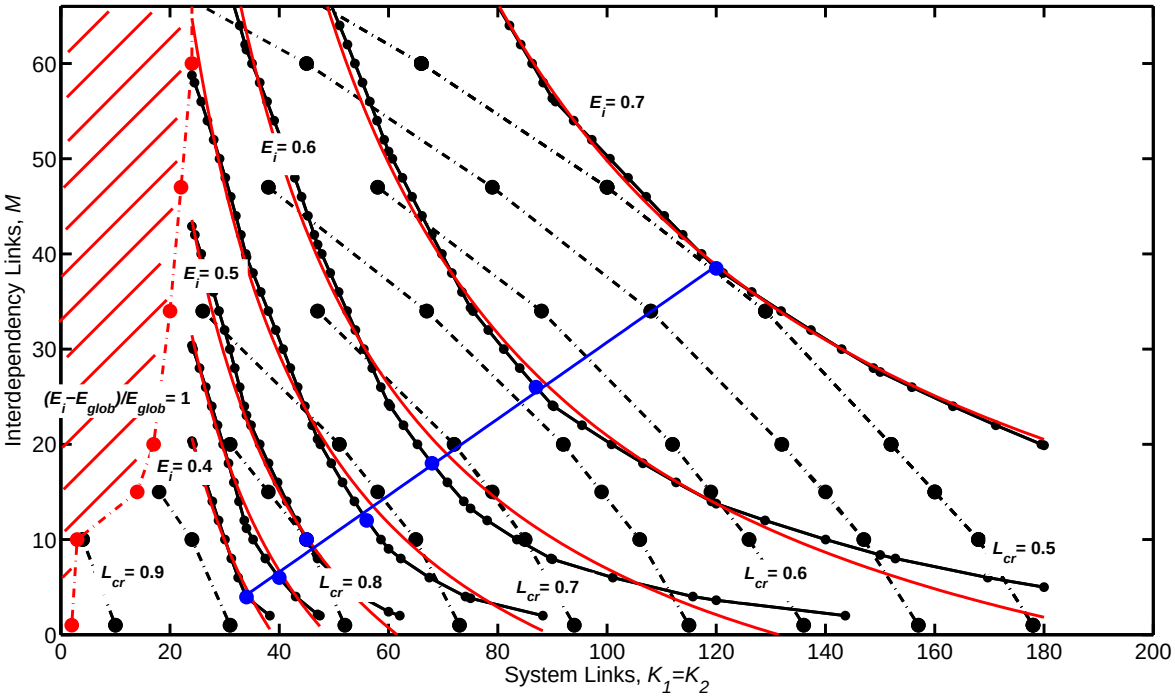

Figure 4.12: The relation, $E_i = f(K, M)$, between the configuration of the interdependent networks, i.e. (K, M), and the interdependency efficiency, E_i, and the relation, $L_{cr} = f(K, M)$, between the configuration of the interdependent networks, i.e. (K, M), and the average critical loads of the two symmetric networks, L_{cr}. Each point (K, M) corresponds to a particular configuration of the interdependent networks as for the system links, K, and the interdependencies, M, and it is associated to a unique E_i value and a unique L_{cr} value. Small black dots and solid black lines: contour lines of the relation, $E_i = f(K, M)$. Big black dots and black dash dotted lines: contour lines of the relation, $L_{cr} = f(K, M)$. Red dots and red dash dotted line: system configurations for which $\rho = 1$. Red shaded area: system configurations for which $\rho > 1$. The red solid curves show how the functional form in Eq. 4.7 fits the contour lines for $E_i = f(K, M)$ in the least-square sense. Blue dots: optimal configurations for different values of interdependency efficiency, E_i. Blue solid line: locus of the optimal configurations, (K^{opt}, M^{opt}).

dependent networks, e.g. thirty calls between two wireless communication networks, no more than $K = 54$ calls can be allowed within each of the two networks if the critical load cannot be lower than 0.70, i.e. the cascade-safe region cannot be smaller than $L_i \in [0.5,\ 0.7]$. On the other hand, if the communication efficiency within the two networks has to be increased, i.e. $K = 85$ calls are established within the two wireless communication networks, then the number of calls between the two interdependent networks must be limited to $M = 10$, for the cascade-safe region to be unchanged.

Chapter 5

Critical phenomena in complex networks

The extreme compactness of networks together with their complex organization result in a broad spectrum of nontraditional critical effects and singularities (79). Critical phenomena in networks include a wide range of issues:

- Structural changes in the connectivity pattern, e.g. a finite fraction of edges turns out to be aggregated into an ultra compact subgraph with diameter, $d = max(d_{ij})$ (the largest entry of the shortest path lengths matrix, $\{d_{ij}\}$, see Section 2.1), much smaller than the diameter of the network (80);

- The emergence of critical scale-free network architectures, i.e. the degree distribution, $P(k)$, of the growing network tends to a power-law function with significant probability of highly connected nodes (hubs) (7);

- Percolation phenomena, i.e. the conditions for the emergence of a giant connected component (81);

- Epidemic thresholds and phase transitions, e.g. the disappearance of the epidemic threshold in uncorrelated infinite networks (i.e. where there is no correlation between degrees of vertices) (11).

Complex networks imply a new type of strong disorder where fluctuations of structural characteristics of vertices (e.g., their degree distribution) far exceed their mean values. One should add to this large-scale inhomogeneity, which is significant in many complex networks, that statistical properties of vertices may strongly differ in different parts of a network.

Critical phenomena in complex network mark the appearance of emerging properties and phenomena in the mapped systems and can be exploited to characterize transitions and thresholds in their dynamics (13). In particular, the emergence and the full development of a giant component in nonequilibrium, i.e. growing, networks is the basic structural transition in their architecture.

5.1 Percolation transition: the formation of a giant component

The giant component of a network is a connected set of nodes that consists of the majority of the network and its presence can be ascertained through the evaluation of the network's community structure. Finding the community structure of a network entails grouping its nodes in clusters, i.e. unconnected sets of nodes; then, the size of each cluster can be evaluated. The cluster with the largest size is called giant component of the network.

Percolation theory is the study of the qualitative change in connectivity of a nonequilibrium network as its nodes and edges are randomly removed or added (12). In order to clarify the concept of bond percolation transition, consider for example a very simple network, i.e. the 40×40 square lattice in Fig. 5.1. In this network, each bond (connection) is present with probability p between two neighboring nodes of the lattice. The maximum number of bonds is $K_{max} = 2 \cdot 40 \cdot 39 = 3120$. On the average, $K = 3120p$ bonds will be in the lattice. Figure 5.1 shows three computer-generated samples of a 40×40 square lattice, with probability increasing from $p = 0.3\%$ to $p = 0.7\%$. The percolation transition concerns the conditions for the formation of a set of bonds connecting the upper and the lower side of the lattice. Since this cluster spans the entire size of the lattice, it is the giant component. For $p = 0.3$ as in the upper-left panel of Fig. 5.1, there is no path connecting the upper and the lower side and the network breaks up into individual clusters. When the bond probability $p = 0.4176$,

a giant component connecting the upper side and the lower side of the lattice appears. The red highlighted path in the upper-right panel of Fig. 5.1 identifies the connection between the upper and the lower side of the lattice. Therefore, the value $p_c = 0.4176$ is the percolation threshold for this model. If the bonds were pipes carrying some fluid, at $p \geq p_c$ a fluid poured on the upper side of the lattice would percolate though the connections of the giant component reaching the lower side, hence percolation transition. For $p = 0.7 > p_c$, the only cluster in the lattice is the giant component (lower panel in Fig. 5.1).

5.2 Models for evolving networks

In the literature, several network evolution models have been assessed based on different growth rules and the sudden emergence of a giant component used to identify the percolation threshold and the transition to an emergent system behavior (82; 83). These studies aim at evaluating how simple laws of evolution and rules of local interactions among the network elements affect their global development and operations. The knowledge of how the local interactions amount to the global behavior allows control over the dynamics which unfold on their structure, e.g. the propagation of failures, the spreading of diseases, and the formation of community structures. Furthermore, these theoretical models are topological since physical parameters characterizing the links, e.g. their lengths, are not considered when connections are established among nodes.

In Section 5.3, we develop a network evolution model that assesses the percolation transition for a spatial network whose nodes are located in the two-dimensional Euclidean space. Nodes are randomly added onto the surface and interconnected according to their spatial proximity. Therefore, unlike the topological models, there is an interplay between the connectivity pattern of the network and the substrate in which nodes are added. This model for evolving networks simulates the metastatic colonization in tumor growth and, specifically, the emergence of a collective behavior in the metastatic cell aggregate. The new system behavior identifies the formation of overt macrometastases which can mount an effective attach to the host organ.

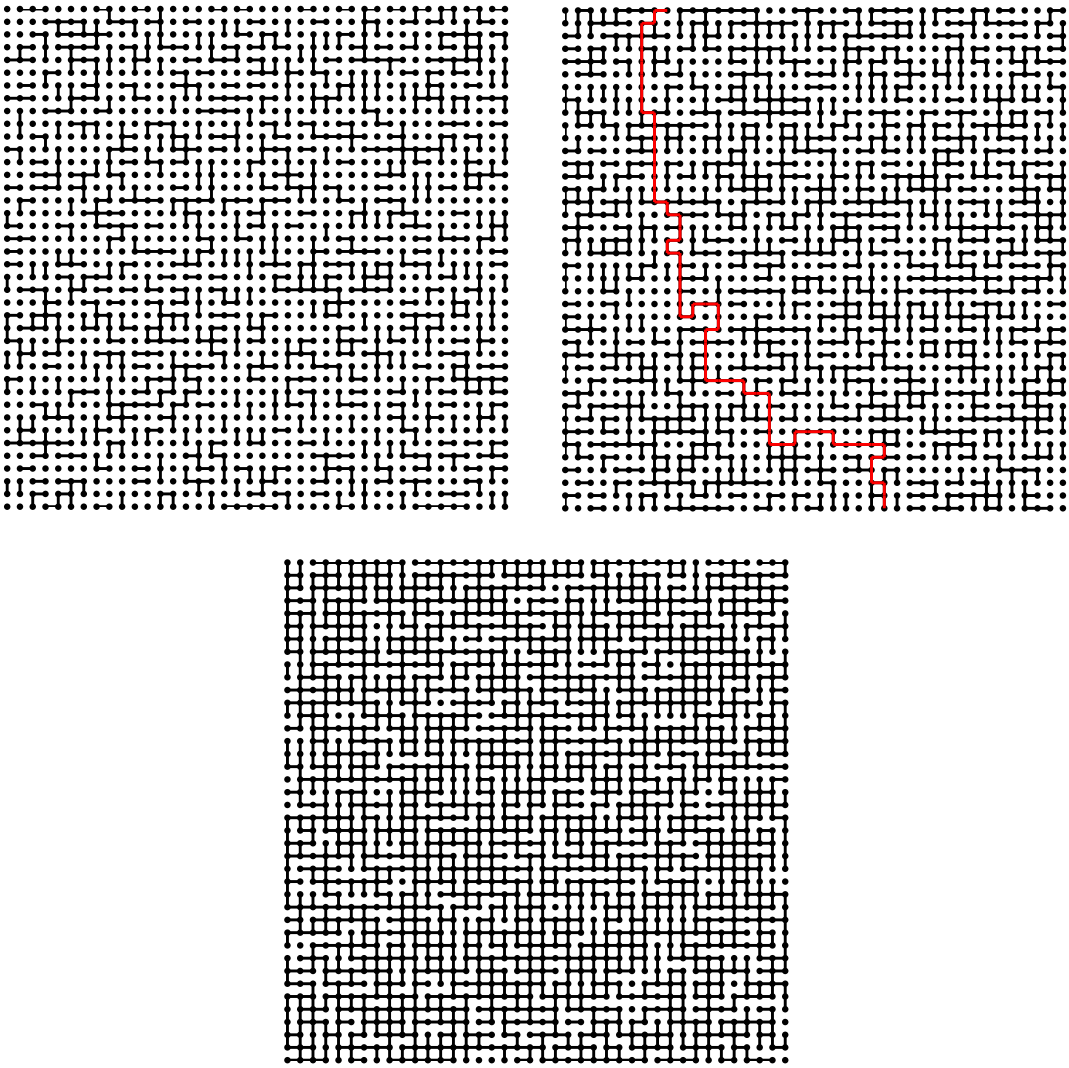

Figure 5.1: Bond percolation network. Each bond (connection) on a 40×40 square lattice is present with probability $p = 0.3$ (upper-left panel), $p = 0.4176$ (upper-right panel) and $p = 0.7$ (lower panel). The value $p_c = 0.4176$ is the percolation threshold for this model for which a giant component connecting the upper side and the lower side of the lattice appears. The red path highlights this connection. For $p = 0.3 < p_c$, many small-sized individual clusters appear in the lattice. For $p = 0.7 > p_c$, the only cluster in the lattice is the giant component.

5.3 Emergence of macrometastases as a percolation transition in a metastatic colonization network

An estimated 1,479,350 new cancer cases and 562,340 deaths from cancer were expected to occur in the United States alone in the latest 2009 projection (84). The majority of those deaths were caused by metastatic lesions far from the primary tumor site.

Metastases are not direct extensions of a primary tumor and their dissemination does not typically occur following the general routing paths in the body, e.g. the blood or lymphatic streams. Instead, metastases arise following the spread of neoplastic cells from the primary tumor site to secondary organs where they form secondary tumors (85).

It is a generally accepted assumption that metastatic colonization in tumors occurs in a stepwise fashion (86–88). Upon leaving the primary tumor, cells release growth factors, e.g. vascular endothelial growth factor A (VEGFA) (89), placental growth factor (PIGF) (89) and transforming growth factor-β (TGFβ) (86), which prime distant sites for future seeding. In turn, cells at secondary sites release guidance chemicals, e.g. inflammatory S100 chemokines and serum amyloid A3 (SAA3) (86; 90), which attract migratory tumor cells.

Recent experimental observations (91) have led to the hypothesis that metastatic colonization and growth are regulated by a process similar to quorum sensing in bacterial biofilm formation (92–95). Following this analogy, metastatic cells produce, release and detect chemicals, called autoinducers, which allow intercellular communications. Cells sense changes in their numbers and density following variations in the autoinducer concentrations. At a critical signaling threshold level, they stop acting as individuals and initiate community behaviors, e.g., promoting the transition from microscopic colonies to overt macrometastases at a preferred second site in the host organ.

We present a model of metastatic colonization based on network theory (8; 79). We demonstrate the occurrence of a percolation transition in the giant component, which is a cluster that spans the entire network, of the metastasized network at a critical cell density. This transition is implicitly based on the intercellular signaling within the metastasis. The formation of a giant component in a growing network that has a complex architecture is considered to be an emergent critical phenomenon. The sudden emergence of a giant com-

ponent is the hallmark of the percolation transition, which marks the onset of a new system behavior (82; 83). In this particular case, the new system behavior is the formation of overt macrometastases which can mount an effective attach to the host organ.

Mathematical models for tumor growth follow different approaches. Stochastic/discrete models (96) incorporate parameters and biological rules discovered from cell research but are limited to analyses of small developing tumors due to the computational burden imposed by the modeling of intercellular interaction. On the other hand, deterministic/continuous models (97–101) regard tumors as spatial distributions of cell densities allowing tumors of clinically significant size to be modeled, but lack the capability to simulate cell-to-cell interactions.

Here we propose a model belonging to the stochastic/discrete category. Our results are the first attempt to provide a model accounting for the intercellular sensing hypothesis during metastatic colonization. We demonstrate that the transition from micro- to macrometastases is an intrinsic characteristic of metastatic growth, which emerges globally through local interactions among cells.

5.3.1 Model and methods

5.3.1.1 Basic colonization model

We simulate the evolution of the metastatic colonization on a surface area of the preferred second site to which the tumor cells are attracted. The chemotactic gradients towards the second site directly influence the attachment rate α to the surface. Following attachment, tumor cells may be removed at a rate β due to apoptosis, necrosis or detachment. Since the attachment surface is the preferential target for metastatic cells, they are placed on it with a uniform probability that they will occupy a specific location. Intercellular communication occurs within a cut-off distance ρ. Thus, the tumor cell covers a circular sensing area of radius ρ about itself and, if another cell lies within it, cell-to-cell talk is established.

The evolving metastatic aggregate is mapped into a network structure whose nodes are the metastatic cells with connections that link communicating cells. Figure 5.2 displays a schematic of the network which maps the metastatic colony. The nodes (or vertices) of the

network map the metastatic cells. A connection between two nodes is established if the corresponding cells lie within a cut-off distance ρ. The breadth-first search algorithm (2) is employed to discover the nodes that belong to the giant component of the metastatic network.

We monitor the temporal evolution of the giant component and find that it exhibits a structural transition within two critical times, namely the transition threshold time when the giant component first appears and the fully-developed threshold time when it spans the entire target surface. Figure 5.3 presents the evolution of the size of the giant component for increasing target areas. All of the simulated scenarios share the emergence of the giant component during the percolation transition. As expected, wider homing surfaces at preferred secondary sites lead to larger transition times due to the associated lower probability of communication among the uniformly positioned cells.

The large fluctuations in the size of the giant component, e.g. the one occurring after $t = 8$ years for $A = 1$ cm^2 in Fig. 5.3, stem from the stochastic nature of the colonization model. During the formation and the growth of the giant component, it may be formed by two strongly connected sets of cells loosely linked by only one cell. In case this cell bridging the two sets of cells is removed due to apoptosis, necrosis or detachment, this massive set of cells is split into two components. The size of the giant component suddenly drops down to the size of the new largest connected component which is realized in the network mapping the metastasis.

The same structural transition in the size of the giant component can be identified with respect to the cell density within the metastasis. Thereby, the transition threshold density and the fully-developed threshold density can be identified as the cell density at which the giant component first appears and the cell density at which it spans the entire target surface, respectively.

The percolation transition in the size of the giant connected component identifies the shift from micro- to macrometastases. It is bounded between the transition threshold time and the fully developed threshold time (represented by dots in Fig. 5.3). Before the transition threshold, the metastatic network contains no giant component. After the fully developed threshold, the giant component grows linearly with the net rate $\alpha - \beta$ since incoming cells attach directly to the giant component.

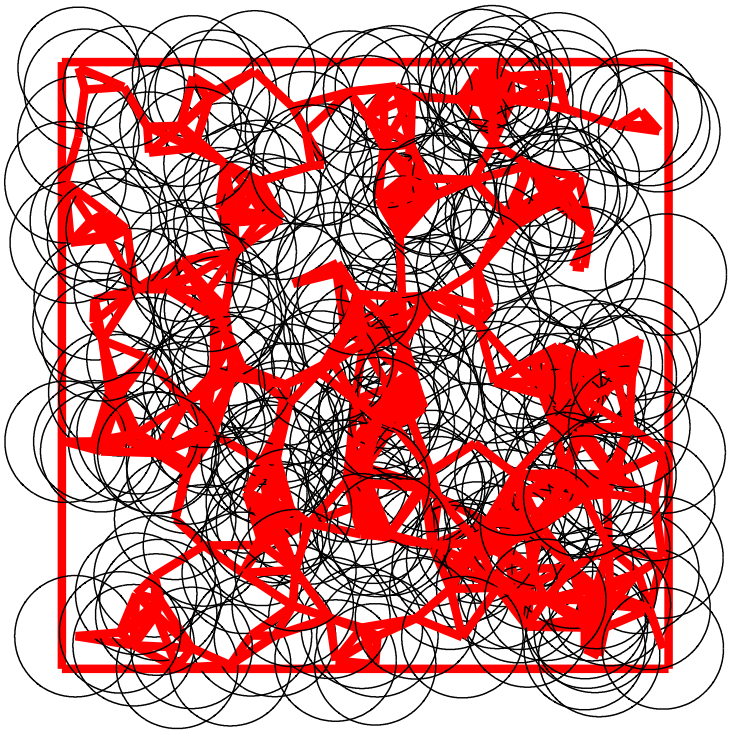

Figure 5.2: The formation of the metastatic network. This schematic displays how the metastatic colony is mapped into a network. The circles represent the sensing areas covered by the tumor cells in accord with the cut-off distance ρ. The cells are placed at the centers of the circles. The homing surface for colonization is bounded by the red square contour and the cells attach uniformly on it. The red connections link intercommunicating cells which lie within the distance ρ. The figure corresponds to a stage of the metastasis progression when the giant component spans the entire homing surface. To increase visibility in this schematic, the ratio between the homing surface side and ρ is set as 10.

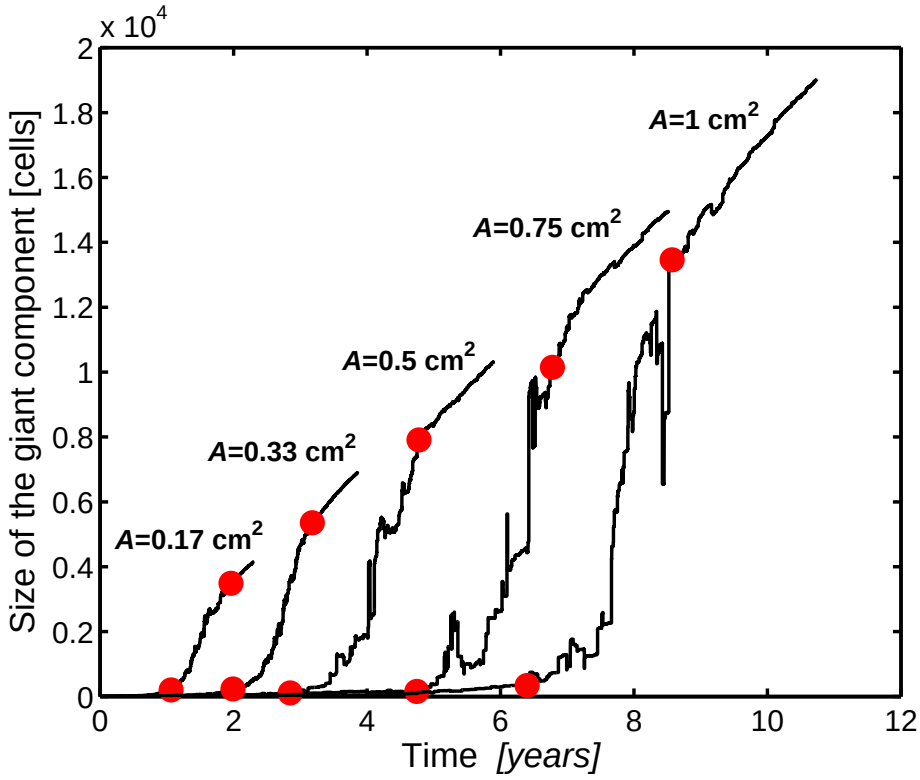

Figure 5.3: Evolution of the giant component in the metastatic network. The results for various target areas are displayed. From right to left, $A = 1, 0.75, 0.5, 0.33, 0.17$ cm^2, respectively. The dots identify the transition threshold time and the fully-developed threshold time of the percolation transition based on the time derivative of the size of the giant component. Three qualitatively different behaviors are found in all the scenarios. Before the transition threshold, the metastatic network contains no giant component, since there are only small disconnected cell clusters. During the transition, incoming cells connect these previously isolated clusters so that a giant component spanning the entire network is formed. After the fully-developed threshold, the giant component grows linearly according to a net rate $\alpha - \beta$ since incoming cells attach directly to it. In these simulations, $\alpha = 10$ and $\beta = 5$ cells/day. $\rho = 100$ μm is chosen to be 10 times as much as the average metastatic cell radius of 10 μm for breast cancer (102). Different ρ values quantitatively influence the critical transition times and the size of the giant component but do not alter the qualitative model behavior (see Fig. 5.6).

The time derivative of the size of the giant component guides us in our determination of these two extremes (Fig. 5.4). The final growth rate value identifies the transition threshold time. In particular, we presume that the transition threshold time occurs when the time derivative of the size of the giant component becomes larger than the final growth rate (left dot in Fig. 5.4). The time derivative exhibits large oscillations during the percolation transition due to the addition and removal of cells to and from the giant component. The fully developed threshold time occurs when these oscillations disappear (right dot in Fig. 5.4). The transition and the fully developed threshold densities are presumed to be the metastatic cell densities at the transition and the fully developed threshold times, respectively.

The model of metastatic colonization is applied to varying target areas, A, to evaluate the extent to which the colonization is affected by the size of the homing surface where the preferential attachment of cancer cells occurs. Moreover, we show that different values of the cut-off distance, ρ, quantitatively influence the critical transition times and densities but do not alter the qualitative behavior of the model.

5.3.1.2 Extensions to the basic metastatic colonization model

Biological considerations inspired three possible extensions to the basic metastatic colonization model. The first concerns the chemotactic gradient attracting tumor cells towards the homing site for metastatic colonization. This gradient directly influences the attachment rate α. If the gradient is time-independent, e.g. when the concentration of the guidance chemical which attract migratory tumor cells to second sites is time-independent, α is constant. Time-varying chemotactic gradients result in $\alpha(t)$ being time-dependent. We have considered the influence of time-dependent $\alpha(t)$ on the percolation transition.

The second extension accounts for the simultaneous attachment of multiple cells on the homing surface. Clusters of several tumor cells can detach from the primary tumor site, travel along the blood and lymphatic vessels and extravasate towards the metastatic colony, providing an additional source of metastatic cells. We consider at most the attachment of clusters of two cells since bigger clusters will not readily extravasate towards the metastasis due to their larger dimensions. We assume that the $p_1 = 70\%$ of the attachments involve individual cells and that the remaining $p_2 = 30\%$ are for clusters of two cells. We simulate

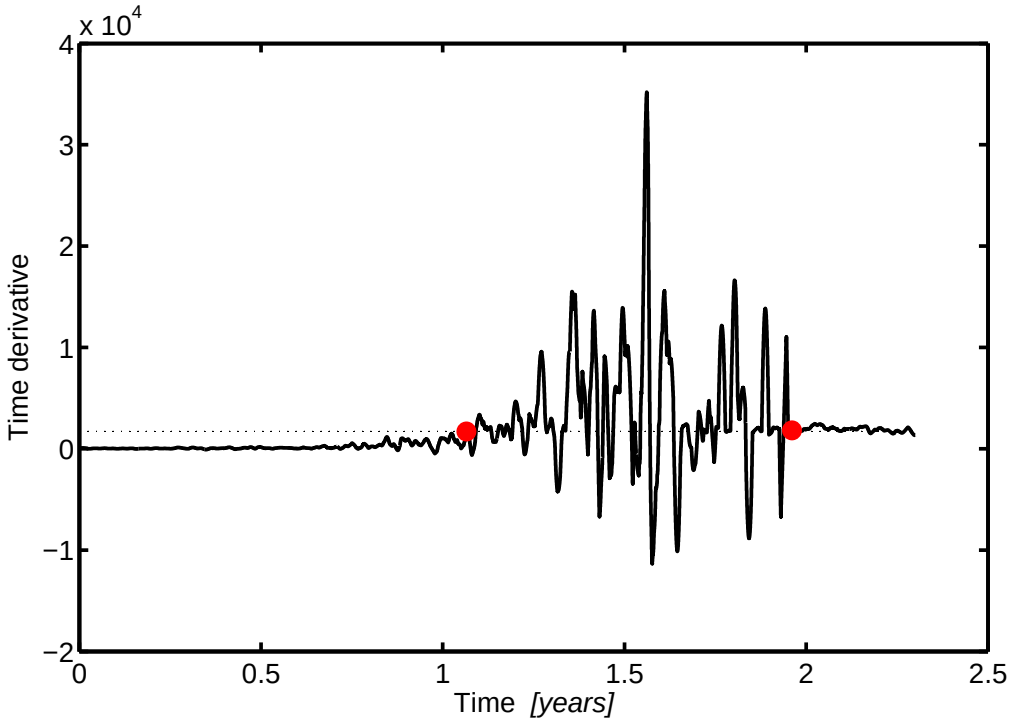

Figure 5.4: The time derivative of the giant component size. The derivative is calculated using least-square regression. This method is chosen due to the high stochastic variability of the signal. For each instant t_i, a t_i-centered time window with length $m = n/100$ is identified, n being the length of the time signal representing the evolution of the giant component size. A first-order polynomial is fitted to the t_i-centered time window and its slope defines the time derivative at t_i. For initial and final times, right- and left-skewed time windows are used, respectively. The dashed line identifies the constant growth rate, R, following the fully-developed transition time. $R = 1800$ cells/year for $\alpha = 10$ cells/day and $\beta = 5$ cells/day. R identifies the transition threshold time (left dot), while the disappearance of large oscillations identifies the fully developed transition time (right dot). This plot is relative to the target area $A = 0.17$ cm^2.

the attachment of multiple cells as follows. The attachment events occur at a rate $\alpha = 10$ cells/day. When an attachment event occurs, based on the corresponding probability, we determine if it involves a single cell or a cluster of two cells. The cells in a cluster are placed in immediate proximity of each other so that the two sensing areas almost completely overlap.

The third extension pertains to the local proliferation of the metastatic cells at the secondary site. Cells that belong to the metastasis replicate, increasing both their number and density. This source term describes the addition of new tumor cells originating from cells within the metastasis without any exogenous contribution. Intercellular sensing also provides a mechanism by which cells can select favorable conditions for replication. For example, cells that are interconnected with many others are more likely to replicate. Thus, we assume that only the cells that belong to the giant component proliferate. The proliferation time T_P is specified as 45 days, which is a typical value for breast cancer (that ranges between one and two months). The proliferation rate is evaluated as $1/T_P$. At each time step, the cells in the giant connected component are examined for proliferation. When a proliferation event occurs, a new cell is placed in the immediate proximity of the replicating cell and thus the two sensing areas overlap almost completely.

The extended model of metastatic colonization is applied to the homing surface with area, $A = 0.33$ cm^2, and the results are compared with those from the basic model. This allows evaluating of the extent to which the three biologically inspired extensions affect the basic metastatic colonization model.

5.3.2 Results and discussion

5.3.2.1 Basic colonization model

Figure 5.5 (b) presents three regions of metastasis progression that are identified in the context of transition times (Fig. 5.3) for homing surfaces with increasing surface areas, A. In these simulations, $\alpha = 10$ and $\beta = 5$ cells/day. $\rho = 100$ μm is chosen to be 10 times as much as the average metastatic cell radius of 10 μm for breast cancer (102). Different ρ values quantitatively influence the critical transition times and the size of the giant component but do not alter the qualitative model behavior (see Fig. 5.6). The blue region below the

transition threshold identifies the early stage of metastatic colonization when cells are characterized by individual behavior. Microcolonies form in the pink region and the transition from micrometastases to macrometastases occurs. The red region above the fully-developed threshold identifies the formation of overt metastases in the host organ. The transition timespan (pink region) is smaller for small homing areas. Thus, in addition to the difficulty of early detection due to their smaller dimensions, metastases with limited spatial extensions take less time to form microcolonies and to fully develop into macrocolonies.

We have also identified the transition threshold density and the fully-developed threshold density corresponding to the threshold times. These results are presented through a three-region diagram for metastasis progression with respect to the cell density within the metastasis (Fig. 5.5 (a)). This diagram shows that an intercellular-sensing-like mechanism is active during the colonization process that enables the metastatic cells to determine if their density and number are sufficient to allow behavior as a community. The transition threshold density remains constant with increasing target area, which is intuitive, although the fully-developed threshold density is sensitive to surface area for smaller targets. However, for the smaller areas, the total cell count in the metastasis is only about 2000 cells which explains the larger variability in the local cell density values. The fact that the threshold densities are weakly dependent on the surface area, A, suggests that the proposed model consistently describes the metastatic colonization for a particular set of the model parameters α, β, ρ.

The diagram in Fig. 5.5 (a) can be applied for specific metastatic colonization by fitting the model parameters α, β, ρ, and the homing area. Using this information, cell density measurements for a specific metastasis could allow a determination of the stage of development of the macrocolony and help guide subsequent interventions to reduce the cell density or population. The model suggests that a reduction in the cell population and density can be effective in promoting a backward transition from macrometastases to micrometastases. Yet, if the colonization process is not stopped, the forward transition from micrometastases to macrometastases will occur again at a later time as incoming tumor cells continue to reach the homing site.

In developing the three region diagram in Fig. 5.5, we specified $\rho = 100$ μm which corresponds to 10 times the average metastatic cell radius 10 μm for breast cancer. Next, we

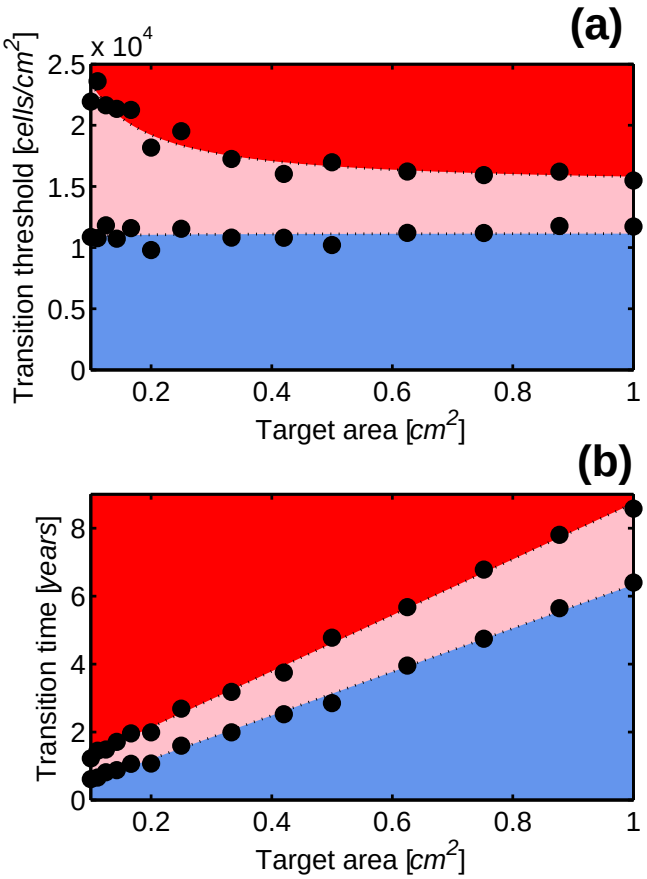

Figure 5.5: Metastatic progression with respect to (a) cell density and (b) critical time for various sizes of the metastasis homing sites. Lower dots: transition thresholds for (a) density and (b) time. Upper dots: fully-developed thresholds for (a) density and (b) time. The threshold time scales linearly with the size of the metastasis homing site while the threshold density is less sensitive to it. This points to to use of intercellular sensing by cells to detect the most convenient density to initiate community behavior. However, the cell number is also a critical parameter in this respect. As an example, for $A = 0.1$ cm^2 the fully-developed metastasis has a size of about 2000 cells, while for $A = 1$ cm^2 this size is about 15,500 cells. Thus, the fully-developed threshold density has higher values for smaller homing sites to compensate for the small cell count in the metastasis. In these simulations, $\alpha = 10$ and $\beta = 5$ cells/day. $\rho = 100$ μm is chosen to be 10 times as much as the average metastatic cell radius of 10 μm for breast cancer (102). Different ρ values quantitatively influence the critical transition times and the size of the giant component but do not alter the qualitative model behavior (see Fig. 5.6).

show that different ρ values quantitatively influence the critical transition times and densities but do not alter the qualitative behavior of the model. Figure 5.6 (a) and (b) presents the three region diagram for metastatic progression that is homologous to Fig. 5.5 (a) and (b) for $\rho = 200$ μm. As expected, the threshold time and density are shifted to lower values due to the augmented sensing area for the metastatic cells. Thus, for increasing ρ values, a smaller number of cells is required to trigger the transition from micro- to macrocolonies in metastasis which, consequently, requires a shorter time to develop into a giant component. This implies that the model can be tuned to describe specific metastatic lesions according to the pertinent intercellular sensing capabilities without loss of generality.

Next, we investigate the percolation transition in the size of the giant component that occurs between the transition threshold time and the fully-developed threshold time. The evolution plot in Fig. 5.3 suggests that there is exponential growth between these two times, which we found to be valid for all the considered scenarios with various target surfaces. Figure 5.7 is a semi logarithm plot of the giant component size vs. time for the homing area $A = 0.1$ cm^2. The plot reveals a linear growth that validates the exponential growth assumption for the giant component size. Least-square regression is used to evaluate the exponential growth rate, γ, between the transition threshold time and the fully developed threshold time.

The slopes of the least-square regression lines for varying homing areas, A, are reported in Fig. 5.8. We notice that the growth rate γ characterizing this exponential growth scales as $\gamma \sim 1/A$. Thus, in addition to the information provided by Fig. 5.5 (b) about the timespan of the transition, we note that while the transition velocity is nonuniform within the transition region (pink area in Fig. 5.5 (b)), it proceeds faster as the fully-developed region (red area in Fig. 5.5 (b)) is approached. The increase in the transition velocity is more pronounced for small homing surfaces (Fig. 5.8), thereby adding more complexity to the growth mechanism. This leads to a reemphasis that there should be prompt intervention following clinical detection of a metastatic tumor due to the intrinsic instability of the transition region.

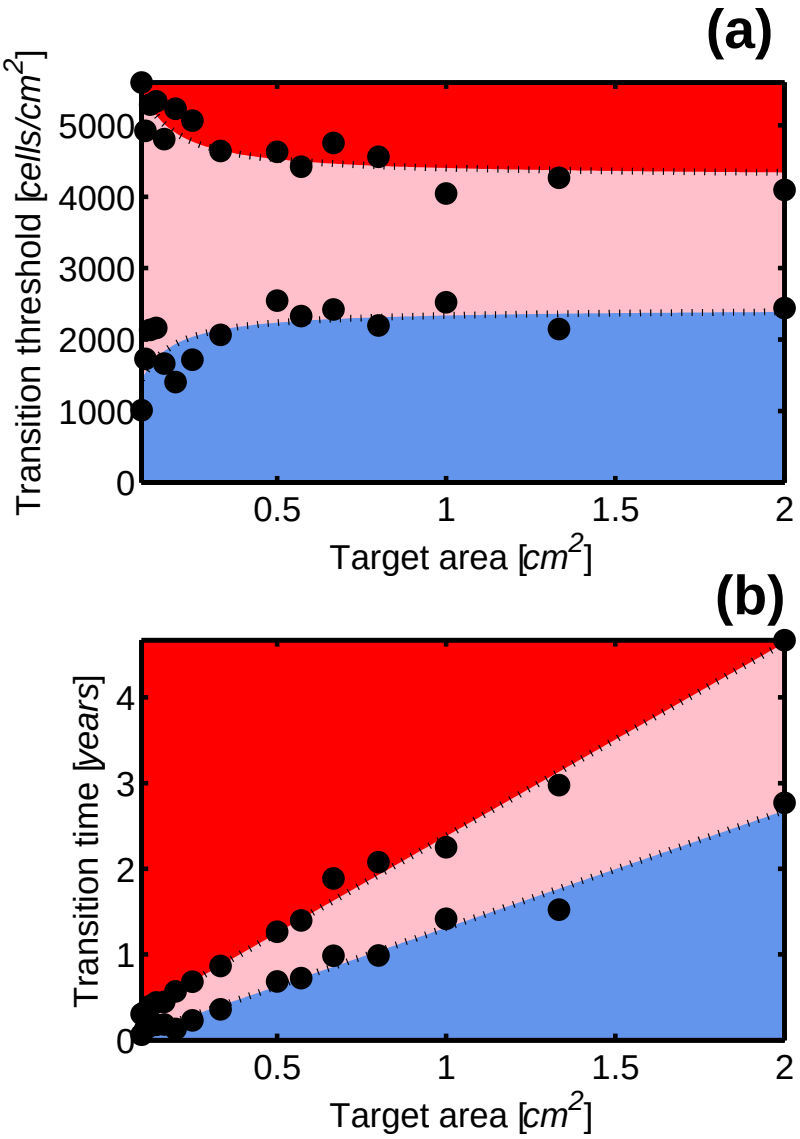

Figure 5.6: Metastatic progression with respect to (a) cell density and (b) critical time. Lower dots: transition thresholds for (a) density and (b) time. Upper dots: fully-developed thresholds for (a) density and (b) time. This figure is the homologue of Fig. 5.5 (a) and (b). The three region diagram is shifted to lower values due to the increase in the cell sensing capability. In this case, $\rho = 200$ μm. $\alpha = 10$ and $\beta = 5$ cells/day as in Fig. 5.5 (a) and (b).

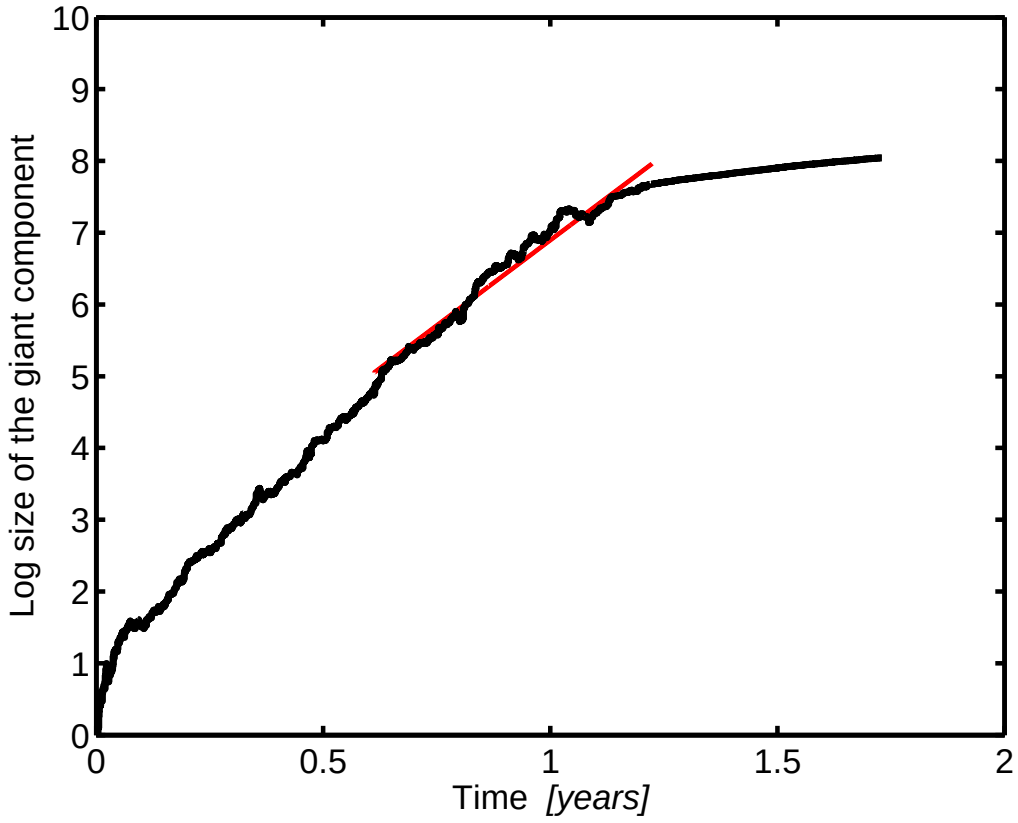

Figure 5.7: Exponential growth between the transition threshold time and the fully developed threshold time. The plot shows the logarithm of the size of the giant component vs. time for $A = 0.1$ cm^2, $\alpha = 10$, $\beta = 5$ cells/day and $\rho = 100$ μm. The red line $4.7558 \cdot t + 2.1381$ identifies the least-square fit between the transition threshold time and the fully developed threshold time with a Pearson correlation coefficient $r^2 = 0.9717$.

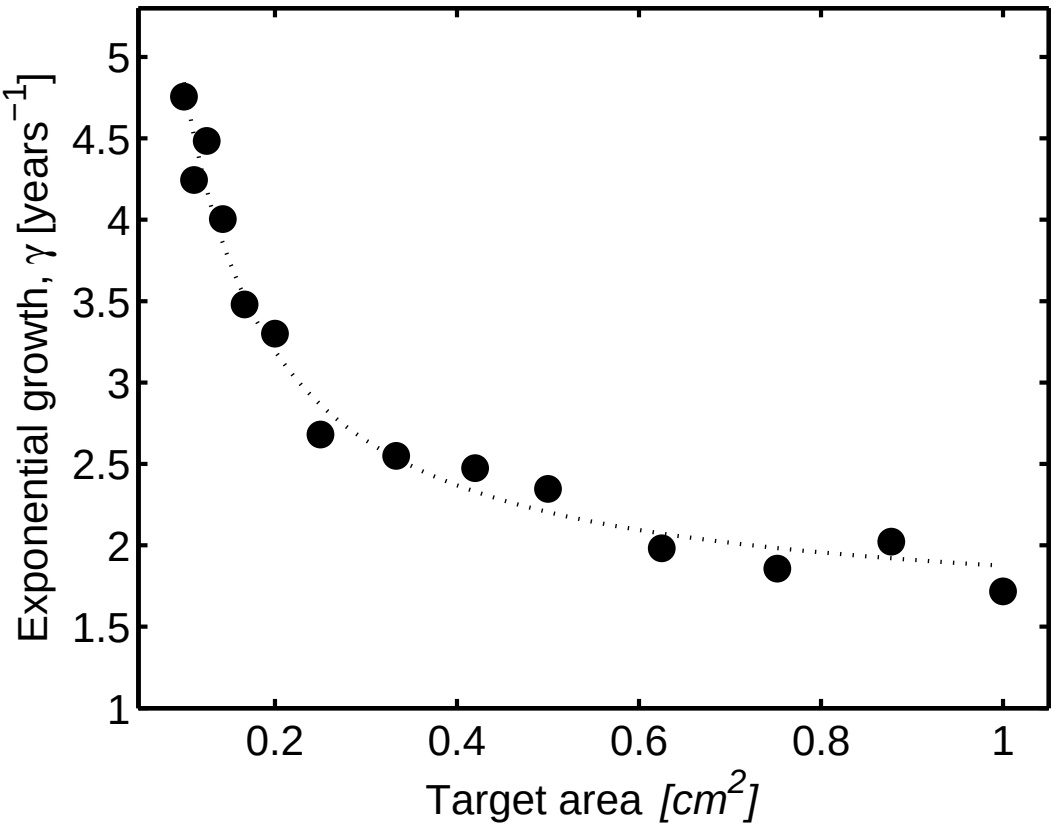

Figure 5.8: Scaling of the exponential growth during the percolation transition. The black dots represent the growth rate of the giant component γ between the transition threshold time and the fully-developed threshold time for increasing metastatic homing area, A. γ scales as $1/A$ (dashed curve) indicating a faster transition for smaller A values (see also Fig. 5.5 (b)). The least-square regression function is $\gamma = 0.33 \cdot 1/A + 1.54$ with Pearson correlation coefficient $r^2 = 0.9758$.

5.3.2.2 Extended colonization model

In this section, we present the results relative to the extended model of metastatic colonization introduced in Section 5.3.1.2. As for the first extension, we considered the effects of a time-varying chemotactic gradient (so that now $\alpha(t)$ is time-dependent) on the percolation transition. The functional form assumed for the attachment rate corresponding to the time-varying chemotactic gradient is quadratic, $\alpha(t) = -2.5 \cdot t^2 + 10 \cdot t + 10$, with a maximum at $t = 2$ years for which there is an increase in the metastatic cell recruitment capability followed by a subsequent decrease. Figures 5.9 and 5.10 present the evolution of the giant component and the evolution of the cell density in the metastasis, respectively, for the time-varying attachment rate, $\alpha(t) = -2.5 \cdot t^2 + 10 \cdot t + 10$, $\beta = 5$ cells/day, $\rho = 100$ μm and a homing area $A = 0.33$ cm^2. The transition and the fully developed thresholds shift towards earlier times due to the increase in metastatic cell recruitment. The transition threshold and the fully developed densities are almost unchanged since the metastatic colonization process is not altered by the time-varying chemotaxis, which does not affect the cell positioning on the homing surface with respect to the base model.

Next, we study the effects of the possible attachments of clusters of multiple cells on the homing surface. Figures 5.11 and 5.12 show the evolution of the giant component and of the cell density in the metastasis, respectively, for the attachment of multiple cells. Like in the previous model extension, the transition threshold and the fully developed threshold times shift towards earlier times due to the increase in metastatic cell recruitment. Yet, the transition occurs at a larger cell density when there is an attachment of multiple cells. This implies that cells in the clusters do not contribute effectively to the intercellular signaling process, since their sensing areas mostly overlap. Hence, multiple cells in clusters connect with the same neighboring cells and do not enhance the global connectivity of the metastatic colony, essentially behaving like single cells in establishing new connections in the metastatic network. Although the colonization speeds up due to the higher effective cell recruitment given by multiple attachments, yet it becomes less efficient since many more cells are required to trigger the percolation transition leading to overt macrometastases.

Finally, the proliferation of the cells belonging to the giant component and the two exten-

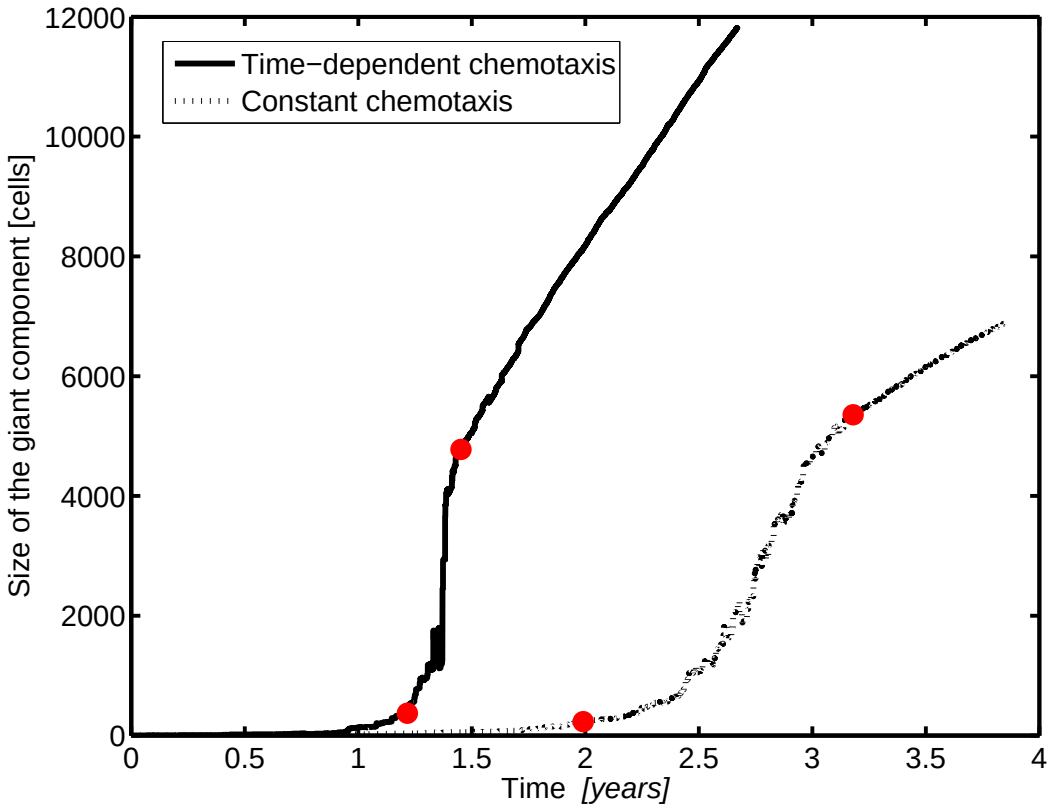

Figure 5.9: Evolution of the giant component for time-varying attachment rate $\alpha(t)$. The solid line shows the results for the time-varying chemotaxis given by the attachment rate $\alpha(t) = -2.5 \cdot t^2 + 10 \cdot t + 10$. The dashed line compares results for constant chemotaxis with $\alpha = 10$ cells/day. The transition threshold time is shifted from 1.99 years to 1.21 years and the fully-developed threshold time is shifted from 3.18 years to 1.45 years, respectively. $A = 0.33$ cm^2, $\beta = 5$ cells/day and $\rho = 100$ μm.

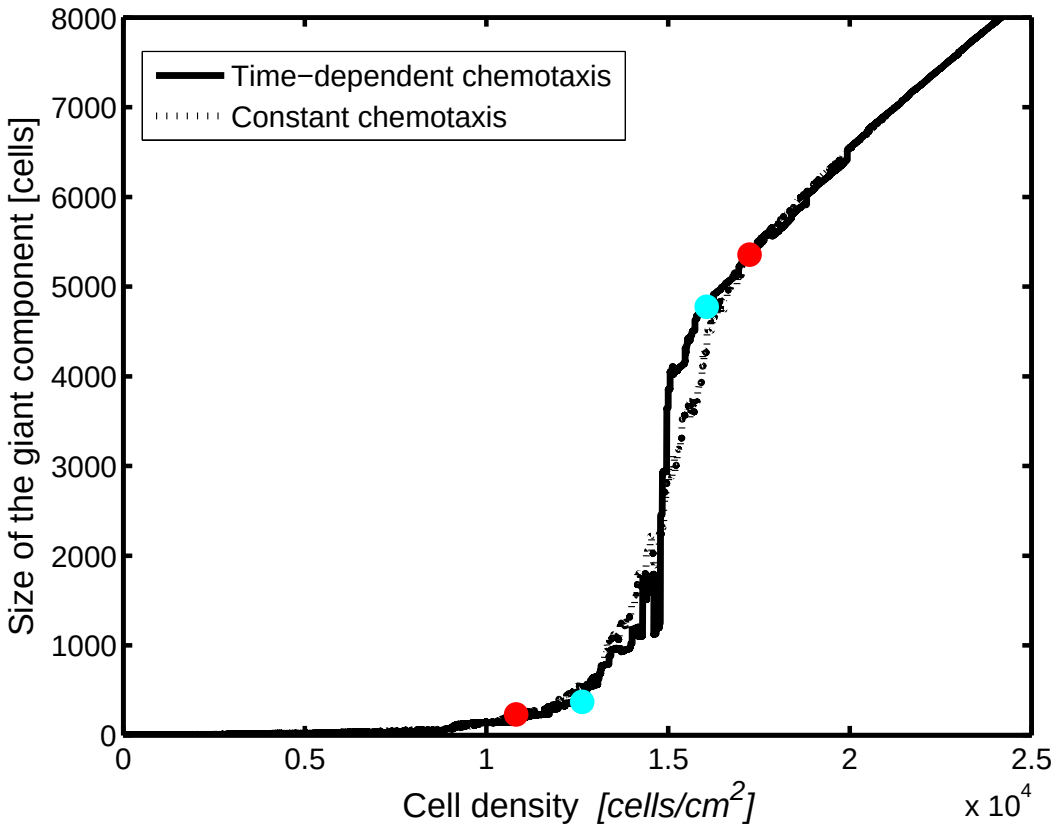

Figure 5.10: Evolution of the cell density for time-varying attachment rate $\alpha(t)$. The solid line represents results for the time-varying chemotaxis given by the attachment rate $\alpha(t) = -2.5 \cdot t^2 + 10 \cdot t + 10$. The dashed line compares results for constant chemotaxis with $\alpha = 10$ cells/day. The cyan dots mark the transition threshold density at $1.26 \cdot 10^4$ cells/cm^2 and the fully-developed threshold density at $1.61 \cdot 10^4$ cells/cm^2 for the time-dependent chemotaxis. The red dots mark the transition threshold density at $1.08 \cdot 10^4$ cells/cm^2 and the fully-developed threshold density at $1.72 \cdot 10^4$ cells/cm^2 for constant chemotaxis. $A = 0.33$ cm^2, $\beta = 5$ cells/day and $\rho = 100$ μm.

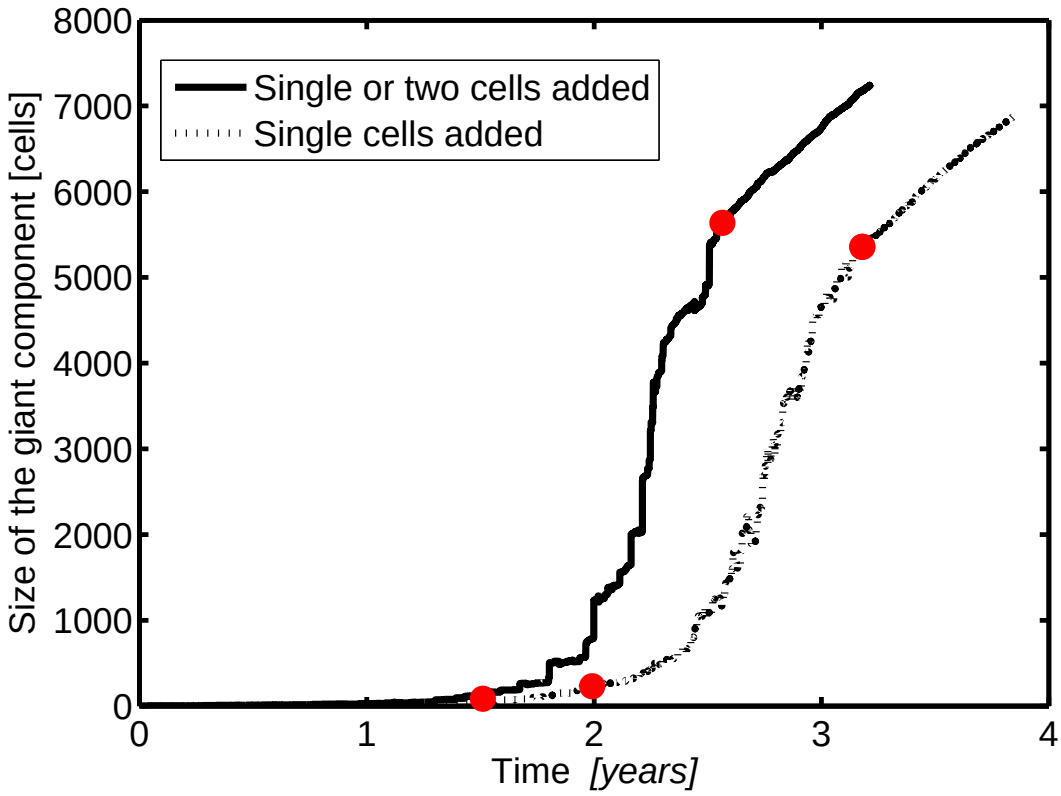

Figure 5.11: Evolution of the giant component size for the attachment of multiple cells. The dashed line shows results for the base model for sake of comparison. The attachment of individual cells occurs with the probability $p_1 = 0.7$ and the attachment of clusters of two cells occurs with the probability $p_2 = 0.3$ with respect to a generic attachment event. The transition threshold time is shifted from 1.99 years to 1.51 years and the fully developed threshold time from 3.18 years to 2.56 years, respectively. $A = 0.33$ cm^2, $\alpha = 10$ cells/day, $\beta = 5$ cells/day and $\rho = 100$ μm.

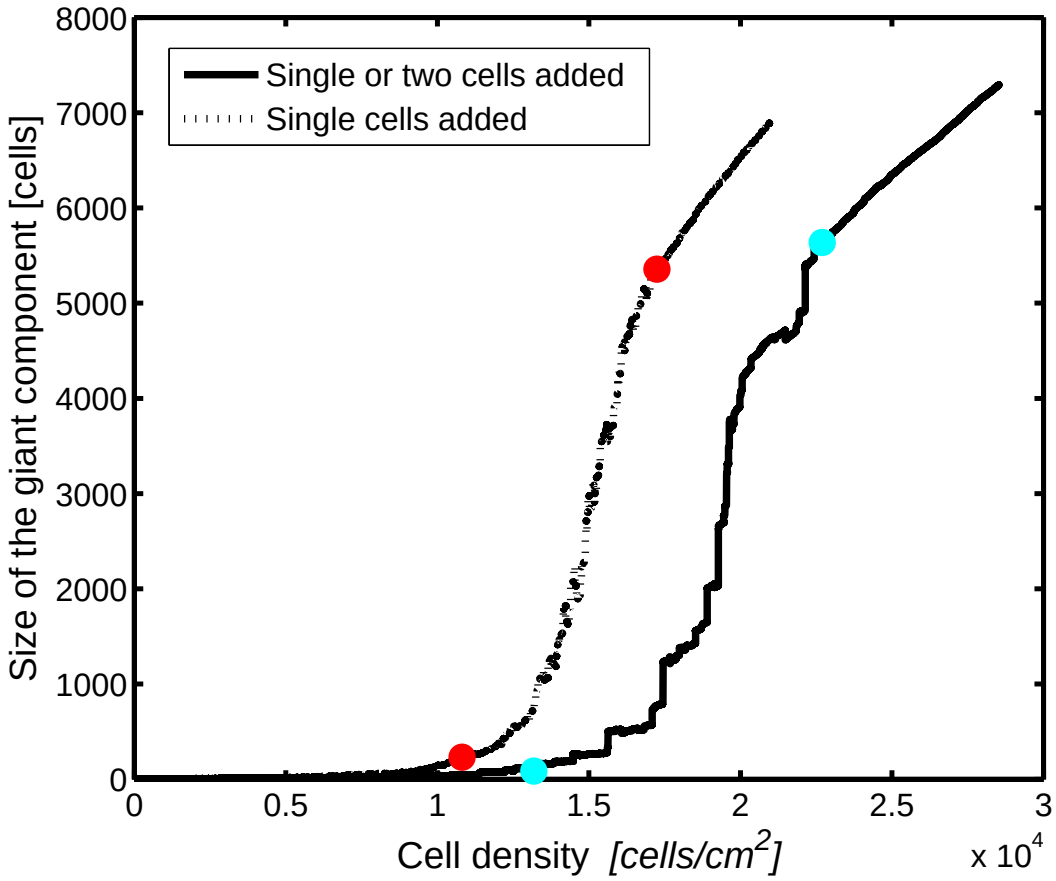

Figure 5.12: Evolution of the cell density for the attachment of multiple cells. The dashed line shows results for the base model for sake of comparison. The attachment of individual cells occurs with the probability $p_1 = 0.7$ and the attachment of clusters of two cells occurs with the probability $p_2 = 0.3$ with respect to a generic attachment event. The cyan dots mark the transition threshold density at $1.32 \cdot 10^4$ cells/cm^2 and the fully-developed threshold density at $2.27 \cdot 10^4$ cells/cm^2 for the attachment of multiple cells. The red dots mark the transition threshold density at $1.08 \cdot 10^4$ cells/cm^2 and the fully-developed threshold density at $1.72 \cdot 10^4$ cells/cm^2 for the base model. $A = 0.33$ cm^2, $\alpha = 10$ cells/day, $\beta = 5$ cells/day and $\rho = 100$ μm.

sions presented above, i.e. the time-varying attachment rate and the attachment of clusters of two cells, namely, are combined. The time-dependent attachment rate $\alpha(t)$ for the simulation of the combined model is reported in Fig. 5.13. After a small initial increase, the attachment rate $\alpha(t)$ decays due to hindered chemotaxis. When $\alpha(t) = \beta$, i.e. $t = 2.38$ years, the detachment rate, β, supersedes the attachment rate, $\alpha(t)$, and proliferation is the only source of cells. Figure 5.14 shows the effects of these extensions on the temporal evolution of the giant component as compared with the basic model. As expected, the transition threshold time decreases as the proliferation source term induces additional growth. Including these three processes during metastatic colonization enhances the growth and hastens the transition of the giant component into overt metastases.

Figure 5.15 shows the evolution of the cell density in the metastasis for a combination of all three model extensions. The transition occurs for a larger cell density in the extended model, mainly due to the overlapping of the sensing areas in the proliferating cells (as discussed above in the context of the attachment of multiple cells). Cell proliferation has a strong influence on the cell density as compared to the effect of time-dependent $\alpha(t)$ (Fig. 5.10) and the attachment of multiple cells (Fig. 5.12) alone. In turn, the density evolution is responsible for the rapid growth in the size of the giant component and for the virtual disappearance of the fully-developed threshold time during the percolation transition (Fig. 5.15).

Therefore, proliferation affects largely the percolation transition so that the evolution of the metastasis from scattered microcolonies to an overt macrocolony takes place in a very short timespan. In these conditions, an intervention aiming at reducing the size of the metastasis to prevent its development is not effective since the colony will suddenly form again.

5.3.3 Conclusions

Despite its geometrical origins, this model for intercellular sensing during metastasis describes the stepwise behavior characteristic of metastatic colonization. It demonstrates that the transition from micro- to macrometastases is an intrinsic characteristic of metastatic growth, which emerges globally through local interactions among cells. The introduction of biologically inspired extensions to the basic colonization model, in particular cell proliferation

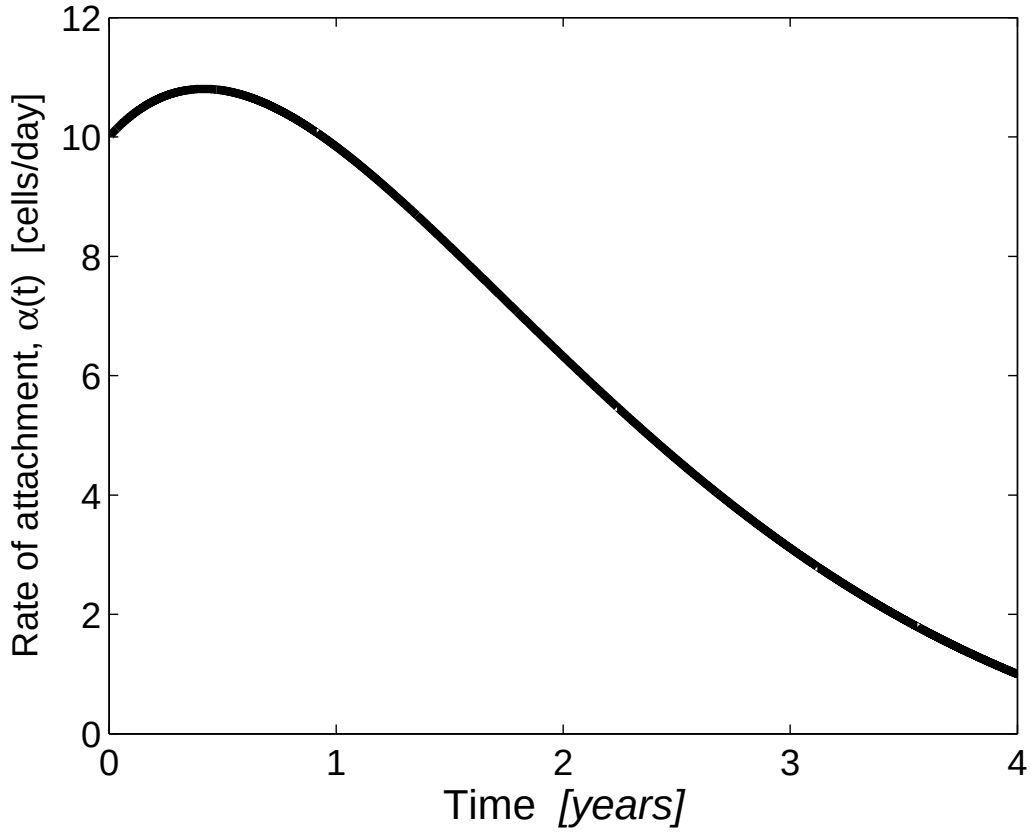

Figure 5.13: Time-varying attachment rate $\alpha(t)$ used for the simulation in Fig. 5.14 and 5.15. The solid line describes the time-dependent attachment rate $\alpha(t) = (-2.5 \cdot t^2 + 10 \cdot t + 10) \cdot e^{-log(10)/4 \cdot t}$ with a maximum at $t = 0.42$ years.

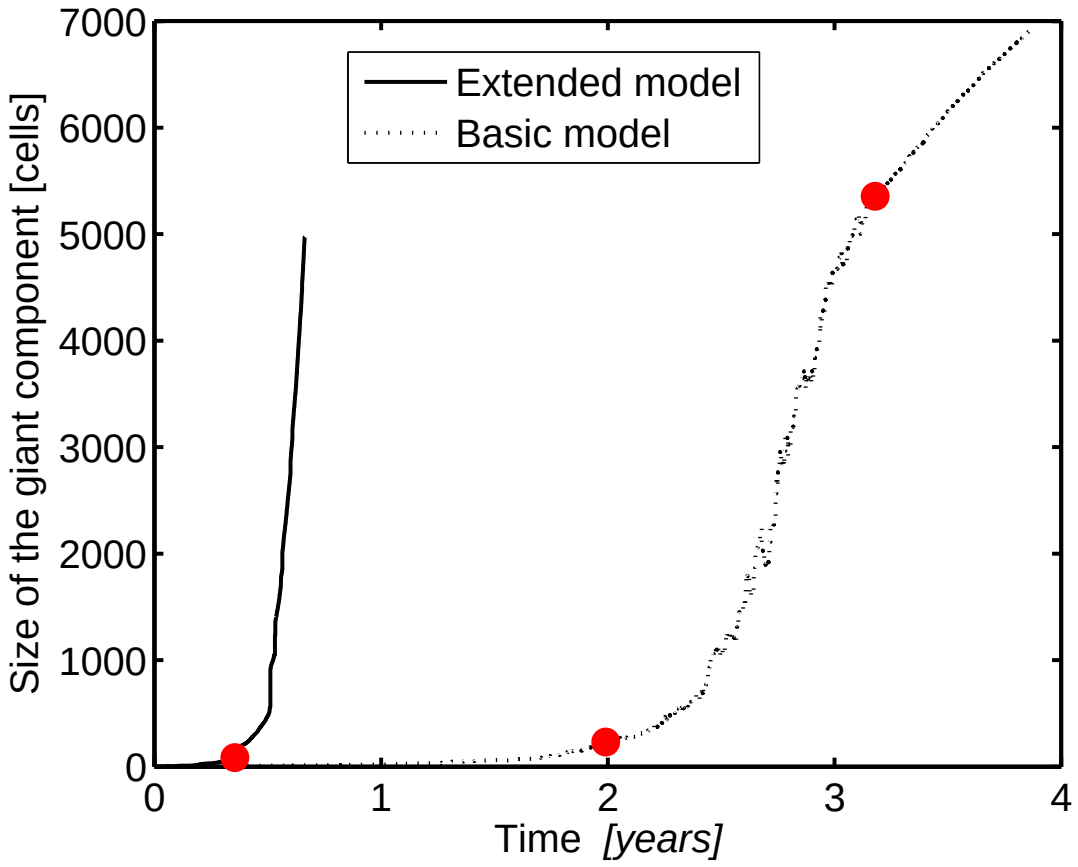

Figure 5.14: Evolution of the giant component in the extended model. Solid line: the result for the extended model considering time-dependent $\alpha(t)$ in Fig. 5.13, attachment of multiple cells, and proliferation. Dashed line: reference model. $\rho = 100$ μm and $A = 0.33$ cm^2. The transition threshold time shifts from 1.99 years to 0.355 years. Due to proliferation, the percolation transition to the fully-developed threshold time is instantaneous. The attachment of individual cells occurs with the probability $p_1 = 0.7$ and the attachment of clusters of two cells occurs with the probability $p_2 = 0.3$ with respect to a generic attachment event. Proliferation occurs only for the cells in the giant connected component with a proliferation time $T_P = 45$ days.

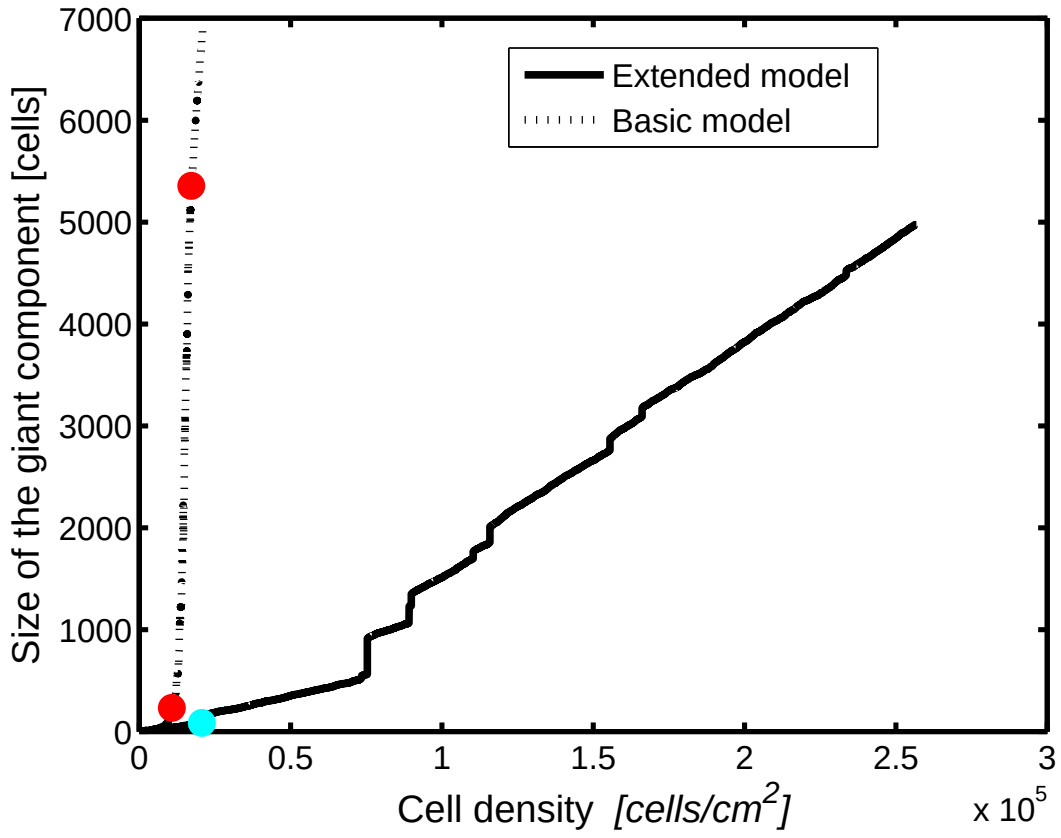

Figure 5.15: Evolution of the cell density for the extended model. Solid line: Result for the extended model considering time-dependent $\alpha(t)$ in Fig. 5.13, attachment of multiple cells, and proliferation. Dashed line: reference model. $A = 0.33$ cm^2 and $\rho = 100$ μm. The transition threshold density shifts from $1.08 \cdot 10^4$ cells/cm^2 (lower red dot) to $2.07 \cdot 10^4$ cells/cm^2 (cyan dot). The attachment of individual cells occurs with a probability $p_1 = 0.7$ and the attachment of clusters of two cells occurs with a probability $p_2 = 0.3$ with respect to a generic attachment event. Proliferation occurs only for cells in the giant connected component with a proliferation time $T_P = 45$ days.

at the secondary site, shortens the time for the percolation transition.

The model can be tuned to describe specific metastatic lesions at specific secondary sites that are caused by different primary tumors to guide proper interventions that seek to reduce the cell population or density.

Furthermore, it prompts the consideration of an intervention that targets the cut-off distance ρ in order to hinder intercellular communication, even in the presence of a significant tumor cell population. This is particularly relevant for those tumor, such as lung and breast cancer, that are highly malignant due to a very prompt and widely spread metastatic colonization.

Chapter 6

Conclusions and open problems

In this dissertation, stochastic and deterministic approaches for modeling complex networks are presented. The methodology combines analysis of the structure formed by the interconnections among the elements of a network with an assessment of the vulnerability towards the propagation of cascading failures. The goal is to understand the mutual interplay between the structure of the network connections and the propagation of cascading failures. Intuitively, an efficient connectivity among the elements of networks is desirable since these systems are designed to establish an effective communication over their links. Nonetheless, as the reachability among the nodes increases, the propagation of undesirable conditions, e.g. network failures, diseases, overloads, is enhanced as well.

Two fundamental issues related to the optimal design and operation of complex networks are addressed. The first concerns the impact that cascading failures have on networks due to the connectivity pattern linking their components. This knowledge is particularly useful during the operation of a network. If the state of load on the network components is high, the risk of cascade spreadings becomes significant. In this case, we have quantified the needed reduction of the connectivity efficiency to prevent the propagation of failures affecting the entire system. Conversely, in networks whose components are working at low loadings, cascades of failure are less likely to arise and propagate. In this case, the reachability among the network elements can be improved through an increase of the connection efficiency, i.e. the addition of new links. The second issue concerns the realization of the most efficient

connectivity in a network that minimizes the propagations of cascading failures. This knowledge is particularly useful during the design of a network. We have found that a system that routinely approaches the critical load for the onset of cascading failures during its operation should have a larger efficiency value. This allows for a smoother transition to the cascade region and for a reasonable reaction time to counteract the onset of significant cascading failures. On the other hand, if there is a need for the critical load for the onset of cascading failures to lie far beyond the operating range of the network, it could be made less vulnerable with fewer connections.

The interplay between the structure of the network connections and the propagation of cascading failures is assessed also in interdependent networks. In these systems, the linking among several network infrastructures is necessary for their optimal and economical operation. Yet, the interdependencies introduce weaknesses in the systems due to the fact that failures may cascade from one system to other interdependent systems, possibly affecting their overall functioning. Inspired by the global efficiency, we defined a measure of the communication capabilities among interdependent systems, i.e. the interdependency efficiency. We have quantified the relations between the structural parameters, i.e. the system links and the interdependency links, and the interdependency efficiency. We also have quantified the relations between the structural parameters and the vulnerability towards the propagation of cascading failures. Resorting to this knowledge, we have identified the optimal interdependency connectivity. This choice of system links and interdependency links maximizes the communication among interdependent networks, while at the same time reduces their vulnerability to the propagation of cascading failures.

Similar to the spreading of failures, the formation of a giant component is a critical phenomenon emerging as a result of the connectivity pattern in a network. This structural transition was exploited to identify the formation of macrometastases in the developed model for metastatic colonization in tumor growth. The methods of network theory proved particularly suitable to reproduce the local interactions among tumor cells that lead to the emergent global behavior of the metastasis as a community. This model for intercellular sensing reproduces the stepwise behavior characteristic of metastatic colonization. Moreover, it prompts the consideration of a curative intervention that hinders intercellular communication, even in

the presence of a significant tumor cell population. In view of these results, the study of tumor growth within the framework of complex systems should be fostered and complemented by experimental data from laboratory tests.

Several open problems arise from this dissertation. In Section 3.3, we estimated the parameters of the deterministic model that describes the propagation of cascading failures in isolated networks. The relation between the global connectivity efficiency on one hand and the critical load and the exponential growth rate on the other hand are presented in Figs. 3.8 and 3.6, respectively. These parameters shows two regions with different sensitivities to the global efficiency. We conjecture that this change in the sensitivity identifies a transition in the network when disconnected, isolated nodes are no longer present and every node is reachable from any other node. Investigating the connectivity patterns of networks in the vicinity of the transition point will be beneficial in validating this conjecture. Moreover, the development of a deterministic model independent of the number of nodes would clarify whether the parameter dependence that we have found is shared by all of isolated networks. With respect to this analysis, further insight will be gained by identifying the functional dependence between the deterministic model parameters and the number of system links through the average one-to-one relation between the global efficiency and the number of system links presented in Fig. 3.4.

We foresee that the assessment of the interplay between system structure and propagation of failures in both isolated and interdependent networks, that we presented in this dissertation, can be extended to account for unidirectionality in the connections. The introduction of directed links, i.e. where the overload propagates only along a specific direction, limits the transfer of overload from failed nodes and hinders the propagation of the failure cascade. On the other hand, introducing limitations on links would result in degrading the connectivity efficiency in the network. The introduction of directionality is also an active safety protection measure to prevent the further propagation of the failure cascade in the network. An alternative active protection system can be based on on-line monitoring of the component load and its time derivative to prevent or delay the failure, components that are approaching critical conditions are then disconnected from the network.

The approach presented in this dissertation can also be extended to account for possible

malfunctioning and removal of connections based on their failure probability. The possibility to incorporate links with different features would also open the fundamental modeling, as presented here, to multiple practical applications, such as societal networks or network of acquaintances.

The discussed analysis of isolated and interdependent networks is carried out for systems having fixed numbers of nodes. A different number of nodes may quantitatively influence the outcome of the analysis but should not alter the qualitative behavior of the model. Nonetheless, the results of this dissertation can be expanded to account not only for variations in the number of links but also for variations in the number of nodes. Such an expansion may enable the development of generalized theories or parameters for cascading failures. The only limit to the development of this model is the large computational power required to simulate the propagation of failures in networks having thousands of nodes.

The algorithm that simulate cascading failures contains several parameters that control the outbreak and the propagation of the cascade. The use of probability distribution functions for these parameters allows for the evaluation of the probability connected to different possible faulty scenarios and the estimation of the associated risk. Thus, the analysis can be embedded in a risk assessment framework. Furthermore, the sensitivity of the results with respect to the model parameters can also be assessed.

The model for metastatic colonization during cancer growth can be extended to account for interventions aimed at hindering the development of the metastasis. One of these possible interventions could be the use of receptor blockers to prevent cell-to-cell communication and the ensuing community-scale behavior that triggers the attack to the host organ. In this respect, the receptor blocker can be added as an element in the metastatic networks that can bind to tumor cells. Upon binding, it deactivates the capability of a network element to establish connections with its neighbors.

A criticism that is often presented against the study of the topology of networks and the abstract modeling of cascading failures is that the structure cannot be the only factor affecting the function and the propagation of failures in a network. Therefore, algorithms of failure spreading that account for the propagation of the physical quantities involved in the network failures can be considered. Then, computer/virtual models and experimental data

can be employed to validate the fundamental modeling discussed in this dissertation. The goal would be to validate the assumption that the global system behavior emerges as a result of local interactions among its elements.

Bibliography

[1] Grigg, C., Wong, P., Albrecht, P., Allan, R., Bhavaraju, M., Billinton, R., Chen, Q., Fong, C., Haddad, S., Kuruganty, S., Li, W., Mukerji, R., Patton, D., Rau, N., Reppen, D., Schneider, A., Shahidehpour, M., and Singh, C. (1999) The IEEE reliability test system - 1996. *IEEE Transactions on Power Systems,* **14**(3), 1010–1020.

[2] Zhang, S., Lawson, K. A., Simmons-Menchaca, M., Sun, L., Sanders, B. G., and Kline, K. (2004) Vitamin E analog α-TEA and celecoxib alone and together reduce human MDA-MB-435-FL-GFP breast cancer burden and metastasis in nude mice. *Breast Cancer Res. Treat.,* **87**(2), 111–121.

[3] Euler, L. (1736) Solutio problematis ad geometriam situs pertinentis. *Commentarii academiae scientiarum imperialis Petropolitanae,* **8**, 128–140 Reprinted in Opera Omnia Series Prima, Vol. 7. pp. 1-10, 1766.

[4] Cormen, T. H., Leiserson, C. E., Rivest, R. L., and Stein, C. (2001) Introduction to Algorithms, Second Edition, The MIT Press, Cambridge, Massachussets.

[5] Appel, K. and Haken, W. (1977) Solution of the four color map problem. *Scientific American,* **237**(4), 108–121.

[6] Lawrel, E. L. (1976) Combinatorial Optimization: Networks and Matroids, Holt, Rinehart and Winston, New York, New York.

[7] Milgram, S. (1967) The small world problem. *Psychology Today,* **2**, 60–67.

[8] Watts, D. J. and Strogatz, S. H. (1998) Collective dynamics of 'small-world' networks. *Nature,* **393**, 440–442.

[9] Barabási, A.-L. and Albert, R. (1999) Emergence of scaling in random networks. *Science,* **286**, 509–512.

[10] Boccaletti, S., Latora, V., Moreno, Y., Chavezf, M., and Hwanga, D.-U. (2006) Complex networks: Structure and dynamics. *Physics Reports,* **424**, 175–308.

[11] Albert, R. and Barabási, A.-L. (2000) Topology of evolving networks: Local events and universality. *Physical Review Letters,* **85**(24), 5234–5237.

[12] Albert, R., H., and Barabási, A.-L. (2000) Error and attack tolerance of complex networks. *Nature,* **406**, 378–382.

[13] Pastor-Satorras, R. and Vespignani, A. (2001) Epidemic spreading in scale-free networks. *Physical Review Letters,* **86**(14), 3200–3203.

[14] Stauffer, D. and Aharony, A. (2003) Introduction to percolation theory. 2nd revised edition, Taylor & Francis, London.

[15] Sethna, J. P. (2006) Statistical Mechanics. Entropy, Order Parameters, and Complexity, Oxford University Press Inc., New York, NY.

[16] Strogatz, S. H. (2001) Exploring complex networks. *Nature,* **410**, 268–276.

[17] Watts, D. J. (1999) Networks, dynamics, and the small-world phenomenon. *American Journal of Sociology,* **105**(2), 493–527.

[18] Floyd, R. W. (1962) Algorithm 97: Shortest path. *Comm. Association for Computing Machinery,* **5**(6), 345.

[19] Albert, R. and Barabási, A.-L. (2002) Statistical mechanics of complex networks. *Reviews of Modern Physics,* **74**, 47–97.

[20] Latora, V. and Marchiori, M. (2001) Efficient behavior of small-world networks. *Physical Review Letters,* **87**(19), 198701.

[21] Hines, P. and Blumsack, S. (2008) In *Proceedings of the Proceedings of the 41st Annual Hawaii International Conference on System Sciences* IEEE Computer Society pp. 185–192.

[22] Eusgeld, I., Kröger, W., Sansavini, G., Schläpfer, M., and Zio, E. (2009) The role of network theory and object-oriented modeling within a framework for the vulnerability analysis of critical infrastructures. *Reliability Engineering & Systems Safety,* **94**(5), 954–963.

[23] Zio, E., Sansavini, G., Maja, R., and Marchionni, G. (2008) An analytical approach to the safety of road networks. *International Journal of Reliability, Quality and Safety Engineering,* **15**(1), 67–76.

[24] Latora, V. and Marchoiri, M. (2005) Vulnerability and protection of infrastructure networks. *Physical Review E,* **71**, 015103.

[25] Erdős, P. and Rényi, A. (1960) On the evolution of random graphs. *Publ. Math. Inst. Hung. Acad. Sci.,* **5**, 17–60.

[26] Motter, A. E. and Lai, Y.-C. (2002) Cascade-based attacks on complex networks. *Physical Review E,* **66**(6), 065102.

[27] Motter, A. E. (2004) Cascade control and defense in complex networks. *Phys. Rev. Lett.,* **93**(9), 098701.

[28] Zio, E. and Sansavini, G. (2008) Modelling failure cascade in network systems due to distributed random disturbances. In Martorell, S., (ed.), *Safety, Reliability and Risk Analysis: Theory, Methods and Applications: Proc. Esrel 2008*, Taylor & Francis Group, London pp. 1861–1866.

[29] Dobson, I., Carreras, B. A., and Newman, D. E. (2005) A loading-dependent model of probabilistic cascading failure. *Prob. Eng. Inf. Sci.,* **19**(1), 15–32.

[30] Maiese, K., Wagner, J., and Boccone, L. (1994) Nitric oxide: a downstream mediator of calcium toxicity in the ischemic cascade. *Neuroscience Letters,* **166**(1), 43–47.

[31] Dobson, I., Carreras, B. A., Lynch, V. E., and Newman, D. E. (2007) Complex systems analysis of series of blackouts: Cascading failure, critical points, and self-organization. *Chaos,* **17**(2), 026103.

[32] Cohen, R., Erez, K., benAvraham, D., and Havlin, S. (2000) Resilience of the internet to random breakdowns. *Physical Review Letters,* **85**(21), 4626–4628.

[33] Zheng, J.-F., Gao, Z.-Y., and Zhao, X.-M. (2007) Clustering and congestion effects on cascading failures of scale-free networks. *Europhys. Lett.,* **79**(5), 58002.

[34] Smart, A. G., Amaral, L. A. N., and Ottino, J. M. (2008) Cascading failure and robustness in metabolic networks. *Proc. Nat. Acad. Sci. U.S.A.,* **105**(36), 13223–13228.

[35] Glass, R. J. J., Stamber, K. L., and Beyeler, W. E. Advanced simulation for analysis of critical infrastructure : abstract cascades, the electric power grid, and fedwire. Technical Report SAND2004-4239 Sandia National Laboratories Report (2004).

[36] Chen, Q. and McCalley, J. D. (2005) Identifying high risk N-k contingencies for online security assessment. *IEEE Transactions on Power Systems,* **20**(2).

[37] Kodsi, S. K. M. and Canizares, C. A. (2007) Application of a stability-constrained optimal power flow to tuning of oscillation controls in competitive electricity markets. *IEEE Transactions on Power Systems,* **22**(4), 1944.

[38] Billington, R. and Allan, R. (1984) Reliability evaluation of power systems, Plenum Publishing Corp., New York, NY, United States.

[39] Chassin, D. P. and Posse, C. (2005) Evaluating north american electric grid reliability using the barabsi-albert network model. *Physica A,* **355**(2-4), 667–677.

[40] Crucitti, P., Latora, V., and Marchiori, M. (2004) Model for cascading failures in complex networks. *Phys. Rev. E,* **69**(4), 045104.

[41] Carreras, B. A., Newman, D. E., Gradney, P., Lynch, V. E., and Dobson, I. (2007) Interdependent risk in interacting infrastructure systems. IEEE Computer Society, Washington, DC, USA p. 112.

[42] Kim, D.-H., Kim, B. J., and Jeong, H. (2005) Universality class of fiber bundle model on complex networks. *Physical Review Letters,* **94**, 025501.

[43] Barabasi, A. L., Albert, R., and Jeong, H. (1999) Mean-field theory for scale-free random networks. *Physica A,* **272**, 173–187.

[44] Huang, K. (1987) Statistical mechanics, John Wiley & Sons, New York, NY 2nd, edition.

[45] Rinaldi, S. M. (2004) In *Proceedings of the 37th Annual Hawaii International Conference on System Sciences (HICSS'04) - Track 2 - Volume 2* p. 20054.1.

[46] Little, R. G. (2002) Controlling cascading failure: Understanding the vulnerabilities of interconnected infrastructures. *Journal of Urban Technology,* **9**(1), 109–123.

[47] Zimmerman, R. (2001) Social implications of infrastructure network interactions. *Journal of Urban Technology,* **8**(3), 97–119.

[48] Zio, E. and Sansavini, G. (2011) Modeling interdependent network systems for identifying cascade-safe operating margins. *IEEE Transactions on Reliability* (to appear), **60**(2).

[49] EU project IRRIIS, Deliverable D222, Tools and techniques for interdependency analysis. `http://www.irriis.org/File.aspx?lang=2\&oiid=9138\&pid=572` (2007).

[50] Min, H.-S. J., Beyeler, W., Brown, T., Son, Y. J., and Jones, A. T. (2007) Toward modeling and simulation of critical national infrastructure interdependencies. *IIE Transactions,* **39**(1), 57–71.

[51] Apostolakis, E. G. and Lemon, M. D. (2005) A screening methodology for the identification and ranking of infrastructure vulnerabilities due to terrorism. *Risk Analysis,* **25**(2).

[52] Dekker, A. H. (2005) Simulating network robustness for critical infrastructure networks. In Estivill-Castro, V., (ed.), *Conferences in Research and Practice in Information Technology, Proceedings of the 28th Australasian Computer Science Conference, The University of Newcastle, Newcastle, Australia*, Vol. 38, pp. 1–5.

[53] Lee, E. E., Mitchell, J. E., and Wallace, W. A. (2007) Restoration of services in interdependent infrastructure systems: a network flows approach. *IEEE Transactions on Systems, Man, and Cybernetics-Part C (Applications and Reviews),* **37**(6), 1303–1317.

[54] Adachi, T. and Ellingwood, B. R. (2008) Serviceability of earthquake-damaged water systems: effects of electrical power availability and power backup systems on system vulnerability. *Reliability Engineering and System Safety,* **93**(1), 78–88.

[55] Piwowar, J., Chatelet, E., and Laclemence, P. (2009) An efficient process to reduce infrastructure vulnerabilities facing malevolence. *Reliability Engineering and System Safety,* **94**, 1869–1877.

[56] Helseth, A. and Holen, A. T. (2009) Structural vulnerability of energy distribution systems: incorporating infrastructural dependencies. *Electrical Power and Energy Systems,* **31**, 531–537.

[57] Newman, D. E., Nkei, B., Carreras, B. A., Dobson, I., Lynch, V. E., and Gradney, P. (2005) In *Proc. Thirty-Eight Annu. Hawaii International Conf. on System Sciences, January 3-6, 2005* IEEE Computer Society, Washington, DC, USA p. 63.3.

[58] Duenas-Osorio, L., Craig, J. I., and Goodno, B. J. (2007) Seismic response of critical interdependent networks. *Earthquake Engineering and Structural Dynamics,* **36**(2), 285–306.

[59] Svendsen, N. K. and Wolthusen, S. D. (2007) Connectivity models of interdependency in mixed-type critical infrastructure networks. *Information Security Technical Report,* **12**(1), 44–55.

[60] Dueas-Osorio, L. and Vemuru, S. M. (2009) Cascading failures in complex infrastructure systems. *Structural Safety,* **31**, 157–167.

[61] Johansson, J. and Jonsson, H. (2008) A model for vulnerability analysis of interdependent infrastructure networks. In Martorell, S., (ed.), *Safety, Reliability and Risk Analysis: Theory, Methods and Applications: Proc. Esrel 2008*, Taylor & Francis Group, London pp. 2491–2499.

[62] Ouyang, M., Hong, L., Mao, Z.-J., Yu, M.-H., and Qi, F. (2009) A methodological approach to analyze vulnerability of interdependent infrastructures. *Simulation Modeling Practice and Theory,* **17**(5), 817–828.

[63] Barton, D. C. and Stamber, K. L. (2000) In *Proc. International Energy Foundation's Conference ENERGEX 2000 - 8th International Energy Forum, Las Vegas, NV, USA.*

[64] Panzieri, S., Setola, R., and Ulivi, G. (2004) In *Securing Critical Infrastructures, CRIS2004 : Conference on Critical Infrastructures, October 25 - 27, 2004, Grenoble, France.*

[65] Casalicchio, E., Galli, E., and Tucci, S. (2007) In *11th IEEE Symposium on Distributed Simulation and Real-Time Applications* IEEE Computer Society Washington, DC, USA pp. 182–189.

[66] Schläpfer, M., Kessler, T., and Kröger, W. (2008) In *Proc. 16th Power Systems Computation Conf., 14-18 July, Glasgow, UK.*

[67] Chen, Q. and McCalley, J. D. (2005) Identifying high risk N-k contingencies for online security assessment. *IEEE Transactions on Power Systems,* **20**(2).

[68] Kodsi, S. K. M. and Canizares, C. A. (2007) Application of a stability-constrained optimal power flow to tuning of oscillation controls in competitive electricity markets. *IEEE Transactions on Power Systems,* **22**(4), 1944.

[69] Hong, X., Gerla, M., Pei, G., and Chiang, C.-C. (1999) In *Proceedings of the 2nd ACM international workshop on Modeling, analysis and simulation of wireless and mobile systems, Seattle, Washington, United States* pp. 53–60.

[70] Germann, T. C., Kadau, K., Longini Jr., I. M., and Macken, C. A. (2006) Mitigation strategies for pandemic influenza in the united states. *Proc. Natl. Acad. Sci. USA,* **103**(15), 5935–5940.

[71] Casalicchio, E., Galli, E., and Ottaviani, V. (2009) In *Proceedings of the 2009 13th IEEE/ACM International Symposium on Distributed Simulation and Real Time Applications* pp. 255–258.

[72] Haimes, Y. Y. and Jiang, P. (2001) Leontief-based model of risk in complex interconnected infrastructures. *Journal of Infrastructure Systems,* **7**(1), 1–12.

[73] Jiang, P. and Haimes, Y. Y. (2004) Risk management for Leontief-based interdependency systems. *Risk Analysis,* **24**(5), 1215–1229.

[74] Haimes, Y. Y., Horowitz, B. M., Lambert, J. H., Santos, J. R., Lian, C., and Crowther, K. G. (2005) Inoperability Input-Output model for interdependent infrastructure sectors. I: theory and methodology. *Journal of Infrastructures Systems,* **11**(2), 67–79.

[75] Haimes, Y. Y., Horowitz, B. M., Lambert, J. H., Santos, J. R., Lian, C., and Crowther, K. G. (2005) Inoperability Input-Output model for interdependent infrastructure sectors. I: case studies. *Journal of Infrastructures Systems,* **11**(2), 80–92.

[76] Reed, D. A., Kapur, K. C., and Christie, R. D. (2009) Methodology for assessing the resilience of networked infrastructure. *IEEE Systems Journal,* **3**(2), 174–180.

[77] Cagno, E., De Ambroggi, M., Grande, O., and Trucco, P. (2009) In *Reliability, Risk and Safety: Theory and Applications - Proc. ESREL 2009 Europe Annual Conf., 6-11 September 2009, Prague, Czech Republic* Taylor & Francis Group, London pp. 1899–1906.

[78] Buldyrev, S. V., Parshani, R., Paul, G., Stanley, H. E., and Havlin, S. (2010) Catastrophic cascade of failures in interdependent networks. *Nature,* **464**, 1025–1028.

[79] Gautam, D., Singh, R. R., and Singh, V. K. (2009) In *Proc. International Conference on Intelligent Agent & Multi-Agent Systems, IAMA 2009* pp. 1–5.

[80] Dorogovtsev, S. N., Goltsev, A. V., and Mendes, J. F. F. (2008) Critical phenomena in complex networks. *Reviews of Modern Physics,* **6**, 119–143.

[81] Dorogovtsev, S. N. and Mendes, J. F. F. (2003) Evolution of networks: from biological nets to the Internet and WWW, Oxford University Press, Oxford.

[82] Kim, J., Krapivsky, P. L., Kahng, B., and Redner, S. (2002) Infinite-order percolation and giant fluctuations in a protein interaction network. *Phys. Rev. E,* **66**(5), 055101(R).

[83] Cho, Y. S., Kim, J. S., Park, J., Kahng, B., and Kim, D. (2009) Percolation transitions in scale-free networks under the achlioptas process. *Physical Review Letters,* **103**, 135702.

[84] Radicchi, F. and Fortunato, S. (2009) Explosive percolation in scale-free networks. *Physical Review Letters,* **103**, 168701.

[85] Jemal, A., Siegel, R., Ward, E., Hao, Y., Xu, J., , and Thun, M. J. (2009) Cancer statistics, 2009. *CA Cancer J. Clin.,* **59**, 225–249.

[86] Chambers, A. F., Groom, A. C., and MacDonald, I. C. (2002) Dissemination and growth of cancer cells in metastatic sites. *Nature Rev. Cancer,* **2**, 563–572.

[87] Hiratsuka, S., Watanabe, A., Aburatani, H., and Maru, Y. (2006) Tumor-mediated upregulation of chemoattractants and recruitment of myeloid cells predetermines lung metastasis. *Nature Cell Biol.,* **8**(12), 1369–1375.

[88] Steeg, P. S. (2006) Tumor metastasis: mechanistic insights and clinical challenges. *Nature Medicine,* **12**(8), 895–904.

[89] Psaila, B. and Lyden, D. (2009) The metastatic niche: adapting the foreign soil. *Nature Rev. Cancer,* **9**, 285–293.

[90] Kaplan, R. N., Riba, R. D., Zacharoulis, S., Bramley, A. H., Vincent, L., Costa, C., MacDonald, D. D., Jin, D. K., Shido, K., Kerns, S. A., Zhu, Z., Hicklin, D., Wu, Y., Port, J. L., Altorki, N., Port, E. R., Ruggero, D., Shmelkov, S. V., Jensen, K. K., Rafii, S., and Lyden, D. (2005) VEGFR1-positive haematopoietic bone marrow progenitors initiate the pre-metastatic niche. *Nature,* **438**, 820–828.

[91] Hiratsuka, S., Watanabe, A., Sakurai, Y., Akashi-Takamura, S., Ishibashi, S., Miyake, K., Shibuya, M., Akira, S., Aburatani, H., and Maru, Y. (2008) The S100A8-serum amyloid A3TLR4 paracrine cascade establishes a pre-metastatic phase. *Nature Cell Biol.,* **10**, 1349–1355.

[92] Hickson, J., Yamada, S. D., Berger, J., Alverdy, J., O'Keefe, J., Bassler, B., and Rinker-Schaeffer, C. (2009) Societal interactions in ovarian cancer metastasis: a quorum-sensing hypothesis. *Clin. Exp. Metastasis,* **26**, 67–76.

[93] Bassler, B. L. (2002) Small talk. Cell-to-cell communication in bacteria. *Cell,* **109**, 421–424.

[94] Jefferson, K. K. (2004) What drives bacteria to produce a biofilm?. *FEMS Microbiol. Lett.,* **236**, 163–173.

[95] Stanley, N. R. and Lazazzera, B. A. (2004) Environmental signals and regulatory pathways that influence biofilm formation. *Microbiol.,* **52**, 917–924.

[96] Waters, C. M. and Bassler, B. L. (2005) Quorum sensing: cell-to-cell communication in bacteria. *Annu. Rev. Cell Dev. Biol.,* **21**, 319–346.

[97] Elias, L. A. B., Wang, D. D., and Kriegstein, A. R. (2007) Gap junction adhesion is necessary for radial migration in the neocortex. *Nature,* **448**, 901–907.

[98] Swanson, K. R., Bridge, C., Murray, J. D., and Alvord Jr., E. C. (2003) Virtual and real brain tumors: using mathematical modeling to quantify glioma growth and invasion. *J. Neurol. Sci.,* **216**, 1–10.

[99] Ganguly, R. and Puri, I. K. (2006) Mathematical model for the cancer stem cell hypothesis. *Cell Prolif.,* **39**, 3–14.

[100] Frieboes, H. B., Lowengrub, J. S., Wise, S., Zheng, X., Macklin, P., Bearer, E., and Cristini, V. (2007) Computer simulation of glioma growth and morphology. *Neuroimage,* **37**(Suppl. 1), S59–S70.

[101] Macklin, P. and Lowengrub, J. (2007) Nonlinear simulation of the effect of microenvironment on tumor growth. *J. Theor. Biol.,* **245**, 677–704.

[102] Stein, A. M., Demuth, T., Mobley, D., Berens, M., and Sander, L. M. (2007) A mathematical model of glioblastoma tumor spheroid invasion in a three-dimensional in vitro experiment. *Biophys. J.,* **92**(1), 356–365.